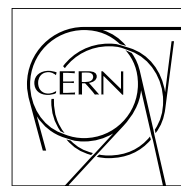


# The Compact Muon Solenoid Experiment Analysis Note

The content of this note is intended for CMS internal use and distribution only



23 May 2017 (v7, 04 July 2019)

## Measurement of the top-anti-top differential production cross section of high transverse momentum top quarks in the all-hadronic final state using the 2016 proton-proton collision data at $\sqrt{s} = 13$ TeV.

Yorgos Tsipolitis  
*National Technical University of Athens*

Konstantinos Kousouris  
*National Technical University of Athens*

Georgios Bakas  
*National Technical University of Athens*

Garyfallia Paspalaki  
*National Center of Scientific Research "Demokritos"*

Andrea Castro  
*Universita e INFN, Bologna*

Federico Celli  
*Universita e INFN, Bologna*

Pralay Kumar Mal  
*National Institute of Science Education and Research*

### Abstract

A measurement of the production cross section of high transverse momentum ( $p_T$ ) top quark pairs is reported. The dataset was collected during 2016 with the CMS detector at the CERN LHC from proton-proton collisions at a center-of-mass energy of 13 TeV, and corresponds to an integrated luminosity of  $35.9 \text{ fb}^{-1}$ . The measurement uses events where either both top quark candidates decay hadronically and are reconstructed as large- $R$  jets with  $p_T > 400 \text{ GeV}$ . The cross section is extracted differentially as a function of kinematic variables of the top quark or top quark pair system. The results are unfolded to the particle and parton levels, and are compared to various theoretical models. The measured cross section is significantly lower, by up to 40%, in the phase space of interest, compared

to the theory predictions, while the normalized differential cross sections are consistent between data and theory.

This box is only visible in draft mode. Please make sure the values below make sense.

PDFAuthor: Konstantinos Kousouris, Georgios Tsipolitis, Georgios Bakas, Prolay Kumar Mal, Andrea Castro, Federico Celli

PDFTitle: Measurement of the top-anti-top quark differential production cross section in the all-hadronic final state using the 2016 proton-proton collision data at  $\text{sqrt}(s) = 13 \text{ TeV}$ .

PDFSubject: CMS

PDFKeywords: CMS, physics, top, qcd, jets

Please also verify that the abstract does not use any user defined symbols

DRAFT

## 1 Contents

2	1	Introduction . . . . .	2
3	2	Samples . . . . .	2
4	2.1	Data . . . . .	2
5	2.2	Simulation . . . . .	3
6	3	Trigger . . . . .	5
7	4	Reconstruction and Selection . . . . .	7
8	4.1	Object Reconstruction . . . . .	7
9	4.2	Selection . . . . .	7
10	4.3	Multivariate Discriminant . . . . .	10
11	4.4	Parton level . . . . .	13
12	4.5	Particle level . . . . .	13
13	5	Data vs Monte Carlo . . . . .	13
14	6	Background . . . . .	17
15	7	Signal Extraction . . . . .	20
16	8	Systematic Uncertainties . . . . .	23
17	9	Fiducial Measurement . . . . .	31
18	10	Unfolded Measurement . . . . .	34
19	10.1	Parton Level . . . . .	34
20	10.2	Particle Level . . . . .	40
21	11	Summary . . . . .	46
22	A	NN Input Variables . . . . .	51
23	B	Control Distributions . . . . .	55
24	C	Background Sensitivity to Pileup . . . . .	60
25	D	Unfolding Tests . . . . .	61

---

## 26 1 Introduction

27 The top quark completes the third generation of quarks in the standard model (SM), and the  
 28 precise knowledge of its properties is critical for the overall understanding of the theory. Mea-  
 29 surements of the top-anti-top quark pair ( $t\bar{t}$ ) production cross section confront the predictions  
 30 from quantum chromodynamics (QCD) and have the potential to constrain the QCD param-  
 31 eters, while being sensitive to physics beyond the SM. Also, the  $t\bar{t}$  production process is a  
 32 dominant SM background to searches for new physics phenomena and therefore its precise  
 33 knowledge is essential for new discoveries.

34 The large  $t\bar{t}$  yield expected in proton-proton (pp) collisions at the CERN LHC allows to perform  
 35 measurements of the  $t\bar{t}$  production rate in a large phase space, and, more importantly, differ-  
 36 entially, as a function of the  $t\bar{t}$  kinematic properties. Such measurements have been performed  
 37 by the ATLAS [1–6] and CMS [7–15] Collaborations at 7, 8, and 13 TeV center-of-mass energies,  
 38 under the hypothesis of the resolved final state, where the decay products of the  $t\bar{t}$  pair can  
 39 be reconstructed individually. This hypothesis is valid for top quark transverse momenta,  $p_T$ ,  
 40 up to approximately 500 GeV. However, at higher  $p_T$  ( $p_T/m \approx 1$ ), the top quark decay prod-  
 41 ucts are highly collimated ("boosted") and they can no longer be reconstructed separately. In  
 42 order to explore the highly boosted phase space, hadronic top quark decays are reconstructed  
 43 as large-radius jets. Previous efforts in this domain by the ATLAS [16, 17] and CMS [18–20]  
 44 Collaborations confirm that it is feasible to perform precise differential measurements of the  $t\bar{t}$   
 45 production and have also shown interesting deviations from the theory predictions.

46 In this note, a measurement of the differential boosted  $t\bar{t}$  production cross section in the hadronic  
 47 final state is presented, using pp collisions at  $\sqrt{s} = 13$  TeV recorded with the CMS detector  
 48 during the 2016 LHC run and amounting to a total integrated luminosity of  $35.9\text{ fb}^{-1}$ . In the  
 49 hadronic decay channel, each W boson arising from the top quark decays into a pair of light  
 50 quarks. As a result, the final state consists of at least six partons (more are possible due to  
 51 initial- and final-state radiation), two of which are b quarks. Due to the high boost consid-  
 52 ered in this measurement ( $p_T > 400$  GeV), the top quarks are reconstructed unambiguously as  
 53 large-radius jets and the final state consists of at least two such jets.

54 This note is organized as follows: section 2 describes the data and Monte Carlo samples used  
 55 in the analysis and section 3 discusses the triggers and the measurement of the corresponding  
 56 efficiency. Then, section 4 presents the details of the jet reconstruction and the event selection.  
 57 A comparison between data and simulation is reported in section 5. The background estimation  
 58 technique is presented in section 6. The signal extraction and the systematic uncertainties are  
 59 discussed in sections 7 and 8, respectively, while the results are presented in sections 9 and 10.  
 60 Finally, section 11 summarizes the results.

## 61 2 Samples

62 In this section we describe the data and Monte Carlo samples that are used in the analysis.

### 63 2.1 Data

64 The collision events used for the measurement of the  $t\bar{t}$  cross section have been collected with  
 65 the triggers described in Section 3 that are part of the JetHT primary dataset. Table 1 lists  
 66 the samples that correspond to different data-taking eras and have been reconstructed in the  
 67 03Feb2017 reprososing. The good Run and luminosity section list used is contained in the  
 68 certification file Cert\_271036-284044\_13TeV\_23Sep2016ReReco\_Collisions16\_JSON.txt.

- 69 The total integrated luminosity of the analyzed data is  $35.9 \text{ fb}^{-1}$ .
- 70 In addition to the data from the JetHT dataset, we have used the SingleMuon dataset for the  
71 measurement of the trigger efficiency. The eras and run ranges are the same as the ones in  
72 Table 1.

Table 1: Data samples.

Sample	Run range	Luminosity ( $\text{pb}^{-1}$ )
/JetHT/Run2016B-03Feb2017_ver2-v2/MINIAOD	273150-275376	5750
/JetHT/Run2016C-03Feb2017-v1/MINIAOD	275656-276283	2573
/JetHT/Run2016D-03Feb2017-v1/MINIAOD	276315-276811	4242
/JetHT/Run2016E-03Feb2017-v1/MINIAOD	276947-277420	4025
/JetHT/Run2016F-03Feb2017-v1/MINIAOD	277932-278808	3105
/JetHT/Run2016G-03Feb2017-v1/MINIAOD	278820-280385	7576
/JetHT/Run2016H-03Feb2017_ver2-v1/MINIAOD	281613-284035	8435
/JetHT/Run2016H-03Feb2017_ver3-v1/MINIAOD	284036-284044	216

## 73 2.2 Simulation

- 74 Monte Carlo simulation is used to generate samples for the  $t\bar{t}$  signal and to model the kine-  
75 matic distributions of some of the background processes. Samples of simulated  $t\bar{t}$  events have  
76 been generated at next-to-leading order (NLO) in QCD using POWHEG v2 [21–25], assuming  
77 a top quark mass of  $m_t = 172.5 \text{ GeV}$ . Single top quark production in the  $t$  channel or in as-  
78 sociation with a W boson are simulated at NLO with POWHEG [26]. The production of W or  
79 Z bosons in association with jets (+jets), as well as QCD multijet events, are simulated with  
80 MG5\_AMC@NLO [27] at leading order (LO), with the MLM matching algorithm [28].
- 81 All simulated events are processed with PYTHIA 8.212 [29, 30] for modeling of the parton show-  
82 ering, hadronization, and underlying event (UE). The NNPDF 3.0 [31] Parton Distribution  
83 Functions (PDF) are used throughout, and the CUETP8M1 UE tune [32] is used for all processes  
84 except for the  $t\bar{t}$ ,  $t\bar{t}H$  and single top quark processes, for which the tune CUETP8M2T4 [33] is  
85 used. The Simulation of the CMS detector response is based on GEANT4 [34]. Additional pp  
86 interactions in the same or neighbouring bunch crossings (pileup) are simulated with PYTHIA  
87 and overlaid with generated events according to the pileup distribution measured in data.
- 88 The various simulated processes are normalized to the best known theoretical cross sections,  
89 namely the  $t\bar{t}$ , +jets, and single top quark samples are normalized to NNLO precision in QCD [35–  
90 37].
- 91 The measured cross sections for the  $t\bar{t}$  process are compared to theoretical predictions provided  
92 by the following Monte Carlo models: POWHEG combined with PYTHIA for the parton show-  
93 ering, as described above, or combined with HERWIG ++ [38] and the corresponding EE5C UE  
94 tune [39]. In addition,  $t\bar{t}$  events were also generated with MC@NLO [27] combined with PYTHIA  
95 for the parton showering.
- 96 In the first part of Table 2 we show the signal samples, while in the second part we show the  
97 background ones that include QCD multijet production, associated production of vector bosons  
98 ( $W^\pm, Z$ ) with jets, and single-top production. The list shows the total number of events ana-  
99 lyzed, including all samples of the same kind (nominal, extensions, backup). The reconstruc-  
100 tion of the Monte Carlo samples belongs to the era RunIISummer16MiniAODv2-PUMoriond17\_80X\_mcRun2\_asy-  
101 and we have used the MINIAODSIM data tier. The reported cross sections have been used in  
102 the normalization of the various processes in the data vs MC comparison plots.

Table 2: Monte Carlo samples.

Sample	Events ( $\times 10^6$ )	$\sigma$ (pb)
TT_TuneCUETP8M2T4_13TeV-powheg-pythia8, backup	153.4	832
TTJets_TuneCUETP8M2T4_13TeV-amcatnloFXFX-pythia8, backup	87.9	832
TT_TuneEE5C_13TeV-powheg-herwigpp, ext2, ext3	57.7	832
TT_hdampDOWN_TuneCUETP8M2T4_13TeV-powheg-pythia8, ext1	57.9	832
TT_hdampUP_TuneCUETP8M2T4_13TeV-powheg-pythia8, ext1	58.2	832
TT_TuneCUETP8M2T4down_13TeV-powheg-pythia8, ext1	58.3	832
TT_TuneCUETP8M2T4up_13TeV-powheg-pythia8, ext1	58.9	832
TT_TuneCUETP8M2T4_13TeV-powheg-fsrdown-pythia8, ext1, ext2	155.7	832
TT_TuneCUETP8M2T4_13TeV-powheg-fsrup-pythia8, ext1, ext2	152.6	832
TT_TuneCUETP8M2T4_13TeV-powheg-isrdown-pythia8, ext1, ext2	148.5	832
TT_TuneCUETP8M2T4_13TeV-powheg-isrup-pythia8_ext1, ext2	156.5	832
TT_TuneCUETP8M2T4_mtop1665_13TeV-powheg-pythia8, ext1, ext2, backup	19.4	832
TT_TuneCUETP8M2T4_mtop1715_13TeV-powheg-pythia8	19.6	832
TT_TuneCUETP8M2T4_mtop1735_13TeV-powheg-pythia8	19.4	832
TT_TuneCUETP8M2T4_mtop1755_13TeV-powheg-pythia8, ext1, ext2	59.4	832
TT_TuneCUETP8M2T4_mtop1785_13TeV-powheg-pythia8	16.4	832
QCD_HT200to300_TuneCUETP8M1_13TeV-madgraphMLM-pythia8, ext1	57.6	1.712e+6
QCD_HT300to500_TuneCUETP8M1_13TeV-madgraphMLM-pythia8, ext1	54.5	3.477e+5
QCD_HT500to700_TuneCUETP8M1_13TeV-madgraphMLM-pythia8, ext1	62.3	3.21e+4
QCD_HT700to1000_TuneCUETP8M1_13TeV-madgraphMLM-pythia8, ext1	45.4	6831
QCD_HT1000to1500_TuneCUETP8M1_13TeV-madgraphMLM-pythia8, ext1	15.1	1207
QCD_HT1500to2000_TuneCUETP8M1_13TeV-madgraphMLM-pythia8, ext1	11.8	119.9
QCD_HT2000toInf_TuneCUETP8M1_13TeV-madgraphMLM-pythia8, ext1	6.0	25.24
DYJetsToQQ_HT180_13TeV-madgraphMLM-pythia8	12.1	1187
WJetsToQQ_HT180_13TeV-madgraphMLM-pythia8	22.4	2788
ST_t-channel_top_4f_inclusiveDecays_13TeV-powhegV2-madspin-pythia8_TuneCUETP8M1	67.2	136.02
ST_t-channel_antitop_4f_inclusiveDecays_13TeV-powhegV2-madspin-pythia8_TuneCUETP8M1	38.8	80.95
ST_tW_top_5f_inclusiveDecays_13TeV-powheg-pythia8_TuneCUETP8M1_ext1	6.9	35.6
ST_tW_antitop_5f_inclusiveDecays_13TeV-powheg-pythia8_TuneCUETP8M1_ext1	6.9	35.6

### 103 3 Trigger

104 The trigger path employed for the collection of signal events uses single-jet L1 seeds that re-  
 105 quire the presence of a jet with  $p_T > 180 \text{ GeV}$ . At HLT jets are reconstructed from (online)  
 106 particle flow candidates using the anti-kt algorithm with distance parameter  $R = 0.8$  and their  
 107 mass, after trimming of soft particles, must be greater than  $30 \text{ GeV}$ . Interesting events are re-  
 108 quired to have at least two such jets with  $p_T > 280(200) \text{ GeV}$  for the leading (trailing) one.  
 109 Finally, at least one of the two jets should be tagged as a b-jet, using the online CSV algorithm.  
 110 The aforementioned trigger path ran unprescaled for the duration of the 2016 run, collecting an  
 111 integrated luminosity of  $35.9 \text{ fb}^{-1}$ . A second, prescaled, path, using the same L1 seed, was also  
 112 employed, with identical kinematic requirements but no b-tagging cut, which ran in parallel  
 113 and collected and integrated luminosity of  $1.67 \text{ fb}^{-1}$ . This path is used for the selection of a  
 114 control QCD sample, as described later. All the triggers described above are summarized in  
 115 Table 3. Finally, it should be noted that the pileup profile of the prescaled control trigger is  
 116 shifted to lower number of interactions (Fig. 1), because the path tended to collect more data  
 117 towards the end of the fills when the instantaneous luminosity was lower.

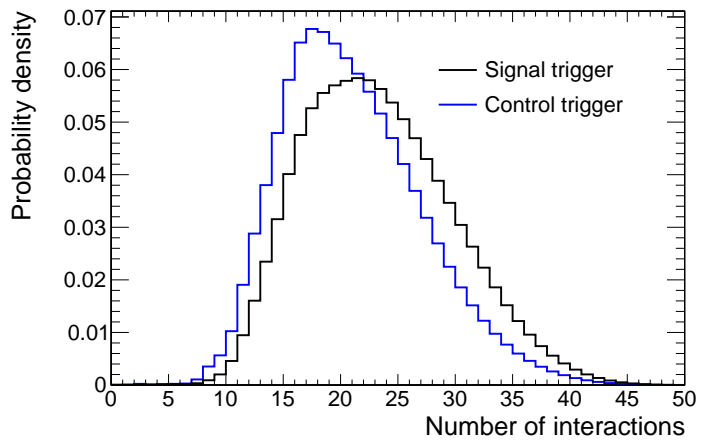


Figure 1: Pileup profile for the signal and control trigger paths.

Table 3: Summary of triggers used in the analysis.

Trigger	Purpose
L1_SingleJet180 OR L1_SingleJet200	L1 seed
HLT_AK8DiPFJet280_200_TrimMass30_BTagCSV_p20	signal HLT path
HLT_AK8DiPFJet280_200_TrimMass30	control HLT path

118 The efficiency of the signal trigger path is measured with respect to an orthogonal path that  
 119 requires the presence of an isolated muon with  $p_T > 27 \text{ GeV}$  (HLT\_IsoMu27). Figure 2 shows  
 120 the trigger efficiency as a function of the second jet  $p_T$  in events with at least two reconstructed  
 121 jets, with at least one of them containing a b-tagged subjet. For details about the offline recon-  
 122 struction see Section 4. The efficiency measured in data is compared to the simulated efficiency,  
 123 showing an excellent agreement. The offline selection requires that the second jet  $p_T$  is greater  
 124 than  $400 \text{ GeV}$ , which is at the beginning of the efficiency plateau.

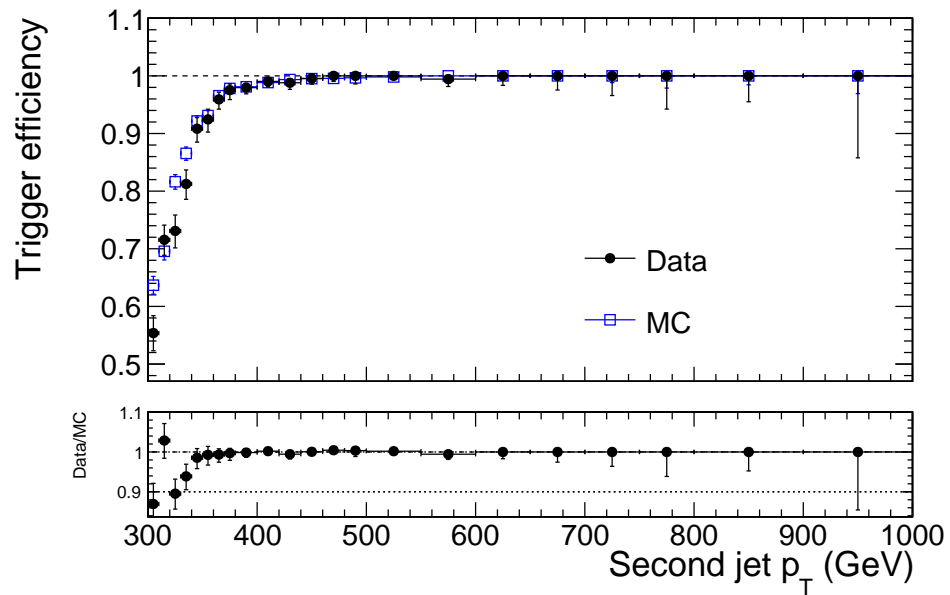


Figure 2: Trigger efficiency for the signal path of the analysis.

## 125 4 Reconstruction and Selection

126 In this section we present the objects used in the analysis, the multivariate method that dis-  
 127 criminated  $t\bar{t}$  events from the QCD multijet background, and we describe the event selection.

### 128 4.1 Object Reconstruction

129 The leptons (muons, electrons) used in the analysis come from the default reconstructed col-  
 130 lections in CMS samples ('slimmedMuons' and 'slimmedElectrons') and must have  
 131  $p_T > 20 \text{ GeV}$ . Muons are required to pass the medium ID working point and electrons should  
 132 pass the tight working point, while both lepton types should have a relative mini-isolation less  
 133 than 0.1.

134 Jets are reconstructed from particle-flow (PF) candidates that have undergone charged-hadron  
 135 subtraction (CHS) in order to suppress the contribution from multiple soft interactions in the  
 136 same bunch crossing (pileup). The momentum 4-vectors of the PF candidates are clustered  
 137 with the anti-kt algorithm with distance parameter  $R = 0.8$ , hence we refer to AK8 PFCHS  
 138 jets. These jets are required to pass the tight jet ID. Furthermore, an algorithm is run to identify  
 139 subjets with distance parameter  $R = 0.4$  within the AK8 jets. Finally, the soft-drop technique  
 140 is used in order to evaluate the mass of the AK8 jet with suppressed pileup contribution. For  
 141 all the aforementioned algorithms we have used the default definitions in the CMS software  
 142 and the default collections in the MINIAOD data and Monte Carlo samples. For the energy  
 143 calibration of the AK8 jets we have used the recommended corrections by the JME POG in the  
 144 80X\_dataRun2\_2016SeptRepro\_v7 and 80X\_mcRun2\_asymptotic\_2016\_TrancheIV\_v8 global  
 145 tags.

146 The selection of AK8 jets that originate from the top decay relies on the identification of a b-jet  
 147 within them. For this purpose, we use the CSVv2 b-tagging algorithm applied on the AK4  
 148 subjets of each AK8 jet. In particular, we use the medium working point, which requires the  
 149 value of the tagger to be greater than 0.8484.

150 Since leptons are also reconstructed as jets, we perform cross cleaning by removing each iden-  
 151 tified lepton from the jet collection with geometrical matching in the  $\eta - \phi$  space: if a jet has  
 152  $\Delta R = \sqrt{(\Delta\eta)^2 + (\Delta\phi)^2} < 0.4$  from any accepted lepton candidate it is removed from the jet  
 153 collection.

### 154 4.2 Selection

155 The baseline selection, summarized in Table 4 is common for all regions used in the analysis  
 156 and it requires at least two jets in the event with  $p_T > 400 \text{ GeV}$  and softDrop masses in the  
 157 range  $(50, 300) \text{ GeV}$ . Also, a lepton veto is applied in order to minimize the probability to select  
 158 leptonic top decays. Then, on top of the baseline selection, we define four specific regions  
 159 (Table 4) based on the NN output (Section 4.3), the jets' softDrop masses, and the number of  
 160 b-tagged subjets in each jet, that serve different analysis purposes. The signal region ( $SR$ ) is  
 161 where we perform the differential measurements and it requires both jets to have a b-tagged  
 162 subjet, a tighter selection on the jets' masses, and a high mva value. Figure 3 shows the top  
 163 decay mode of the selected  $t\bar{t}$  events, where more than 95% come from the hadronic channel.  
 164 The QCD control region ( $CR$ ) is the same as the SR but with the b-tagging requirement reverted  
 165 (the jets should not contain a b-tagged subjet) and it is used to get from data the shape of the  
 166 QCD background for each variable of interest. Then, we employ the signal region A ( $SR_A$ ),  
 167 which is used to determine the normalization of the QCD background, and finally the signal  
 168 region B ( $SR_B$ ), which is used to constrain some of the signal modelling uncertainties. Figure 4

<sup>169</sup> shows a cartoon of the signal regions on the plane defined by the NN output and the jet masses.

Table 4: Baseline selection requirements.

Observable	Requirement
$N_{\text{jets}}$	$> 1$
$N_{\text{leptons}}$	$= 0$
$p_{\text{T}}^{\text{jet}1,2}$	$> 400 \text{ GeV}$
$m_{SD}^{\text{jet}1,2}$	$(50, 300) \text{ GeV}$

Table 5: Selection requirements per analysis region.

Region	Trigger	Offline Requirements	Purpose
$SR$	signal	$\text{Base+NN} > 0.8 + 2\text{btags} + m_{SD}^{\text{jet}1,2} \in (120, 220) \text{ GeV}$	signal region
$SR_A$	signal	$\text{Base+NN} > 0.8 + 2\text{btags}$	QCD fit region
$SR_B$	signal	$\text{Base} + 2\text{btags} + m_{SD}^{\text{jet}1,2} \in (120, 220) \text{ GeV}$	signal systematics region
$CR$	control	$\text{Base+NN} > 0.8 + 0\text{btags} + m_{SD}^{\text{jet}1,2} \in (120, 220) \text{ GeV}$	QCD control region

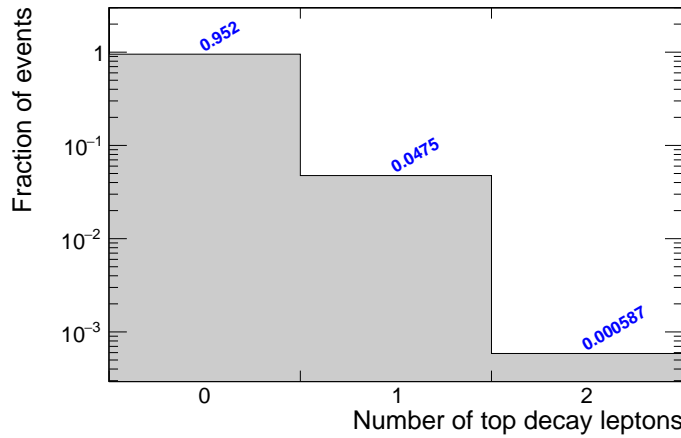


Figure 3: Distribution of  $t\bar{t}$  decay modes after the signal selection of the analysis.

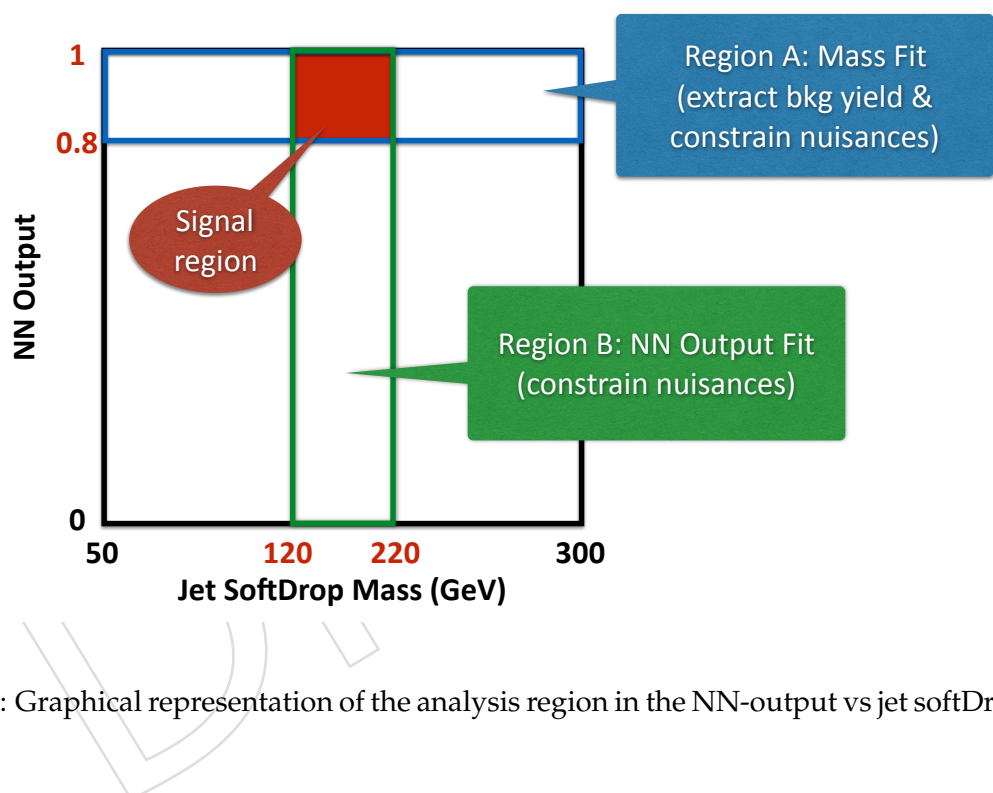


Figure 4: Graphical representation of the analysis region in the NN-output vs jet softDrop mass.

---

<sup>170</sup> **4.3 Multivariate Discriminant**

<sup>171</sup> In order to discriminate between events that come from  $t\bar{t}$  decays and QCD multijet production  
<sup>172</sup> we rely on variables that reveal the jet substructure. In particular, we use the "N-subjettiness"  
<sup>173</sup>  $\tau_N$ , defined as:

$$\tau_N = \frac{1}{\sum_k p_{T,k} R} \sum_k p_{T,k} \min\{\Delta R_{1,k}, \Delta R_{2,k}, \dots, \Delta R_{N,k}\}, \quad (1)$$

<sup>174</sup> where  $N$  denotes the reconstructed candidate subjets and  $k$  runs over the constituent particles  
<sup>175</sup> in the jet. The variable  $\Delta R_{i,k} = \sqrt{(\Delta y_{i,k})^2 + (\Delta \phi_{i,k})^2}$  is the angular distance between the can-  
<sup>176</sup> didate subjet  $i$  and the particle  $k$ . The variable  $R$  is the characteristic jet radius ( $R = 0.8$  in our  
<sup>177</sup> case).

<sup>178</sup> Since the signal final state ( $t\bar{t}$  hypothesis) involves two jets with a top-quark decay signature,  
<sup>179</sup> we consider the N-subjettiness variables  $\tau_{1,2,3}$  for both leading jets in the event, resulting in  
<sup>180</sup> six discriminating variables per event. The distributions of these variables in  $t\bar{t}$  and QCD  
<sup>181</sup> simulated events are shown in Fig. 5, indicating that there is significant separating power in  
<sup>182</sup> them. The linear correlation between the variables is shown in Fig. 6. In order to exploit fully  
<sup>183</sup> the differences of the N-subjettiness variables we turn to multivariate discriminants, imple-  
<sup>184</sup> mented in the TMVA package [40]. As a baseline we consider a simple Fisher discriminant,  
<sup>185</sup> which is a linear combination of the variables. Then, a feed-forward neural network (NN)  
<sup>186</sup> is constructed to enhance the discriminating power quantified by the integral of the receiver-  
<sup>187</sup> operator-characteristic (ROC) curve. The network (Fig. 7) is composed of two hidden layers  
<sup>188</sup> with 16 and 4 nodes, respectively, each of one using a sigmoid activation function. The dis-  
<sup>189</sup> tribution of the NN output and the convergence of its training are shown in Fig. 8. As shown  
<sup>190</sup> in Fig. 9, the NN is clearly better than the simple Fisher discriminant and it also outperforms  
<sup>191</sup> slightly a Boosted Decision Tree composed of 500 trees and trained with the Gradient Boost  
<sup>192</sup> method with shrinkage parameter equal to 0.1. More complicated NN architectures have not  
<sup>193</sup> been found to improve the performance. The training is performed with events that pass the  
<sup>194</sup> baseline selection and the MC samples are divided in two halves, one used for the training and  
<sup>195</sup> one for the testing.

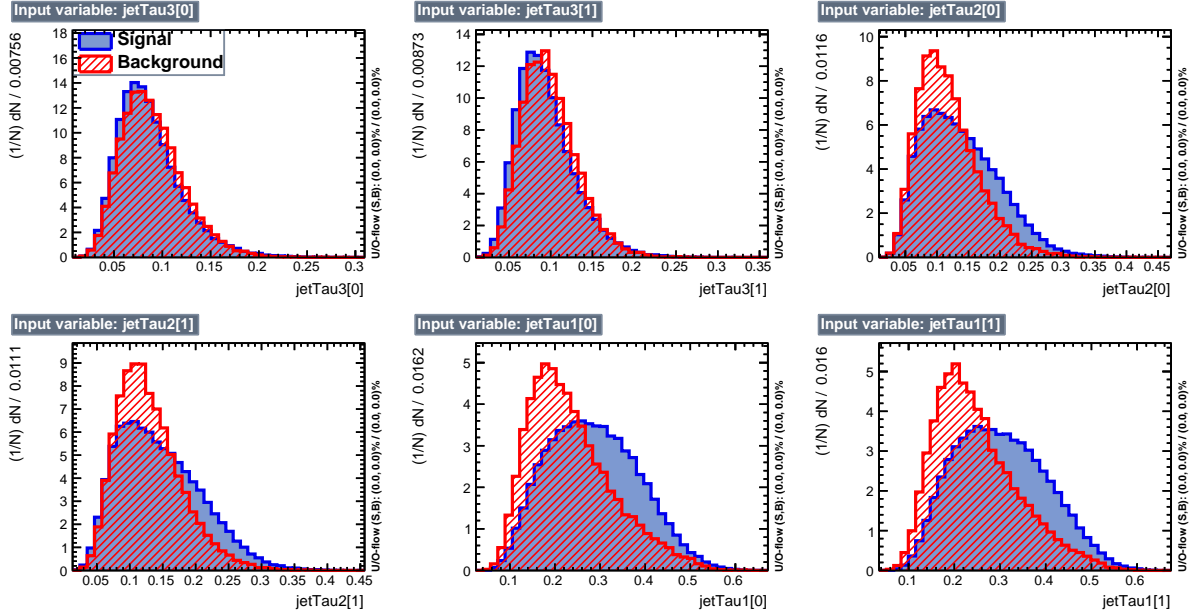


Figure 5: Discriminating variables used for the separation of  $t\bar{t}$  from QCD events.

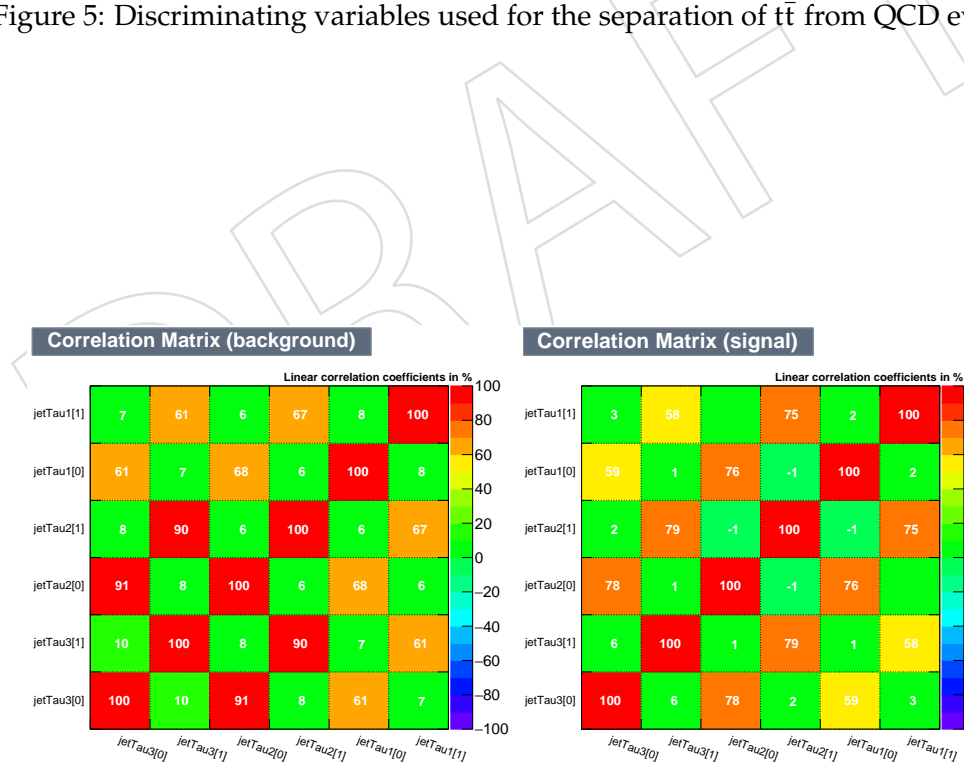


Figure 6: Linear correlation between the discriminating variables in background (left) and signal (right) events.

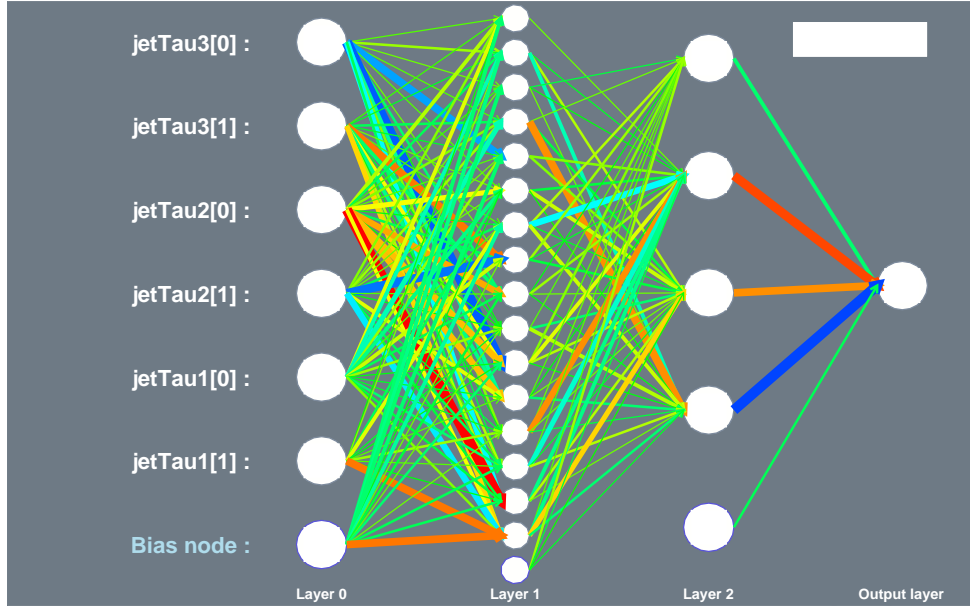


Figure 7: Neural network architecture.

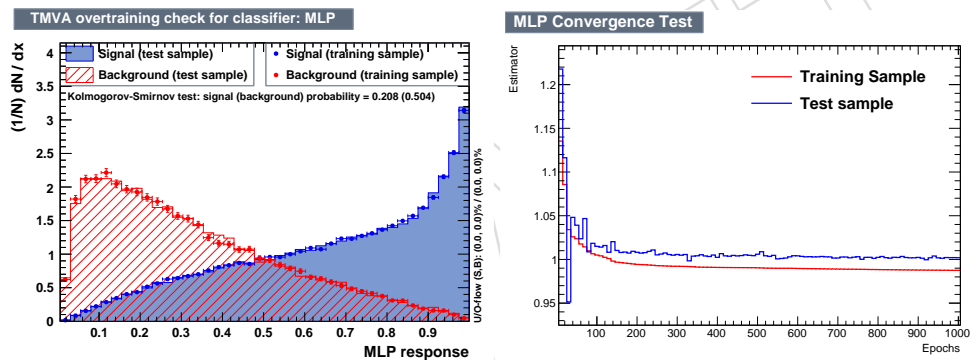


Figure 8: Output of the NN (left). Convergence of the NN training (right).

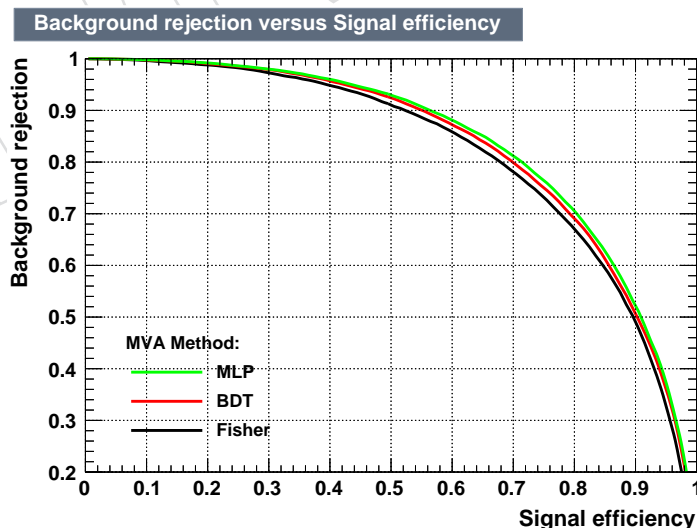


Figure 9: Performance of the multivariate discriminants in the form of a receiver-operator-characteristic curve.

196 **4.4 Parton level**

197 The partonic phase space to which we unfold the measurement is constrained by the kinematic  
 198 requirements of the detector-level fiducial region. Namely, the top and anti-top partons must  
 199 have  $p_T > 400 \text{ GeV}$  and  $|\eta| < 2.4$ , while the invariant mass of the  $t\bar{t}$  system must be greater  
 200 than  $800 \text{ GeV}$  in order to avoid extreme events with high top  $p_T$  and very low  $m_{t\bar{t}}$ . These cuts  
 201 are summarized in Table 6.

Table 6: Definition of parton-level phase space.

Observable	Requirement
$p_T^{t,\bar{t}}$	$> 400 \text{ GeV}$
$ \eta^{t,\bar{t}} $	$< 2.4$
$m_{t\bar{t}}$	$> 800 \text{ GeV}$

202 **4.5 Particle level**

203 The so-called "particle level" represents the state that consists of stable particles originating  
 204 from the proton-proton collision, after the hadronization process, and before the interaction of  
 205 these particles with the detector. The observables computed from the particles' momenta are  
 206 thought to be better defined compared to the ones computed from parton information and ac-  
 207 companied by smaller theoretical uncertainties. Also, the associated phase space is closer to the  
 208 fiducial phase space of the measurement at detector level. In the context of this analysis, parti-  
 209 cle jets are reconstructed from stable particles, excluding neutrinos, with the anti-kt algorithm  
 210 of distance parameter  $R = 0.8$ , identical to the detector-level reconstruction. It should be noted  
 211 that only particles originating from the primary interaction are considered. Subsequently, jets  
 212 that are geometrically matched, within  $\Delta R < 0.4$  in  $\eta - \phi$  from generated leptons (i.e. from the  
 213 leptonic decays of the W boson) are removed from the particle-jet collection. Finally, the two  
 214 particle jets with the highest  $p_T$  are considered the particle-level top-quark candidates. In order  
 215 to match as closely as possible the fiducial phase space, the same kinematic cuts are applied as  
 216 for detector-level events. These requirements are summarized in Table 7.

Table 7: Definition of particle-level phase space.

Observable	Requirement
$N_{\text{jets}}$	$> 1$
$p_T^{\text{jet}1,2}$	$> 400 \text{ GeV}$
$ \eta^{\text{jet}1,2} $	$< 2.4$
$m_{SD}^{\text{jet}1,2}$	(120, 220) GeV
$m_{jj}$	$> 800 \text{ GeV}$

217 In order to verify the sanity of the adopted particle-level definition, in each event that passes  
 218 the requirements above, the top candidates are matched within  $\Delta R < 0.4$  in  $\eta - \phi$  to the original  
 219 top quarks at parton level. Figure 47 shows this efficiency, which varies between 96% and 98%,  
 220 as a function of particle-level top  $p_T$  and  $\eta$ .

221 **5 Data vs Monte Carlo**

222 In this section we present comparisons between data and Monte Carlo for various observables.  
 223 It should be noted that the  $t\bar{t}$  normalization is scaled by a factor 0.6, consistent with the findings  
 224 of Section 9, and the QCD background yield is adjusted such that the total Monte Carlo events

225 are equal to the events in data. Table 8 shows the event yields for the various processes after  
 226 applying the baseline selection plus the requirement that both AK8 jets contain a b-tagged  
 227 subjet, with or without the NN cut (see Section 4 for details on the selection requirements).  
 228 Already after the b-tagging requirement the  $t\bar{t}$  signal is sufficiently enhanced that it becomes  
 229 visible. Finally, the NN cut suppresses QCD by a factor  $\sim 17$  with a signal loss of  $\approx 45\%$ . In  
 230 the signal region the signal-over-background ratio is  $\approx 1.8$ .

Table 8: Expected and observed event yields in  $SR_A$ .

Process	No NN cut	With NN cut
$t\bar{t}$	10881	5867
QCD	85155	4930
$W+jets$	857	110
$Z+jets$	784	59
Single Top	753	211
Data	98430	11177

Table 9: Expected and observed event yields in the signal region.

Process	Yield
$t\bar{t}$	3978
QCD	2171
$W+jets$	51
$Z+jets$	12
Single Top	83
Data	6295

231 Figure 10 shows the softDrop mass of the leading jet (one entry per event), which serves as a  
 232 proxy for the top mass. Figure 11 shows the mass of the  $W$  candidate. This is defined as the  
 233 leading AK4 subjet in the leading AK8 jet and it is selected if the event satisfies the signal region  
 234 selection and if it has  $p_T > 300$  GeV while it is not b-tagged ( $CSV < 0.8484$ ). The distribution  
 235 of the NN output is shown in Fig. 12.

236 The kinematic properties of jets (two entries per event) in the signal region are shown in Fig. 13,  
 237 while those of the  $t\bar{t}$  system are shown in Fig. 14. Finally, the jet substructure properties (n-  
 238 subjettiness variables) are shown in Fig. 15.

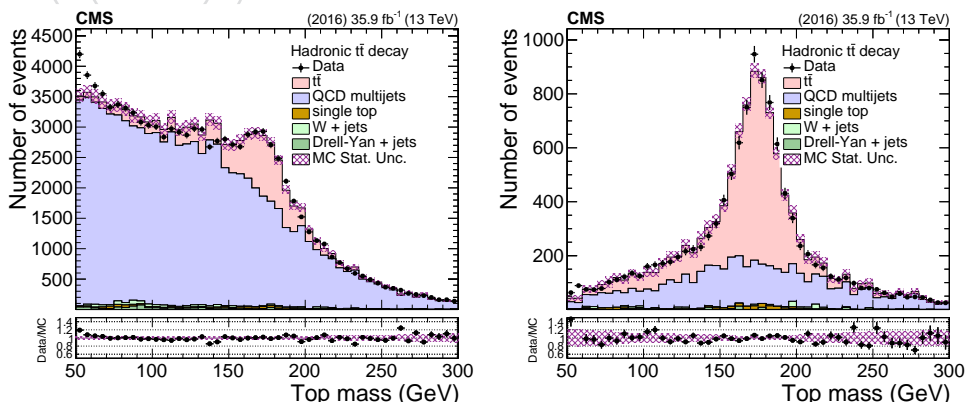


Figure 10: SoftDrop mass of the leading AK8 jet after the baseline selection with both AK8 jets containing a b-tagged subjets, with (right) and without (left) the  $NN > 0.8$  cut.

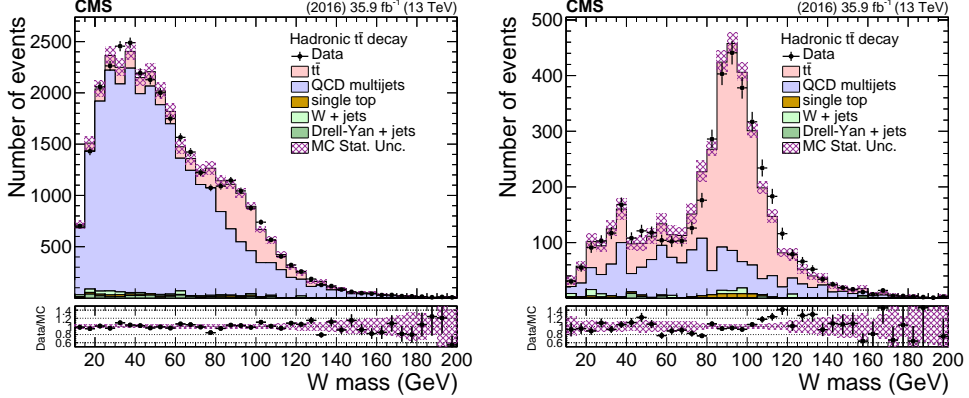


Figure 11: SoftDrop mass of the W candidate jet after the baseline selection with both AK8 jets containing a b-tagged subjets, with (right) and without (left) the  $NN > 0.8$  cut.

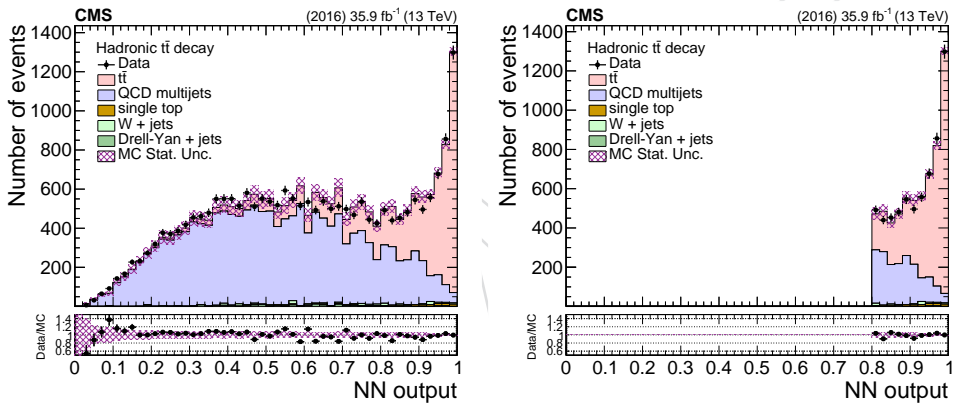


Figure 12: NN output after the baseline selection with both AK8 jets containing a b-tagged subjets, with (right) and without (left) the  $NN > 0.8$  cut.

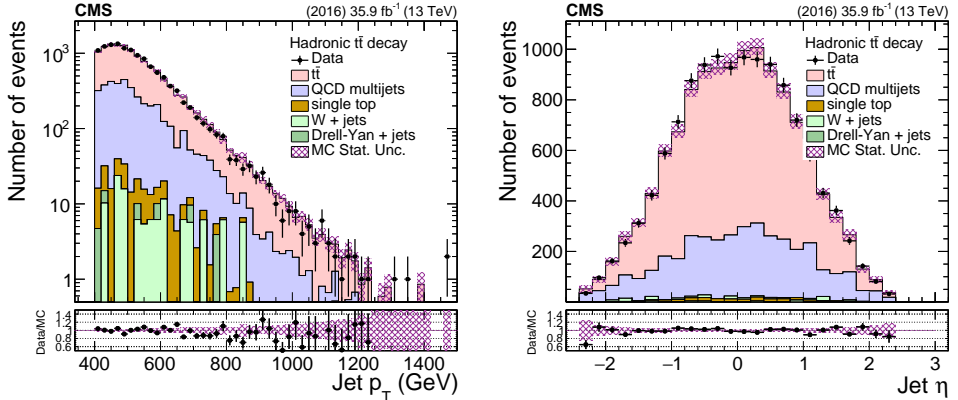


Figure 13: Jet  $p_T$  (left) and  $\eta$  (right) distributions in the signal region. The plots contain two entries per event (for the leading and trailing jets).

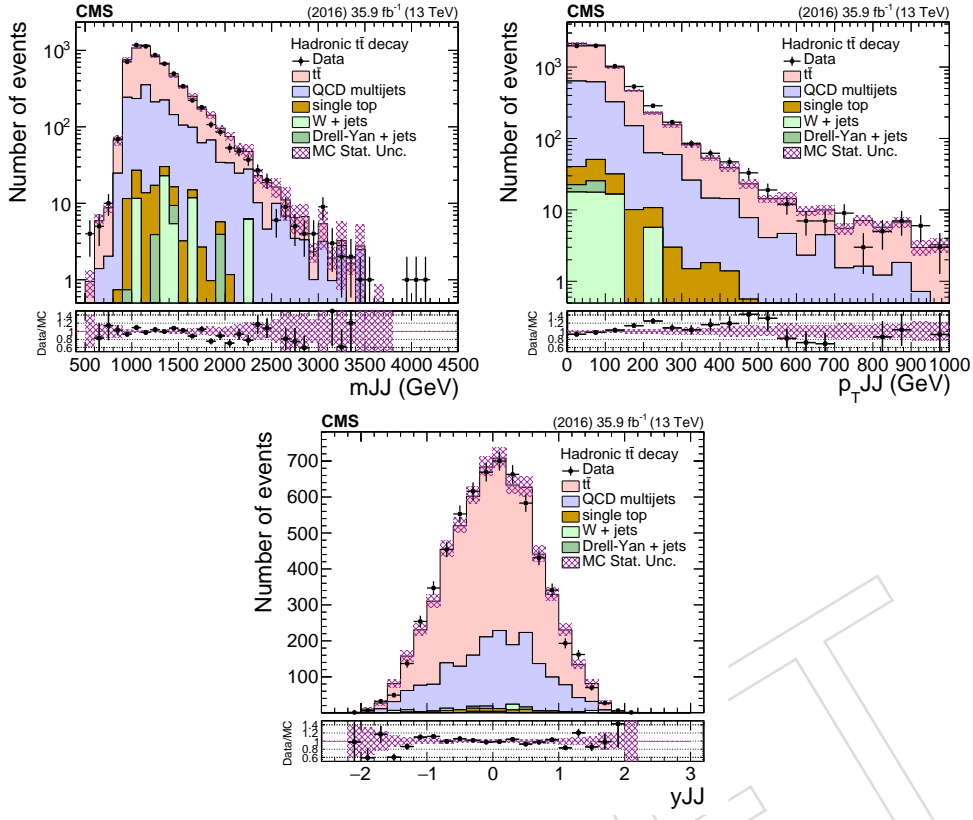


Figure 14: Kinematic distributions of the  $t\bar{t}$  system in the signal region.

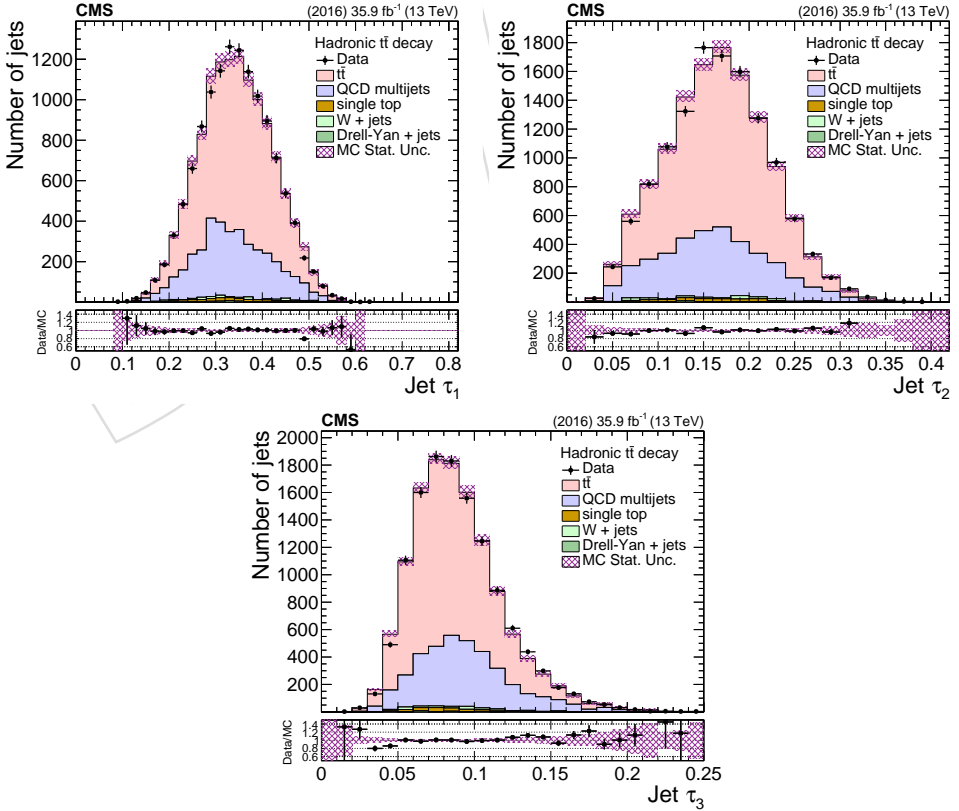


Figure 15: N-subjettiness variables for the two leading jets in the signal region.

## 239 6 Background

240 The, by far, dominant background in this analysis is the QCD multijet production, as there is  
 241 a finite probability that ordinary jets, from single parton radiation, will mimic the topological  
 242 substructure of a top-decay jet. With a combination of b-tagging requirements on the subjets  
 243 and n-subjettiness variables, we are able to suppress significantly the QCD background, as  
 244 shown in Section 5. In order to estimate the remaining contribution we employ a data-driven  
 245 technique based on the assumptions that if the b-tagging requirement is reverted we a) get a  
 246 pure QCD sample, and b) the jet kinematic properties are not affected.

247 The two elements that need to be determined from data are the shape  $Q(x)$  of the QCD back-  
 248 ground as a function of an observable of interest  $x$ , and the absolute normalization  $N_Q$ . The  
 249 QCD template  $Q(x)$  is taken from the QCD control sample by applying the signal region selec-  
 250 tion with reverted b-tagging requirement (none of the leading AK8 jets is allowed to contain a  
 251 b-tagged subjet). Figures 16,17 show the closure test in MC as a function of jet and dijet kine-  
 252 matic variables. We observe that, within the statistical precision of the simulation, the shapes  
 253 are compatible, regardless of the b-tagging requirement. Moreover, Figs. 19,20 show that in-  
 254 deed the 0-btag sample has negligible  $t\bar{t}$  contamination.

255 The normalization of the QCD background is determined from a fit to the data in signal re-  
 256 gion A (Section 4) on the softDrop mass of the top candidate. However, since this is an  
 257 extended signal region (in order to allow for QCD dominated sidebands), a transfer factor  
 258  $R_{yield} = N^{SR}/N^{SR_A}$  is needed in order to get the QCD normalization in the signal region. This  
 259 transfer factor is different for the  $t\bar{t}$  kinematic variables (one entry per event) and the top vari-  
 260 ables (two entries per event). Figure 18 shows a closure test performed in QCD Monte Carlo  
 261 events, where the value of  $R_{yield}$  is independent of the b-tagging requirement (within the sta-  
 262 tistical precision of the simulation), and therefore can be taken from the QCD control sample  
 263 ( $R_{yield} = N^{CR}/N^{CR_A}$ ).

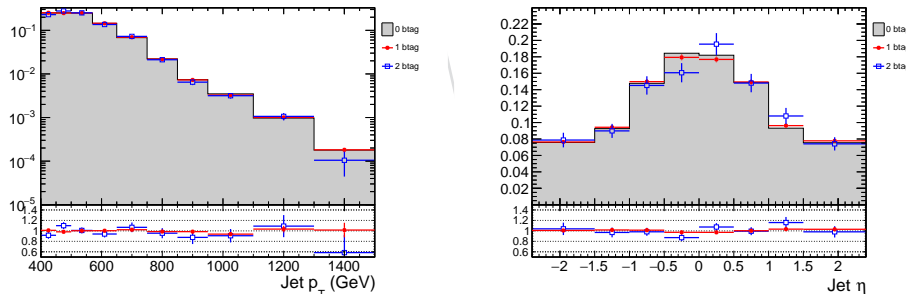


Figure 16: Closure test for the data-driven QCD prediction method for the shape of the top  $p_T$  and  $\eta$  variables.

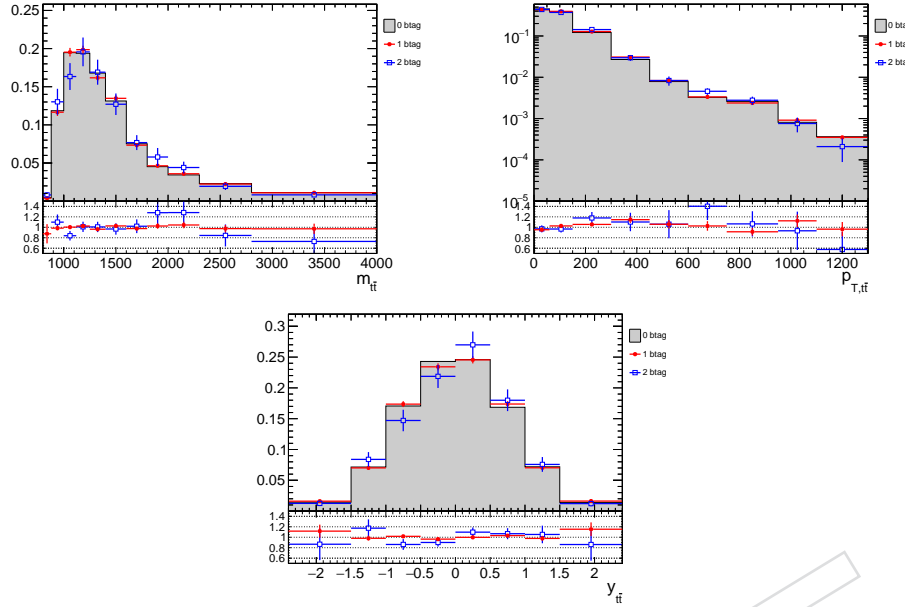


Figure 17: Closure test for the data-driven QCD prediction method for the shape of the  $t\bar{t}$  variables.

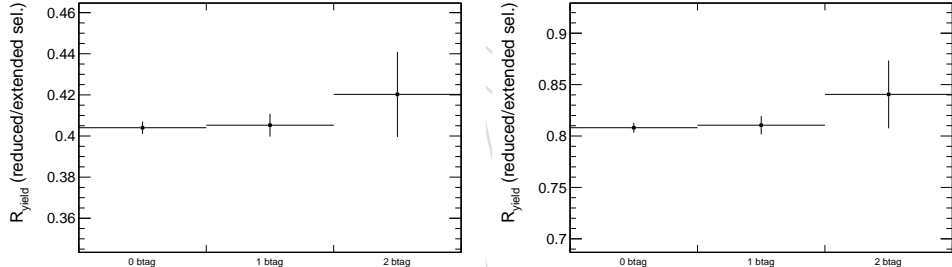


Figure 18: Closure test for the data-driven QCD prediction method for event yield ratio between the control and signal regions. left  $t\bar{t}$  properties (one entry per event). right top properties (two entries per event).

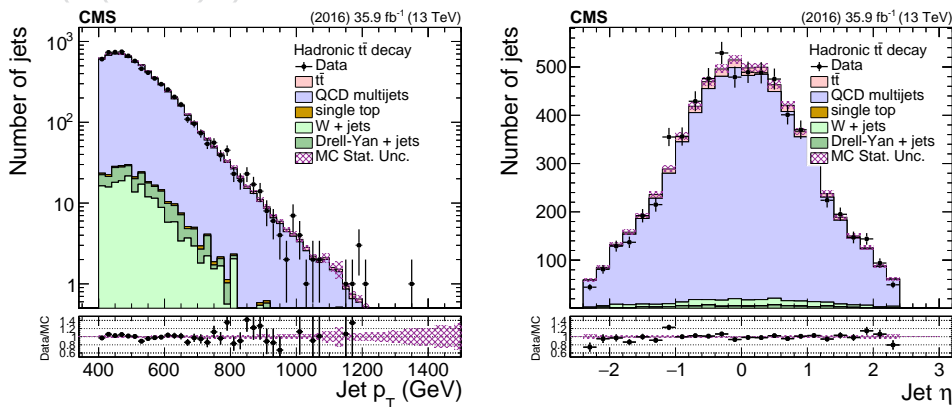


Figure 19: Jet  $p_T$  (left) and  $\eta$  (right) distributions in the QCD control region. The plots contain two entries per event (for the leading and trailing jets).

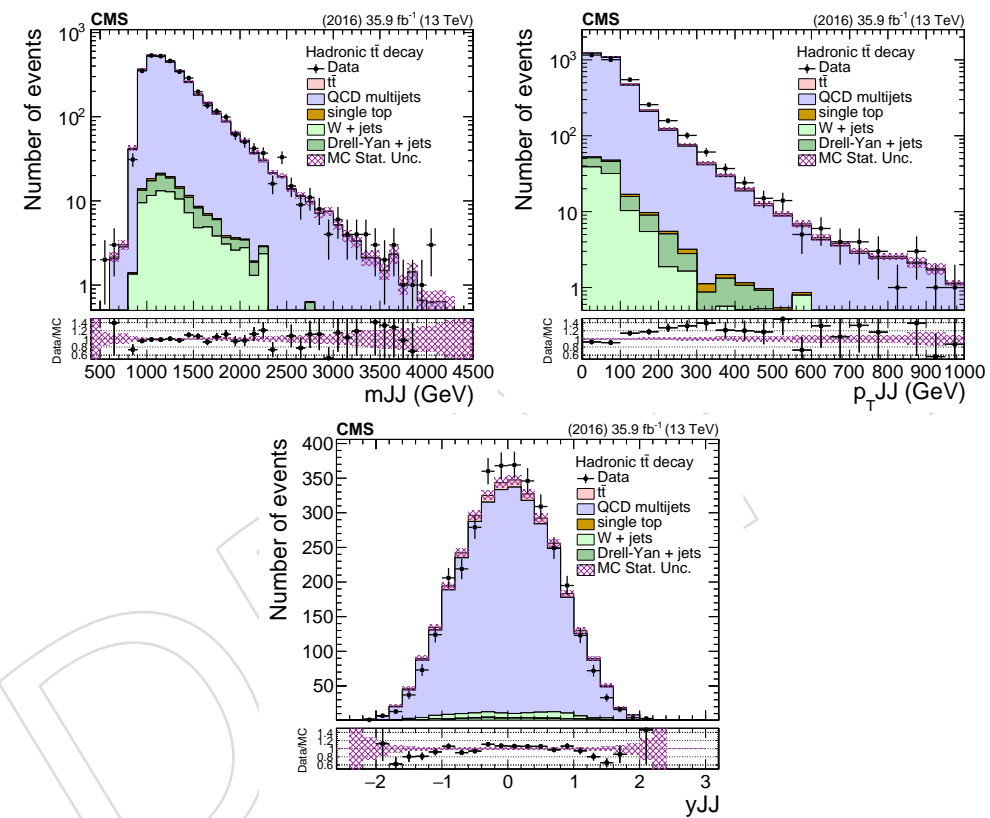


Figure 20: Kinematic distributions of the  $t\bar{t}$  system in the QCD control region.

---

<sup>264</sup> **7 Signal Extraction**

<sup>265</sup> The  $t\bar{t}$  signal is extracted from data, differentially, as a function of five variables (top  $p_T$  and  $\eta$ ,  
<sup>266</sup>  $t\bar{t}$  mass,  $p_T$ , and rapidity) by subtracting the contribution of the backgrounds:

$$S(x) = D(x) - R_{\text{yield}} N_{\text{qcd}} Q(x) - B(x), \quad (2)$$

<sup>267</sup> where  $x = p_T^t, \eta^t, m^{t\bar{t}}, p_T^{t\bar{t}}, y^{t\bar{t}}$ ,  $S(x)$  is the signal,  $D(x)$  is the measured distribution in data,  $Q(x)$   
<sup>268</sup> is the QCD shape,  $B(x)$  is the subdominant backgrounds' contribution (both the shape and the  
<sup>269</sup> normalization are taken from the simulation),  $R_{\text{yield}}$  is the yield ratio between the signal region  
<sup>270</sup> and the fit region, and  $N_{\text{qcd}}$  is the fitted number of QCD events in  $SR_A$ .

<sup>271</sup> The quantity  $N_{\text{qcd}}$  is estimated from a fit to the data in  $SR_A$  on the mass of the top candidate,  
<sup>272</sup> which is the softDrop mass of the leading jet. The fit is described by the equation below:

$$D_{SR_A}(m^t) = N_{t\bar{t}} T(m^t; k_{\text{scale}}, k_{\text{res}}) + N_{\text{qcd}} (1 + k_{\text{slope}} m^t) Q_{CR_A}(m^t) + N_{\text{bkg}} B(m^t) \quad (3)$$

<sup>273</sup> which contains the shapes (templates)  $T(m^t)$ ,  $B(m^t)$  of the signal and the subdominant back-  
<sup>274</sup> grounds, respectively, taken from the simulation, and the shape  $Q(m^t)$  of QCD taken from the  
<sup>275</sup> control sample in data. The templates of the various components are shown in Figs. 21,22. To  
<sup>276</sup> account for the difference observed in the closure test of QCD for the  $m^t$  variable (Fig. 23) we  
<sup>277</sup> introduced the linear modification factor  $(1 + k_{\text{slope}} m^t)$ , inspired by the simulation, but with  
<sup>278</sup> the slope parameter  $k_{\text{slope}}$  left free in the fit. Also free in the fit are the normalization factors  
<sup>279</sup>  $N_{t\bar{t}}$ ,  $N_{\text{qcd}}$ , and  $N_{\text{bkg}}$ . Finally, we introduce two more nuisance parameters in the  $t\bar{t}$  simulation,  
<sup>280</sup>  $k_{\text{scale}}$  and  $k_{\text{res}}$ , which account for possible differences between data and simulation in the scale  
<sup>281</sup> and resolution of the  $m^t$  parameter. The fit model is imported to the RooFit package and the fit  
<sup>282</sup> result is shown in Fig. 24 while the fitted parameters are summarized in Table 10. We observe  
<sup>283</sup> that the fitted  $t\bar{t}$  yield (6238) is significantly lower than the expectation (9604), which implies  
<sup>284</sup> that the fiducial cross section is  $\approx 35\%$  lower compared to the Powheg+Pythia8 prediction.  
<sup>285</sup> The nuisance parameters related to the  $m^t$  scale and resolution are consistent with one and the  
<sup>286</sup> slope of the QCD modification factor  $(5.7 \pm 1.4) \times 10^{-3}$  is very close to the value from the QCD  
<sup>287</sup> simulation  $((5.4 \pm 1.2) \times 10^{-3})$ . Finally, despite the large uncertainty, the yield of the subdomi-  
<sup>288</sup> nant backgrounds  $(400 \pm 247)$  is very close to the Monte Carlo prediction (380) in Table 8. The  
<sup>289</sup> overall sanity of the fit and the consistency of the results allows us to use the measured  $N_{\text{qcd}}$   
<sup>290</sup> for the extraction of the signal distribution.

Table 10: Results of the fit in  $SR_A$ .

Parameter	Value	Error
$k_{\text{res}}$	0.960	0.026
$k_{\text{scale}}$	1.002	0.002
$k_{\text{slope}}$	5.7e-03	1.4e-03
$N_{\text{bkg}}$	400	255
$N_{\text{qcd}}$	4539	247
$N_{t\bar{t}}$	6238	181

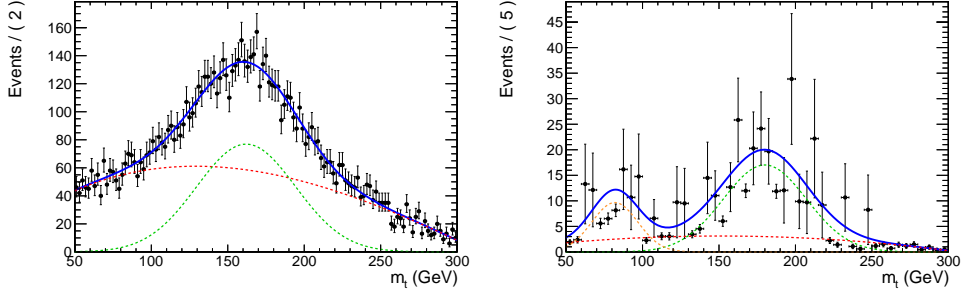


Figure 21: Templates of QCD (left), taken from data, and of the subdominant backgrounds (right), taken from the simulation. The different lines show the individual components (frozen in the fit) used to describe the shapes. The QCD shape is composed of a smooth polynomial and a Gaussian, while the shape of the subdominant backgrounds contains a smooth polynomial and two Gaussians (one describes the W resonance from the single top and WJets processes and the other describes the broader peak from the kinematic selections).

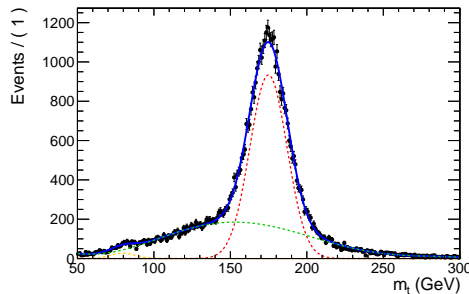


Figure 22: Template of the  $t\bar{t}$  signal taken from the simulation. The different lines show the individual components (frozen in the fit) used to describe the shape. The shape consists of a smooth polynomial and two Gaussians (one describes the W resonance from unmerged top decays and the other describes the fully merged top resonance).

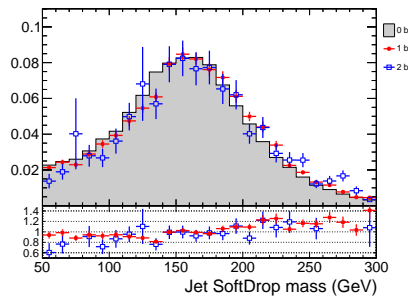


Figure 23: Closure test in the QCD simulation for the shape of the  $m^t$  variable in the three possible b-tagging requirements (none, exactly one, or both jets contain a b-tagged subject).

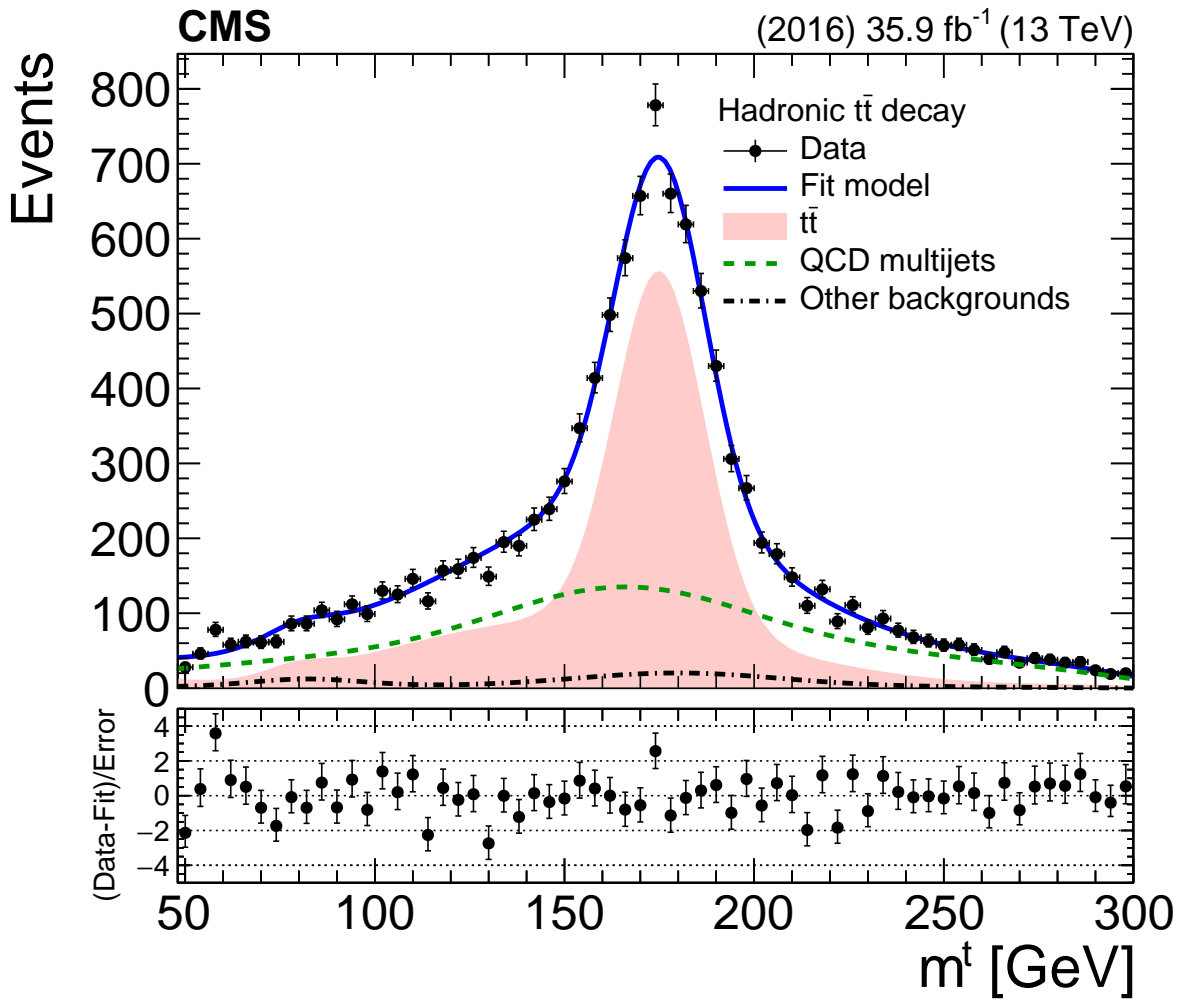


Figure 24: Result of the template fit on data. The red line shows the  $t\bar{t}$  contribution, the green line shows the QCD, and the brown line shows the subdominant backgrounds.

## 291 8 Systematic Uncertainties

292 The systematic uncertainties considered in this analysis are divided in two categories: exper-  
 293 imental and theoretical. The former includes all the uncertainties related to the differences in  
 294 the object performance between data and simulation. The latter are related to the simulation it-  
 295 self and affect primarily the unfolded results through the acceptance, efficiency, and migration  
 296 matrix. The list below describes briefly these uncertainties and the way they have been han-  
 297 dled here. It should be noted that for each systematic variation the differential cross sections  
 298 (fiducial and unfolded) are re-measured and the difference with respect to the nominal result  
 299 is taken as the effect of this variation to the measurement.

### 300 1. Experimental Uncertainties

- 301 • QCD background prediction: we use the fitted QCD yield uncertainty. The  
   302 shape uncertainties due to the closure test in the simulation and the different  
   303 pileup profiles in the control and signal regions are very small, at the 1% level.
- 304 • *Jet energy scale (JES)*: this is the uncertainty on the energy scale of each recon-  
   305 structed jet and it is a leading experimental uncertainty. Following the rec-  
   306 commendations of the JME group, we have considered 24 independent JES  
   307 sources [41] as follows: for each variation a new jet collection is created and  
   308 the event interpretation is repeated. This results not only in variations of the  
   309  $p_T$  scale itself, but may also lead to different top candidates. The JES uncer-  
   310 tainty, per jet, is of the order 1 – 2%,  $p_T$  and  $\eta$  dependent. The effect on the  
   311 measured cross section is typically of the order 10% but it can be much larger  
   312 at very high jet  $p_T$ .
- 313 • *Jet energy resolution*: The impact on the measurement due to the jet energy res-  
   314 olution (JER) is determined by smearing the jets according to the JER uncer-  
   315 tainty. The effect on the cross section is relatively small, at the level of 2%.
- 316 • *Subjet b tagging efficiency (hadronic)*: The uncertainty in the identification of b-  
   317 subjets within the large- $R$  jets (estimated in [42]) is a leading experimental  
   318 uncertainty in the hadronic channel. The effect on the cross sections is of the  
   319 order of 10% relatively flat in all the observables. Unlike the uncertainty asso-  
   320 ciated with the JES, the b-subjet tagging uncertainty therefore largely cancels  
   321 in the normalized cross sections.
- 322 • *Pileup*: The uncertainty related to the modeling of additional pileup interac-  
   323 tions is a subdominant uncertainty. The impact on the measurement is esti-  
   324 mated by varying the total inelastic cross section used to weight the simulated  
   325 events by  $\pm 4.6\%$ . The effect on the cross sections is negligible (below 1%).
- 326 • Trigger: this accounts for the difference between the simulated and observed  
   327 trigger efficiency. Based on Fig. 2 the uncertainty is well below 1% in the phase  
   328 space of this analysis.
- 329 • *Luminosity*: The uncertainty in the measurement of the integrated luminosity  
   330 is 2.5% [43].

### 331 2. Theoretical Uncertainties

332 The theoretical uncertainties are divided into two sub-categories: the ones related to the  
 333 matrix element of the hard process and the ones related to the modelling of the parton  
 334 shower and the underlying event. Practically, the first category (consisting of the first  
 335 three sources below) is evaluated by variations of LHE event weights stored in the nom-  
 336 inal MC simulation, while the second category is evaluated with dedicated, alternative

337 MC samles.

- 338     ● *Parton distribution functions*: The uncertainty due to parton distribution func-  
339       tions (PDFs) is estimated by applying event weights corresponding to the 100  
340       replicas of the NNPDF set. For each observable we compute its standard devi-  
341       ation from the 100 variations.
- 342     ● *Renormalization and factorization scales*: This source of systematic uncertainty is  
343       estimated by applying event weights corresponding to different factorization  
344       and renormalization scale options. For each observable the largest deviation  
345       from the nominal scales is taken.
- 346     ● *Strong coupling constant ( $\alpha_S$ )*: The uncertainty associated with the  $\alpha_S$  is esti-  
347       mated by applying event weights corresponding to higher and lower values  
348       of  $\alpha_S$  for the matrix element.
- 349     ● *Final state radiation (FSR)*: this uncertainty is estimated from alternative MC  
350       samples with reduced and increased value for the strong coupling constant  
351       used by Pythia8 to generate final state radiation. The original variations are  
352       largely exaggerated, as seen in Fig. 25, where the alternative samples fail miserably  
353       to describe the data in two sensitive observables: the mass of the top  
354       candidate jet and the NN output, both of which rely on the dynamics of the jet  
355       formation. In order to use a more realistic estimate of this uncertainty, a max-  
356       imum likelihood fit is performed (independently) on these variables, using  
357       the systematic uncertainties as independent nuisance parameters. The fits are  
358       implemented through the “Combine” toolbox using templates for the various  
359       components and are shown in Fig. 26. The fit on the  $m^t$  variable is well be-  
360       haved in the entire fit range, while the fit on the NN output is less successful  
361       in the background-enriched region. Nevertheless, since it is the signal uncer-  
362       tainties that we wish to constrain, the signal region is fitted perfectly. As a re-  
363       sult of these fits, the nuisances are constrained in-situ. Figures 27 and 28 show  
364       the comparison of the pre-fit and post-fit uncertainties, as well as the pulls of  
365       the nuisance parameters. Both fits indicate that the post-fit FSR nuisance is  
366       actually close to its pre-fit (nominal) value with a significant reduction of its  
367       uncertainty. Based on the observations from the fits, we have scaled down the  
368       effects of the FSR variations by a (conservative) factor 0.3.
- 369     ● *Initial state radiation (ISR)*: this uncertainty is estimated from alternative MC  
370       samples with reduced and increased value for the strong coupling constant  
371       used by Pythia8 to generate initial state radiation.
- 372     ● *Matrix element – parton shower matching*: In the POWHEG matrix element to par-  
373       ton shower (ME-PS) matching scheme, the resummation damping factor  $h_{\text{damp}}$   
374       is used to regulate high- $p_T$  radiation. Uncertainties in  $h_{\text{damp}}$  are parameterized  
375       by considering alternative simulated samples with  $h_{\text{damp}}$  varied by  $\pm 1\sigma$ .
- 376     ● *Underlying event tune*: This uncertainty is estimated from alternative Monte  
377       Carlo samples with the tune CUETP8M2T4 parameters varied by  $\pm 1\sigma$ .

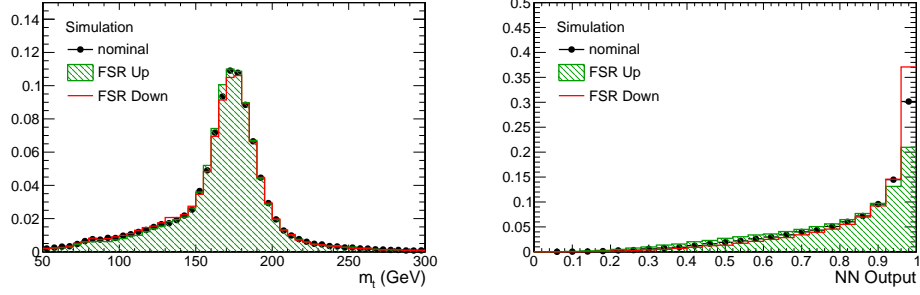


Figure 25: Variations of the  $m^t$  (left) and NN output (right) distributions due to the alternative FSR MC samples.

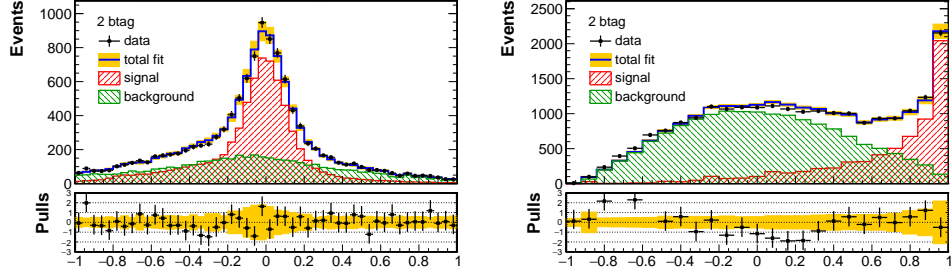


Figure 26: Fit to the  $m^t$  (left) and NN output (right) distributions aiming to constrain the MC modelling uncertainties.

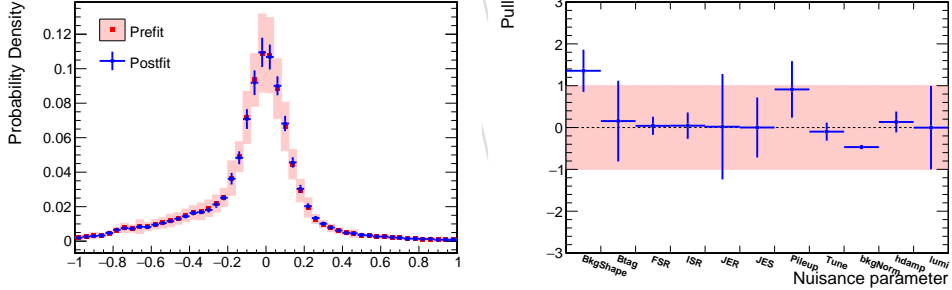


Figure 27: (left) Comparison between the prefit and postfit distributions and uncertainties of the  $m^t$  distribution. (right) Fit pulls of the nuisance parameters.

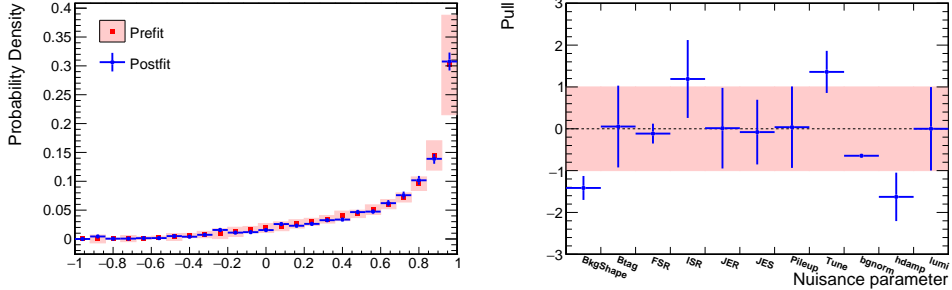


Figure 28: (left) Comparison between the prefit and postfit distributions and uncertainties of the NN output distribution. (right) Fit pulls of the nuisance parameters.

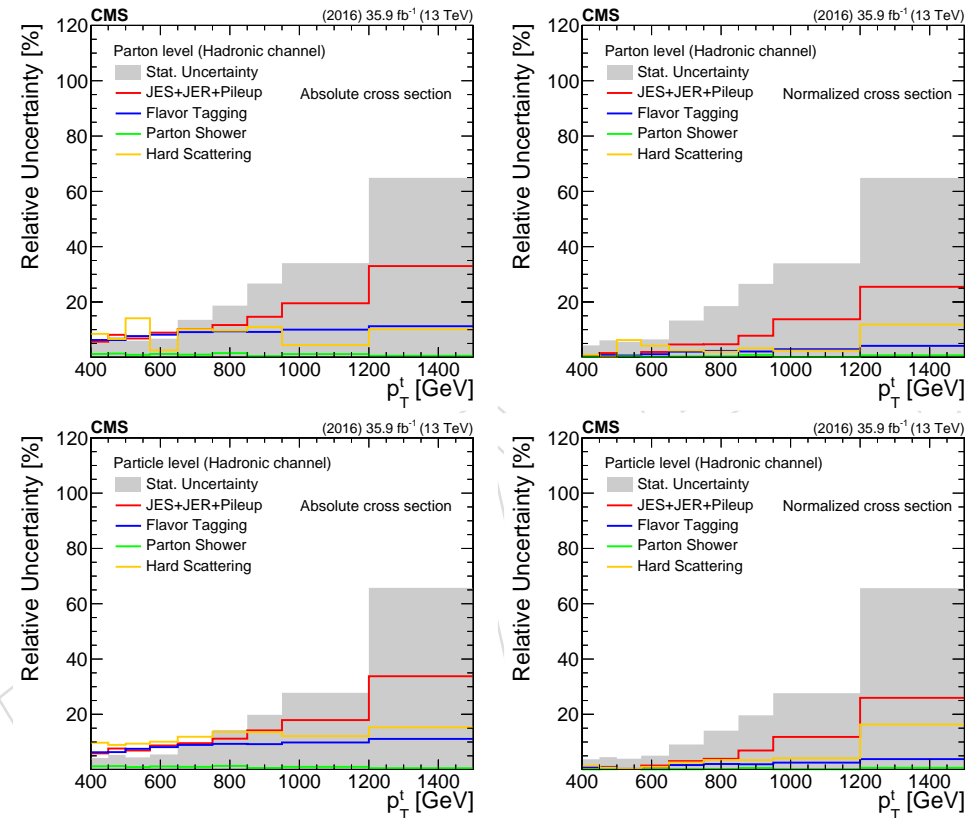


Figure 29: Decomposition of uncertainties for the parton- and particle-level measurement (left: absolute, right: normalized) as a function of top  $p_T$ .

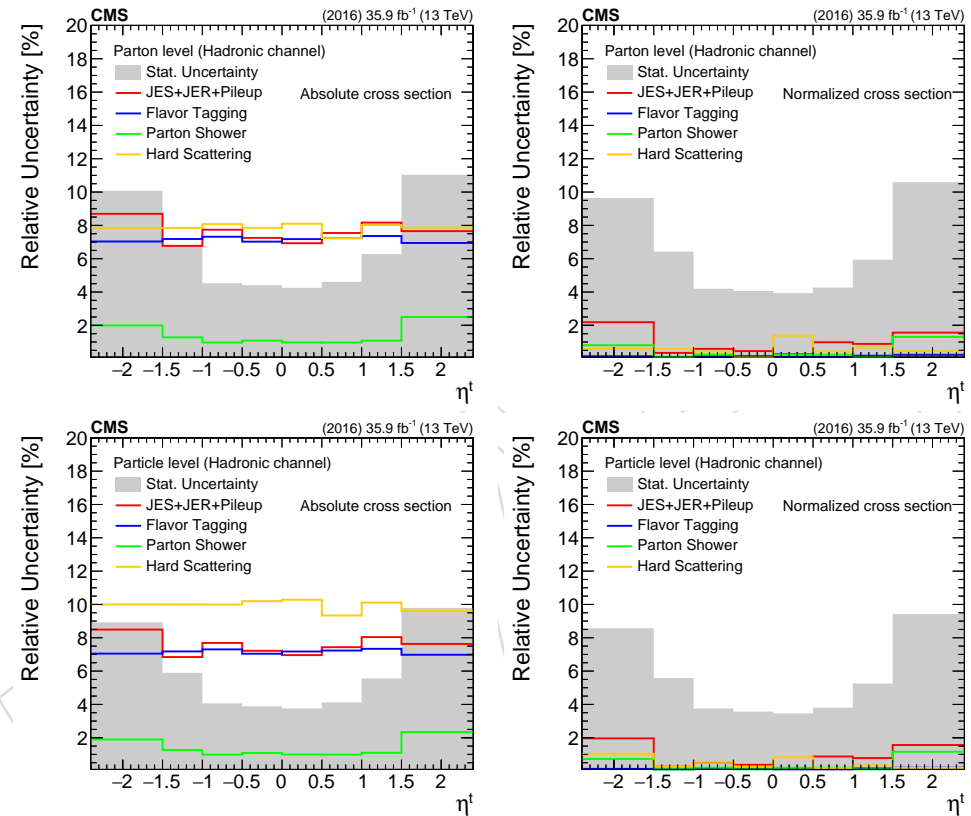


Figure 30: Decomposition of uncertainties for the parton- and particle-level measurement (left: absolute, right: normalized) as a function of top  $\eta^t$ .

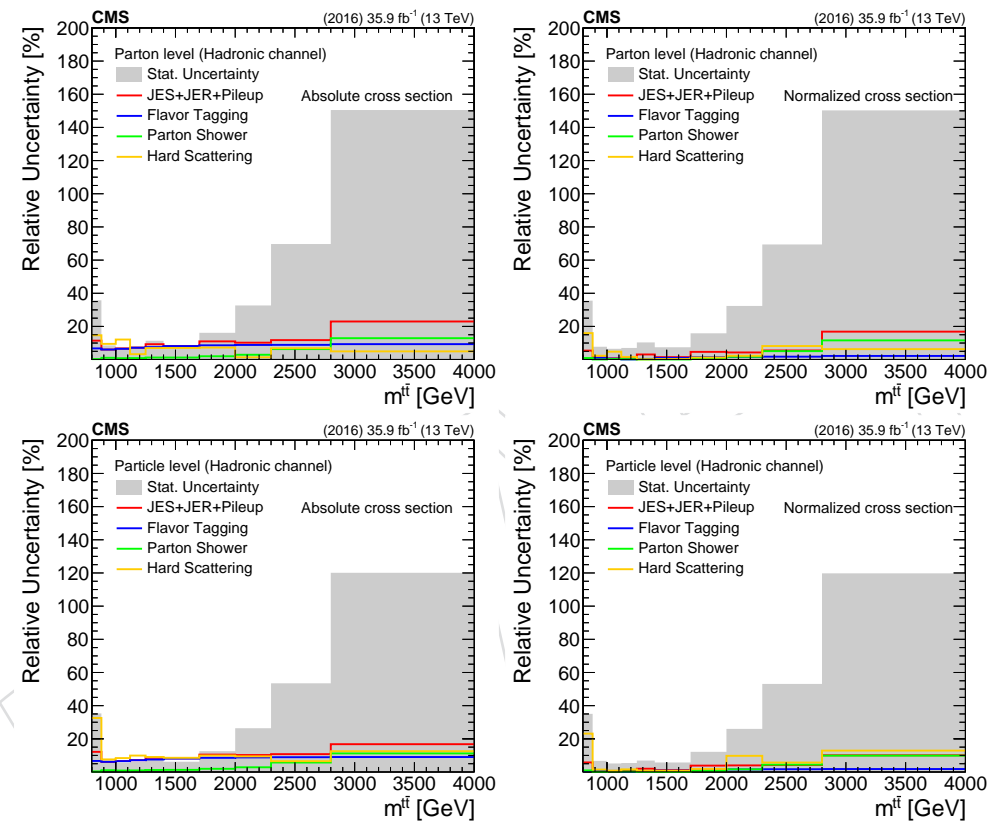


Figure 31: Decomposition of uncertainties for the parton- and particle-level measurement (left: absolute, right: normalized) as a function of  $m_{t\bar{t}}$ .

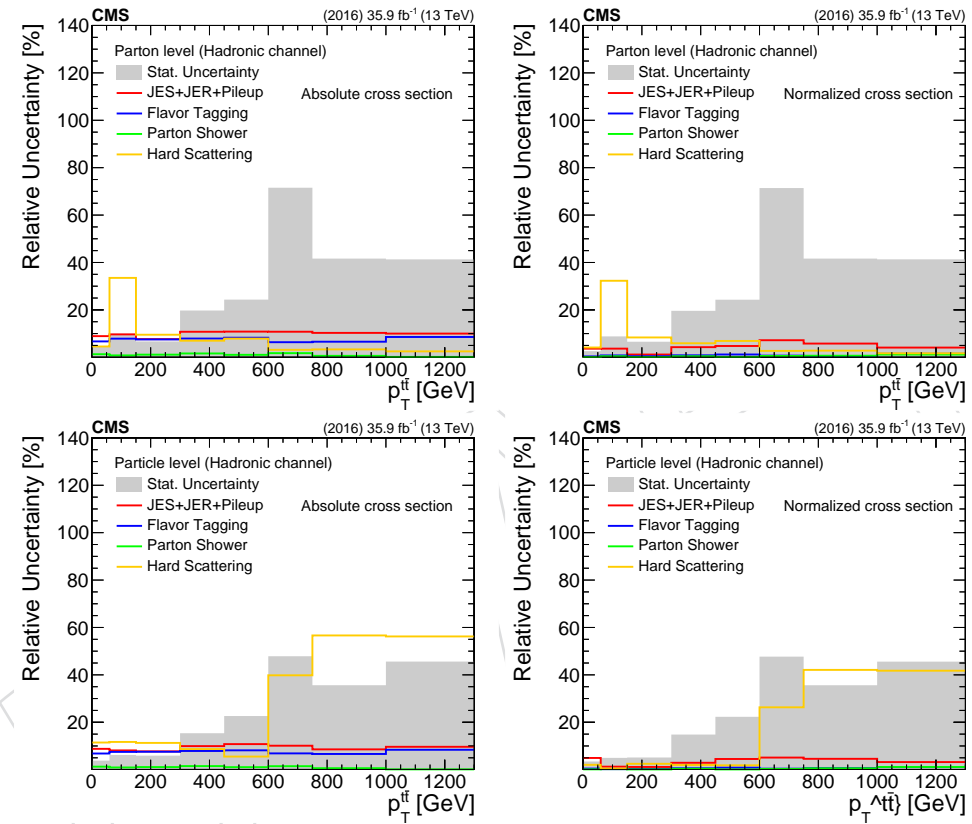


Figure 32: Decomposition of uncertainties for the parton- and particle-level measurement (left: absolute, right: normalized) as a function of  $p_T^{\text{tt}}$ .

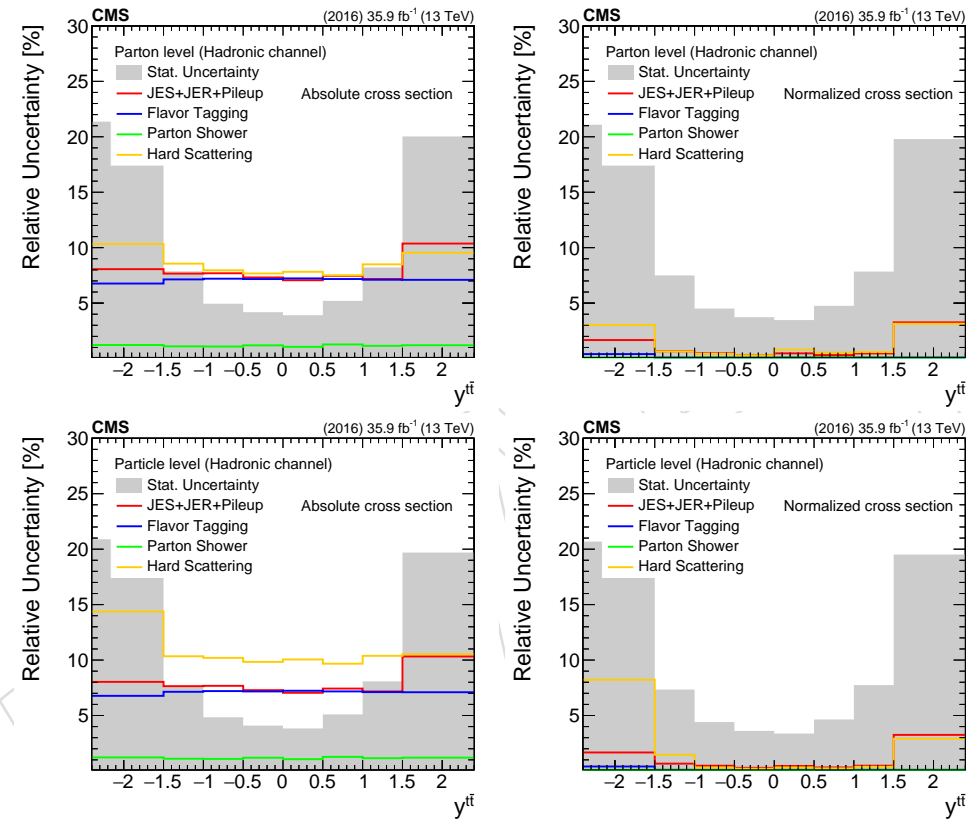


Figure 33: Decomposition of uncertainties for the parton- and particle-level measurement (left: absolute, right: normalized) as a function of  $y_{t\bar{t}}$ .

## 378 9 Fiducial Measurement

379 The fiducial differential cross section is derived in bin  $i$  of the variable  $x$  from the signal yield  
 380  $S_i$  (eq. 2) in the bin as follows:

$$\frac{d\sigma_i^{\text{fid}}}{dx} = \frac{S_i}{\mathcal{L} \cdot \Delta x_i}, \quad (4)$$

381 where  $\mathcal{L}$  is the total integrated luminosity and  $\Delta x_i$  is the width of the  $i$ -th bin of the observable  
 382  $x$ . Of particular interest is also the normalized cross section, computed as:

$$\frac{1}{\sigma^{\text{fid}}} \frac{d\sigma_i^{\text{fid}}}{dx} = \frac{1}{\sum_k S_k} \cdot \frac{S_i}{\mathcal{L} \cdot \Delta x_i}, \quad (5)$$

383 which is used to confront the modelling of the differential cross section regardless of the overall  
 384 normalization. In order to estimate the uncertainty on the measurement, the entire procedure is  
 385 repeated for every source of uncertainty described in Section 8. Both the experimental and the  
 386 theoretical uncertainties affect primarily the  $t\bar{t}$  singal shape, which is used to fit the data for the  
 387 QCD background normalization. As a result the total systematic uncertainty of the measure-  
 388 ment is small and the statistical uncertainty dominates. This is true both for the absolute and  
 389 the normalized cross sections. Figures 34-38 show the fiducial cross sections as a function of  
 390 the variables of interest. Firstly, we observe the expected offset of about 40% in the total cross  
 391 section between the data and the Powheg+Pythia8 prediction, which is considerably smaller  
 392 for the other theory predictions. In particular the Powheg+Herwigpp seems to agree best (this  
 393 is most visible in Fig. 35). In terms of shape comparisons, the Powheg+Pythia8 prediction is in  
 394 excellent agreement with data for all the variables, except for the invariant mass  $m_{t\bar{t}}$  of the  $t\bar{t}$   
 395 system, where the theoretical spectrum appears to be harder above  $\approx 2$  TeV. A similar behavior  
 396 is observed for the other theory models with hints of somewhat larger differences, although the  
 397 statistical precision of the predictions does not allow quantitative comparisons.

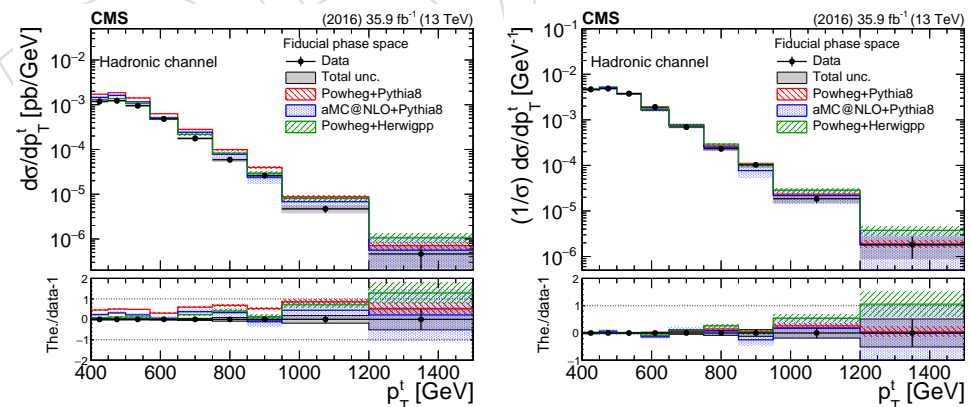


Figure 34: Fiducial differential cross section, absolute (left) and normalized (right), as a function of top  $p_T$ . The bottom panel shows the ratio (theory - data)/data.

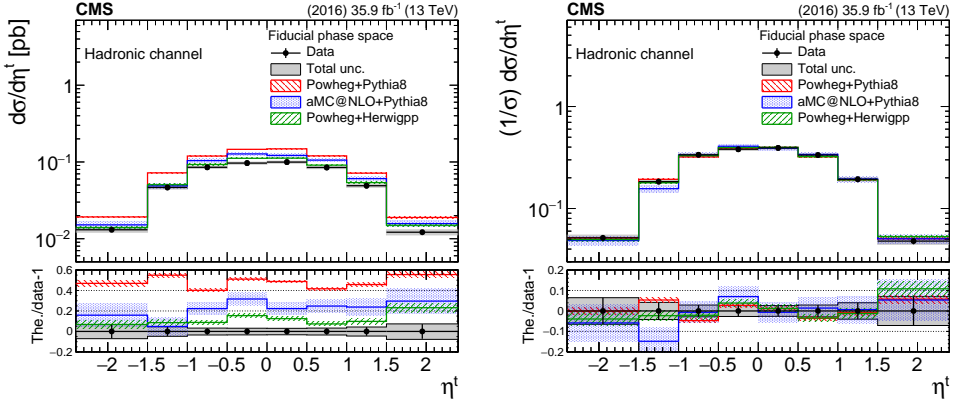


Figure 35: Fiducial differential cross section, absolute (left) and normalized (right), as a function of top  $\eta$ . The bottom panel shows the ratio (theory - data)/data.

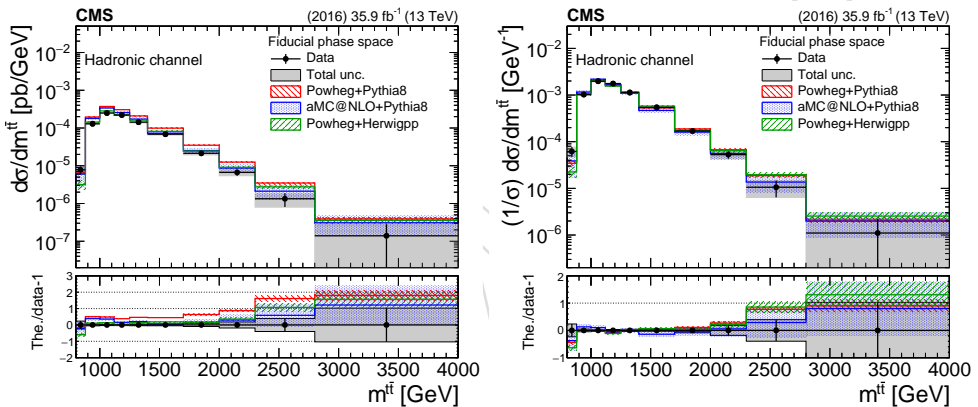


Figure 36: Fiducial differential cross section, absolute (left) and normalized (right), as a function of  $m_{t\bar{t}}$ . The bottom panel shows the ratio (theory - data)/data.

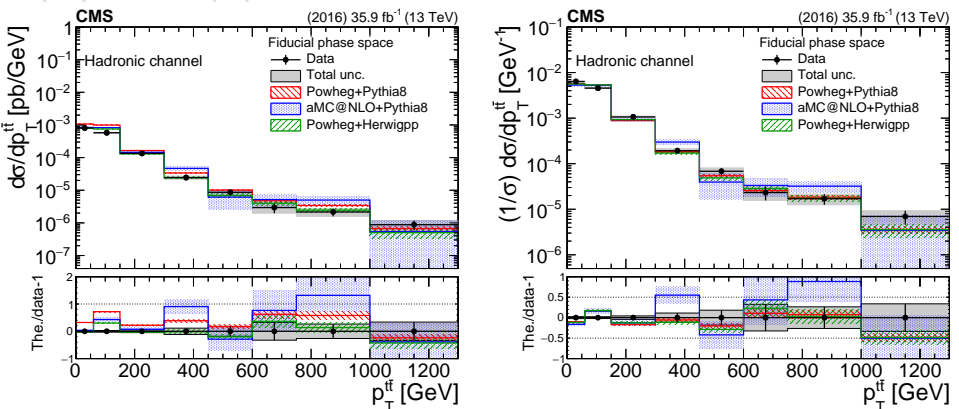


Figure 37: Fiducial differential cross section, absolute (left) and normalized (right), as a function of  $p_{t\bar{t}}$ . The bottom panel shows the ratio (theory - data)/data.

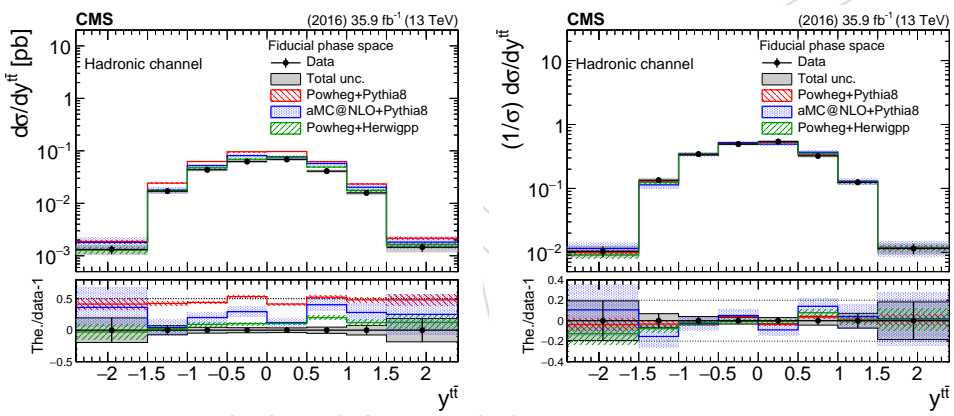


Figure 38: Fiducial differential cross section, absolute (left) and normalized (right), as a function of top  $y_{t\bar{t}}$ . The bottom panel shows the ratio  $(\text{theory} - \text{data})/\text{data}$ .

## 398 10 Unfolded Measurement

399 The fiducial measurement at detector level is also reported unfolded to the parton and particle  
 400 levels. Equation 6 defines the unfolded differential cross section:

$$\frac{d\sigma_i^{\text{unf}}}{dx} = \frac{1}{\mathcal{L} \cdot \Delta x_i} \cdot \frac{1}{f_{2,i}} \cdot \sum_j \left( R_{ij}^{-1} \cdot f_{1,j} \cdot S_j \right), \quad (6)$$

401 where  $\mathcal{L}$  is the total integrated luminosity and  $\Delta x_i$  is the width of the i-th bin of the observable  
 402  $x$ . The quantity  $f_{1,j}$  is the fraction of reconstructed events in the j-th bin that have an equiva-  
 403 lence event at the unfolded level (parton or particle), whereas the quantity  $f_{2,i}$  is the fraction of  
 404 events at the unfolded level that have an equivalent reconstructed event. Figures 39 and 48 be-  
 405 low show the aforementioned fractions at parton and particle level, respectively, as a function  
 406 of all the observables. The quantity  $R_{ij}^{-1}$  is the inverse of the migration matrix between the i-th  
 407 and j-th bins. Due to the finite resolution of the detector, the migration matrix is non-diagonal  
 408 and thus the application of an unfolding procedure is necessary. The binning of the various  
 409 observables has been chosen such that the purity (fraction of reconstructed events that the true  
 410 value of the observable lies in the same bin) and the stability (fraction of true events that the re-  
 411 constructed observable lies in the same bin) are well above 50% (Figures 40 and 49). This choice  
 412 results in highly diagonal migration matrices, shown in Figs. 41 and 50. In order to avoid the  
 413 biases introduced by the various unfolding methods with some type of regularization, we have  
 414 used simple migration matrix inversion, as written in Eq. 6 at a price of a moderate increase of  
 415 the statistical uncertainty (see details in Appendix D).

### 416 10.1 Parton Level

417 The results of the unfolded measurement at parton level are shown in Figs. 42–46. The compar-  
 418 ison with the theory predictions follows the trends observed in the fiducial measurement. That  
 419 is, there is an 20–40% lower inclusive cross section, while the shapes of the differential distri-  
 420 butions are reasonably reproduced by all models. A hint of a deviation at very high values of  
 421  $m^{t\bar{t}}$  is observed but the measurement is not very precise at this part of the phase space.

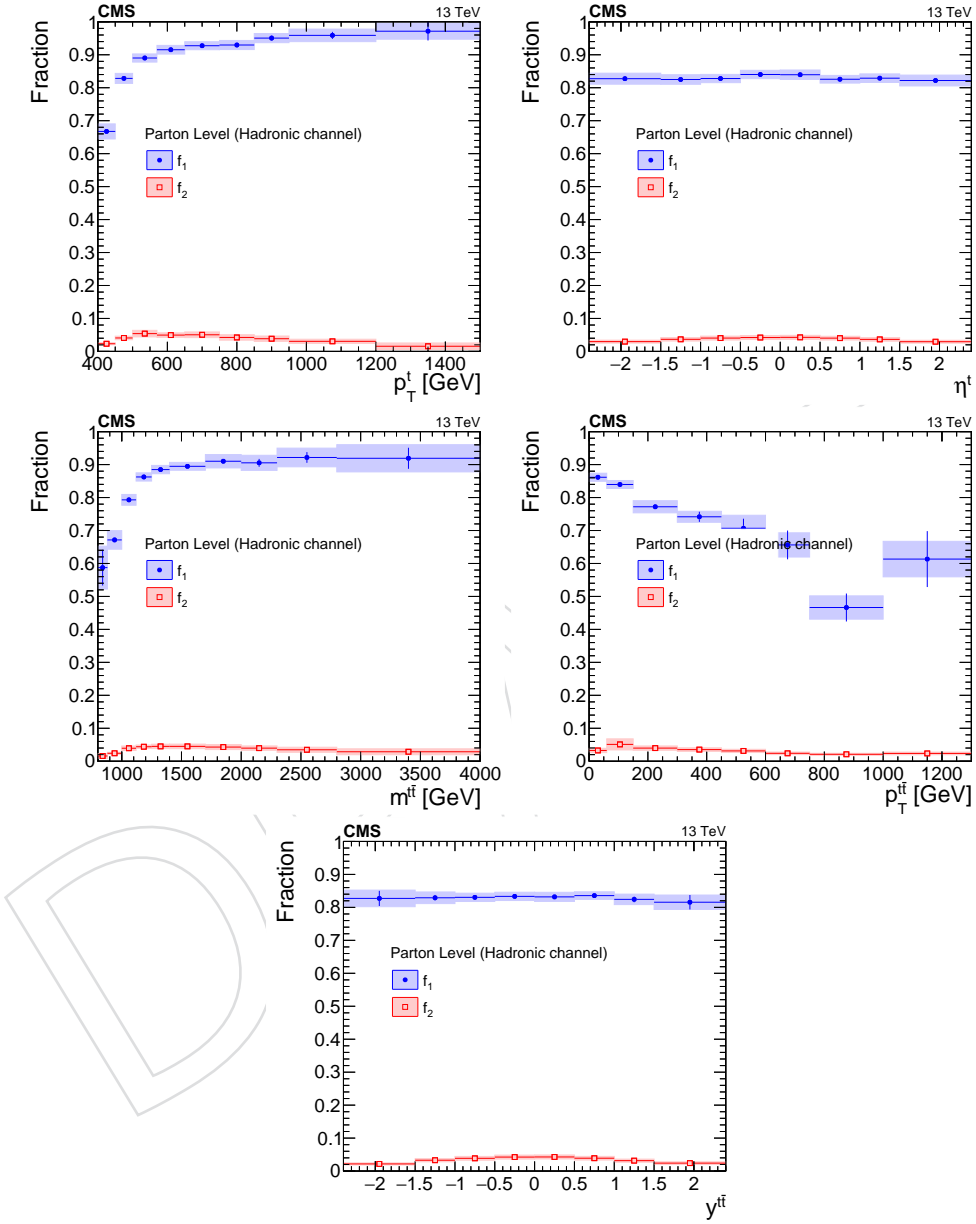


Figure 39: Simulated fractions  $f_{1,2}$  for the parton-level selection as a function of the various observables.

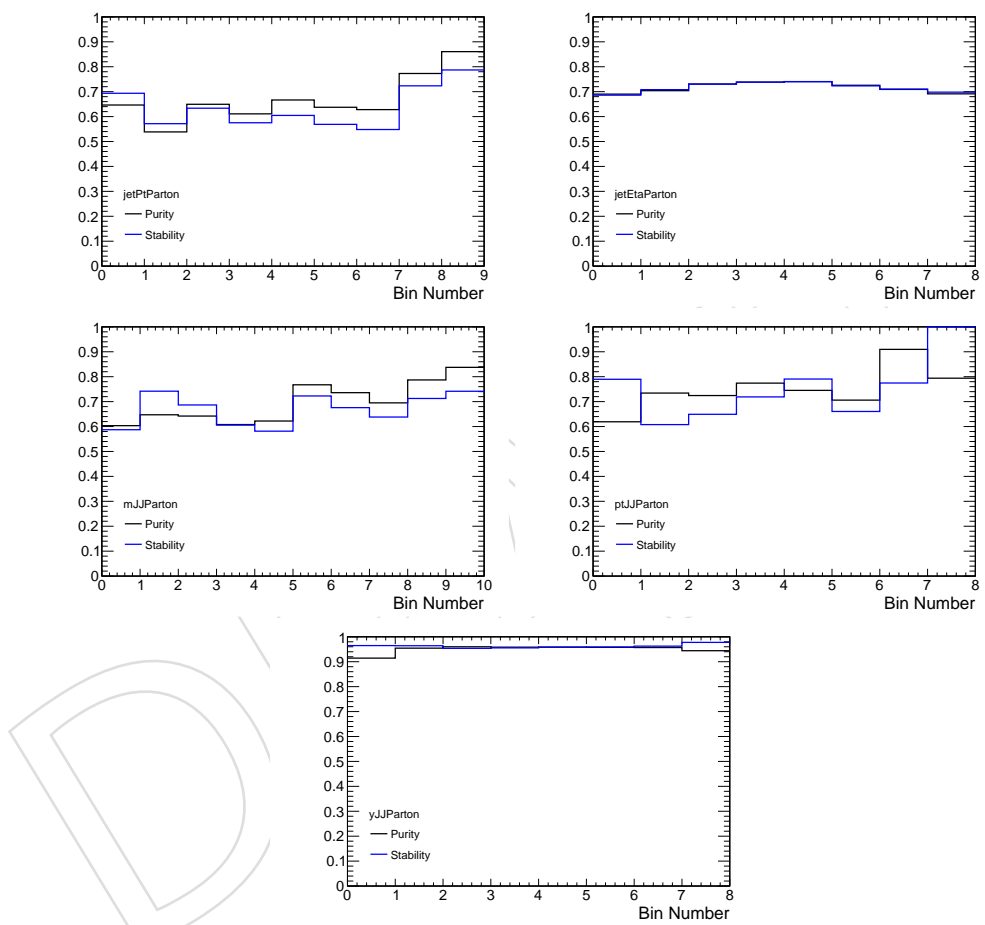


Figure 40: Simulated purity and stability of each bin at parton level.

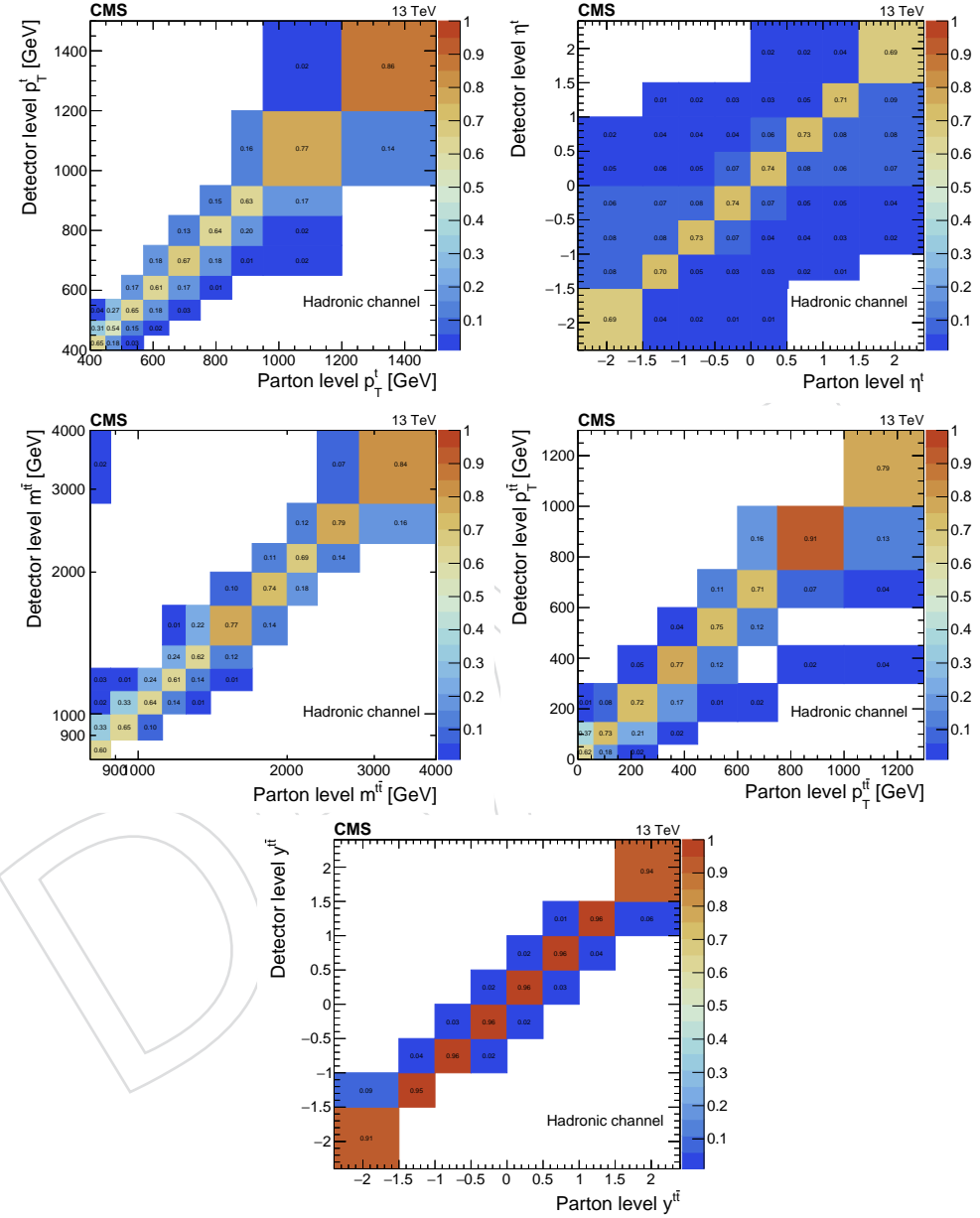


Figure 41: Simulated migration matrices at parton level. Each column is normalized to unity.

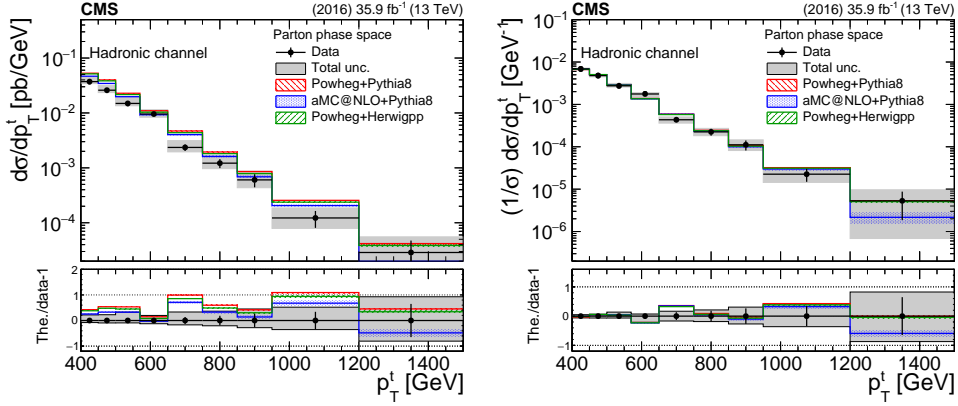


Figure 42: Differential cross section unfolded to parton level, absolute (left) and normalized (right), as a function of top  $p_T$ . The bottom panel shows the ratio (theory - data)/data.

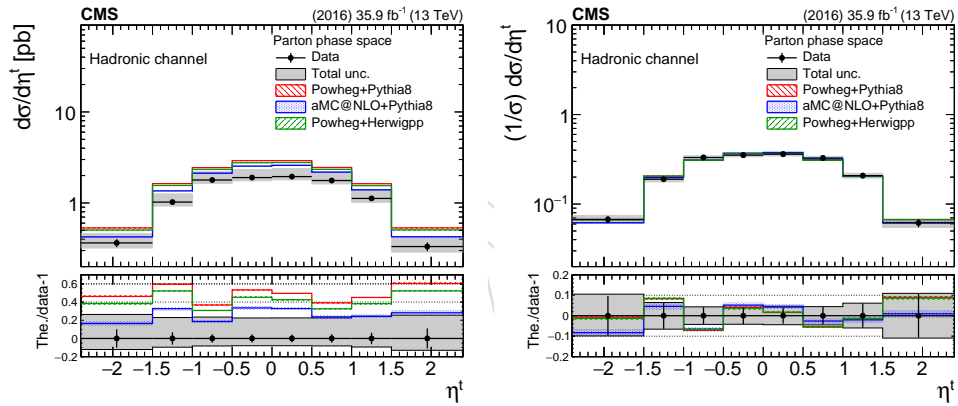


Figure 43: Differential cross section unfolded to parton level, absolute (left) and normalized (right), as a function of top  $\eta$ . The bottom panel shows the ratio (theory - data)/data.

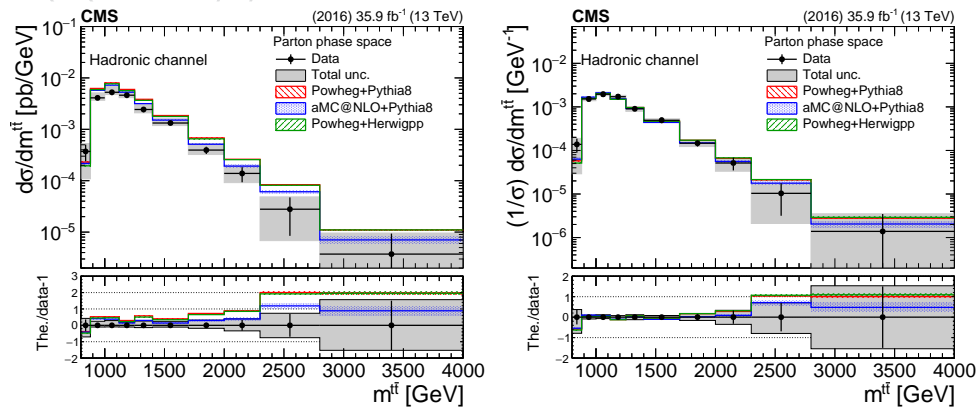


Figure 44: Differential cross section unfolded to parton level, absolute (left) and normalized (right), as a function of  $m_{t\bar{t}}$ . The bottom panel shows the ratio (theory - data)/data.

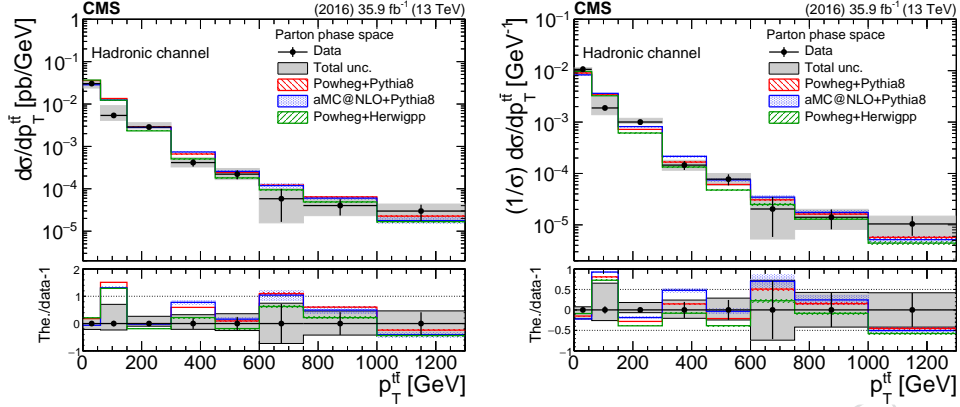


Figure 45: Differential cross section unfolded to parton level, absolute (left) and normalized (right), as a function of  $p_T^{t\bar{t}}$ . The bottom panel shows the ratio (theory - data)/data.

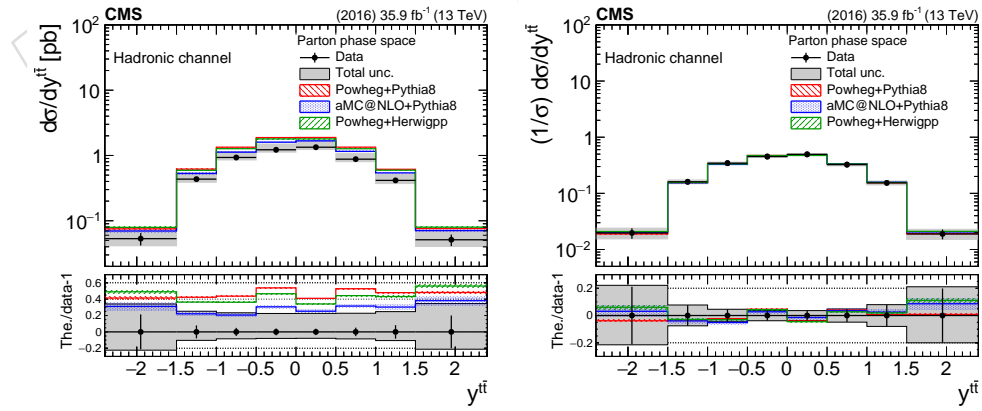


Figure 46: Differential cross section unfolded to parton level, absolute (left) and normalized (right), as a function of  $y^{t\bar{t}}$ . The bottom panel shows the ratio (theory - data)/data.

---

**422 10.2 Particle Level**

423 The results of the unfolded measurement at particle level are shown in Figs. 51- 55. We observe  
 424 that the uncertainties are similar to those of the parton level, while the comparison with the  
 425 theory predictions follows the trends observed in the fiducial measurement. That is, there is  
 426 an 20 – 40% lower inclusive cross section, while the shapes of the differential distributions  
 427 are reasonably reproduced by all models. A hint of a deviation at very high values of  $m^{t\bar{t}}$  is  
 428 observed but the measurement is not very precise at this part of the phase space.

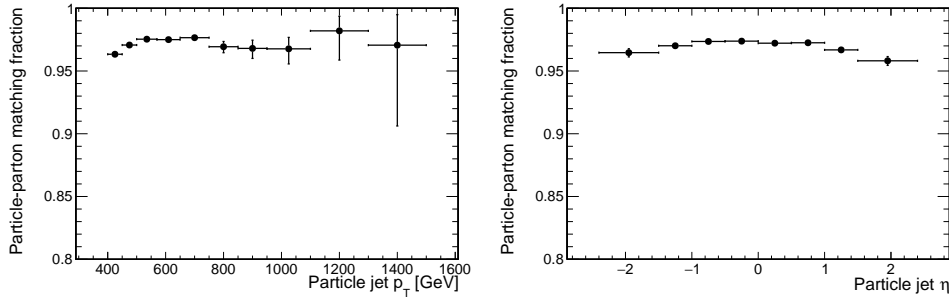


Figure 47: Simulated efficiency of the particle-level top candidates as a function of  $p_T$  and  $\eta$ .

DRAFT

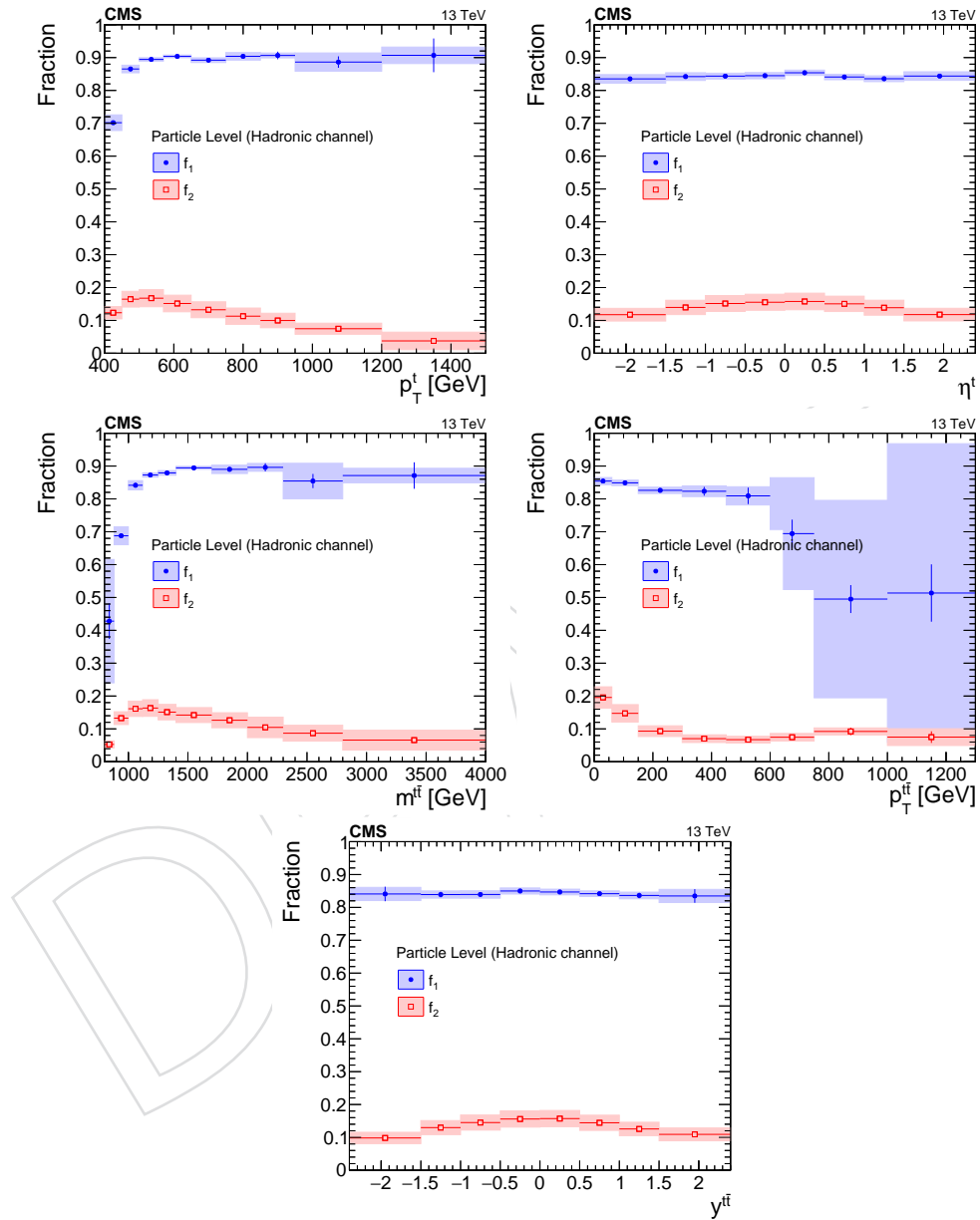


Figure 48: Simulated acceptance and efficiency for the particle-level selection as a function of the various observables.

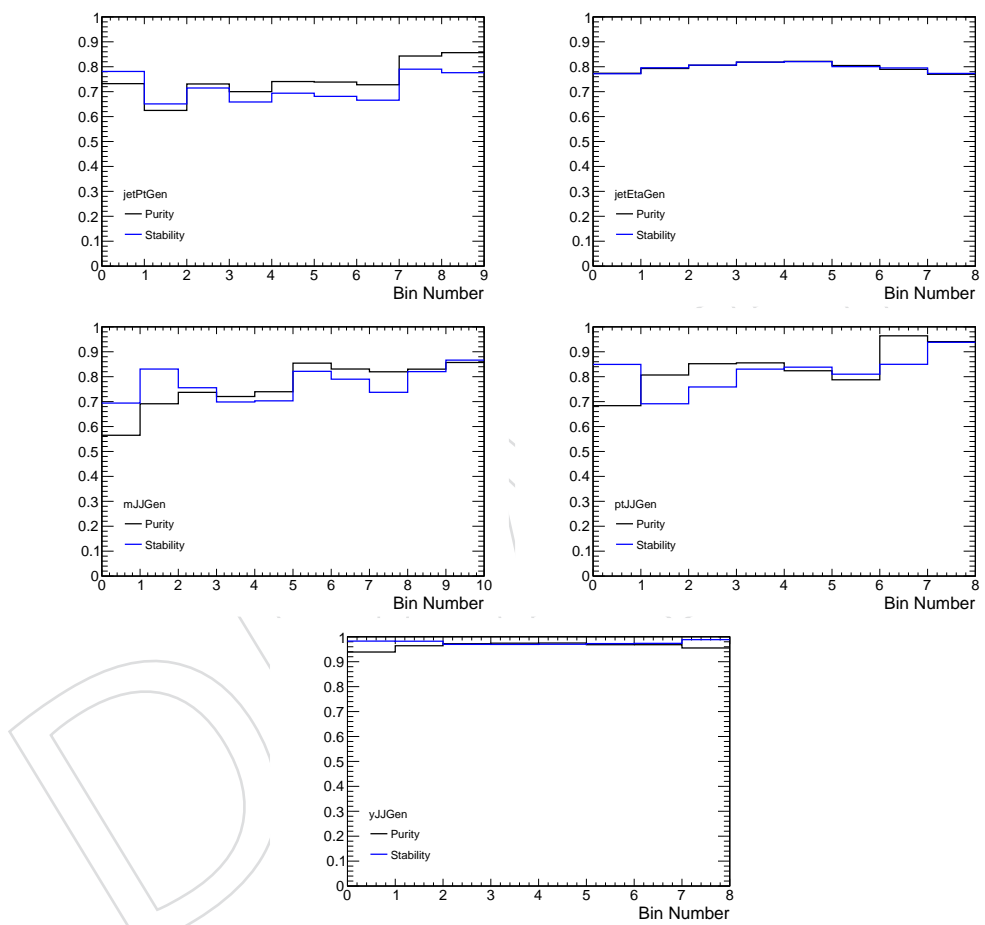


Figure 49: Simulated purity and stability of each bin at particle level.

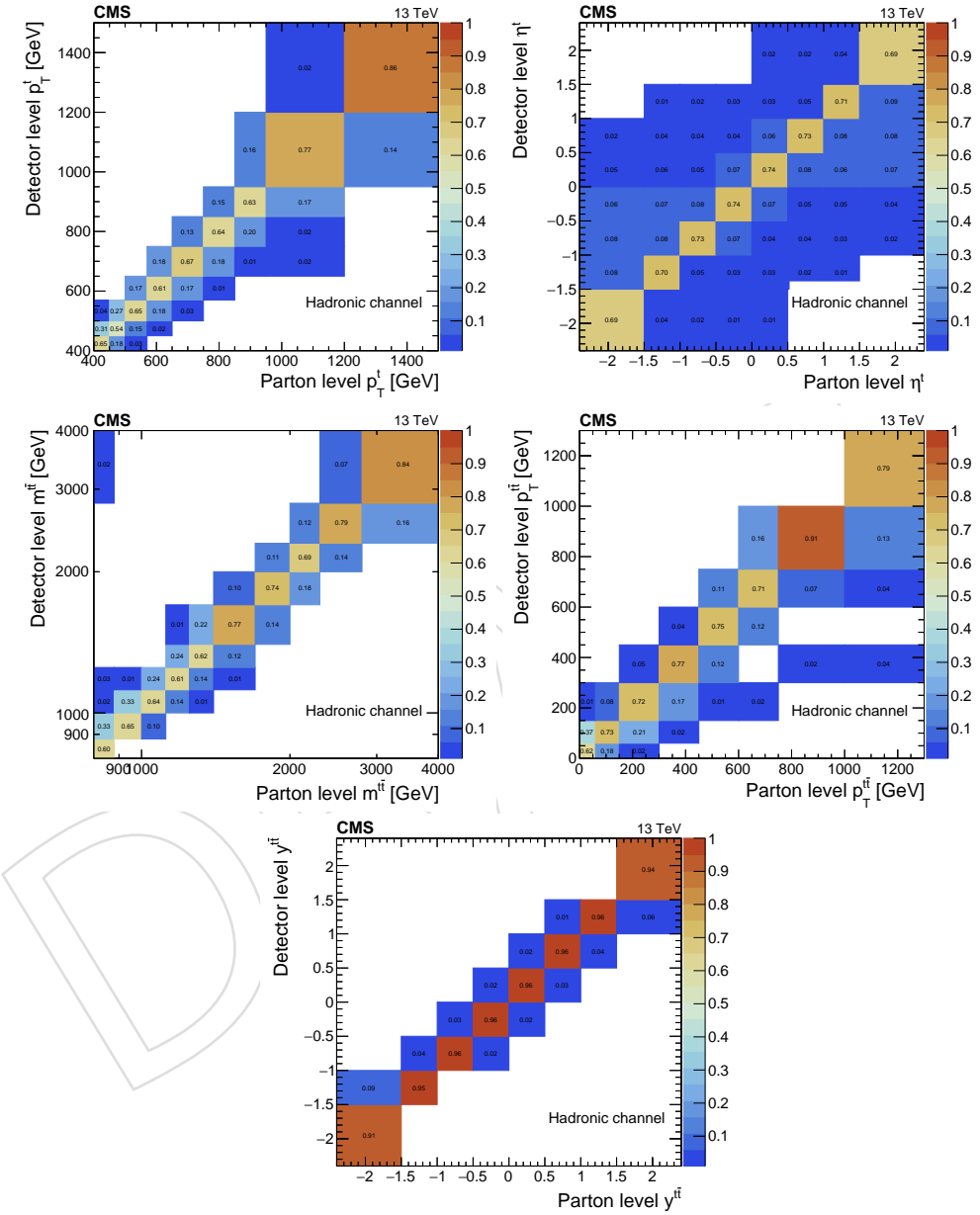


Figure 50: Simulated migration matrices at particle level. Each column is normalized to unity.

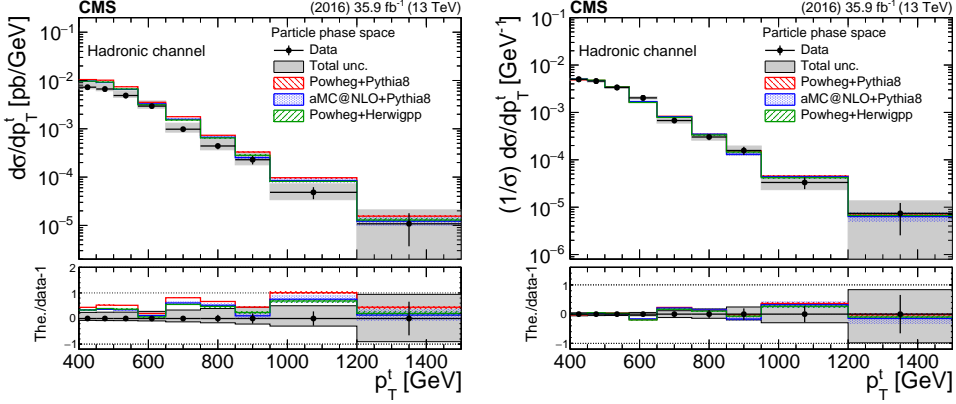


Figure 51: Differential cross section unfolded to particle level, absolute (left) and normalized (right), as a function of top  $p_T$ . The bottom panel shows the ratio (theory - data)/data.

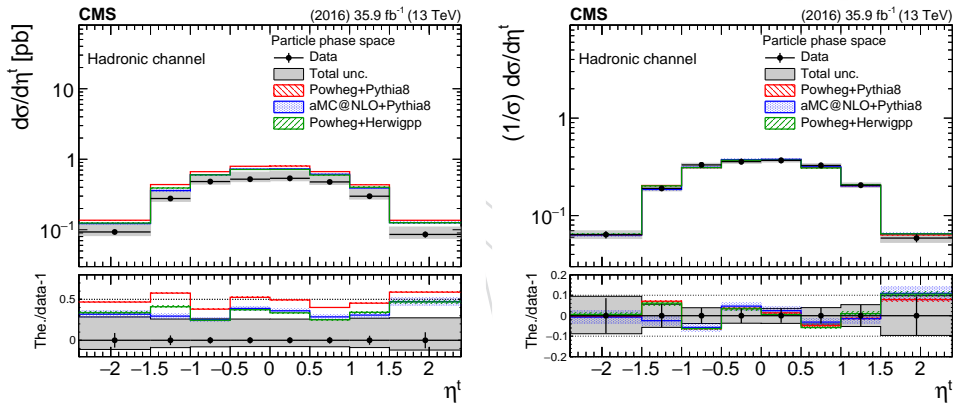


Figure 52: Differential cross section unfolded to particle level, absolute (left) and normalized (right), as a function of top  $p_T$ . The bottom panel shows the ratio (theory - data)/data.

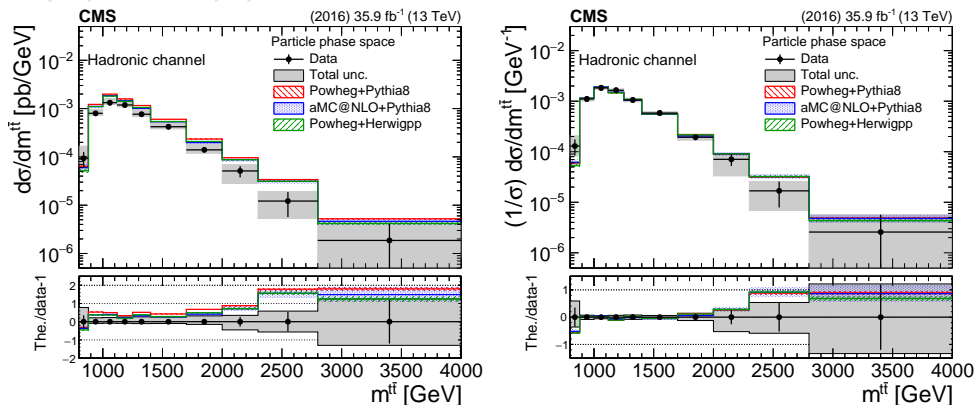


Figure 53: Differential cross section unfolded to particle level, absolute (left) and normalized (right), as a function of  $m_{t\bar{t}}$ . The bottom panel shows the ratio (theory - data)/data.

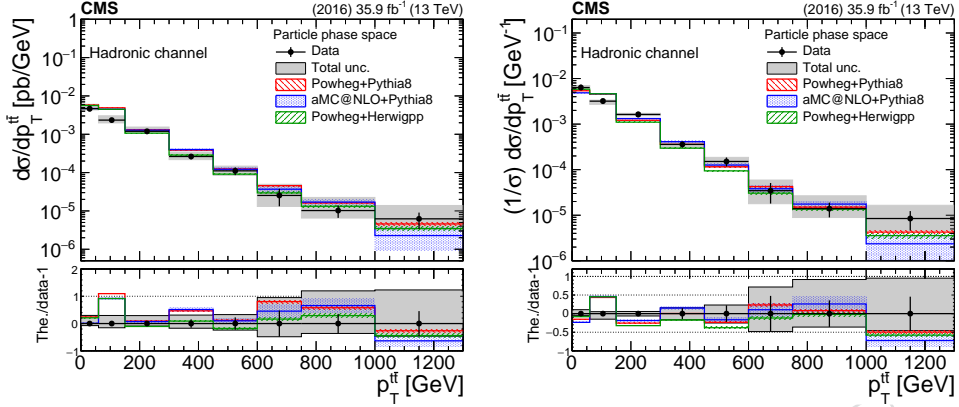


Figure 54: Differential cross section unfolded to particle level, absolute (left) and normalized (right), as a function of  $p_T^{t\bar{t}}$ . The bottom panel shows the ratio (theory - data)/data.

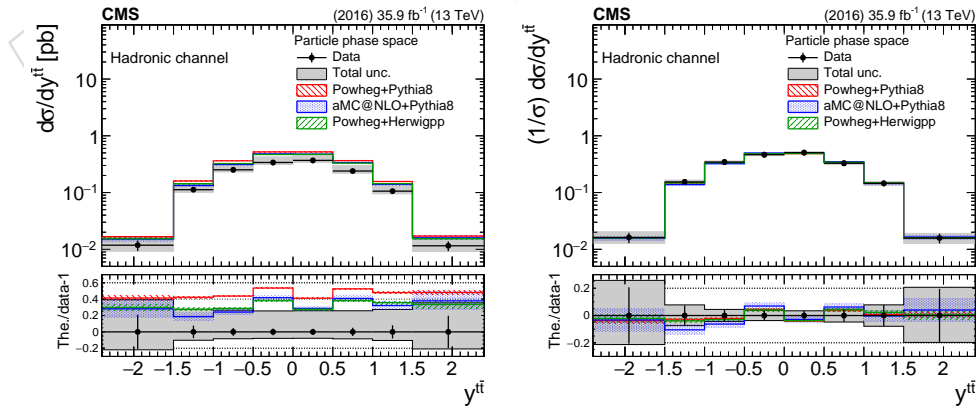


Figure 55: Differential cross section unfolded to particle level, absolute (left) and normalized (right), as a function of  $y^{t\bar{t}}$ . The bottom panel shows the ratio (theory - data)/data.

**429 11 Summary**

430 A measurement of the  $t\bar{t}$  production cross section for high- $p_T$  top quarks at 13 TeV proton-  
431 proton collisions has been presented. The measurement is performed with events where both  
432 top quarks decay hadronically, and where the hadronic decay products cannot be resolved but  
433 are instead clustered in a single large- $R$  jet with  $p_T > 400$  GeV. The hadronic final state thus  
434 contains two large- $R$  jets. The cross section is reported differentially as a function of (inclusive)  
435 top  $p_T$  and  $\eta$ , and as a function of the invariant mass,  $p_T$ , and rapidity of the  $t\bar{t}$  system, un-  
436 folded to the parton and particle levels, absolute and normalized. The results are compared  
437 to theoretical predictions from the POWHEG matrix-element generator, interfaced with PYTHIA  
438 8 or HERWIG ++ for the underlying event and parton shower, and from the MC@NLO matrix-  
439 element generator, interfaced with PYTHIA 8. All the models overpredict significantly the ab-  
440 solute cross section in the phase space of the measurement (up to 40%), while they are able  
441 to describe consistently the differential shapes in all the variables. The most notable discrep-  
442 ency can be seen in the invariant mass of the  $t\bar{t}$  system, where the theoretical models predict  
443 higher cross section at high mass values. However, in order to estimate the significance of the  
444 discrepancy, more data are needed.

DRAFT

## 445 References

- [1] ATLAS Collaboration, "Measurements of top-quark pair differential cross-sections in the lepton+jets channel in  $pp$  collisions at  $\sqrt{s} = 13$  TeV using the ATLAS detector", *JHEP* **11** (2017) 191, doi:10.1007/JHEP11(2017)191, arXiv:1708.00727.
- [2] ATLAS Collaboration, "Measurements of top-quark pair differential cross-sections in the  $e\mu$  channel in  $pp$  collisions at  $\sqrt{s} = 13$  TeV using the ATLAS detector", *Eur. Phys. J.* **C77** (2017), no. 5, 292, doi:10.1140/epjc/s10052-017-4821-x, arXiv:1612.05220.
- [3] ATLAS Collaboration, "Measurement of lepton differential distributions and the top quark mass in  $t\bar{t}$  production in  $pp$  collisions at  $\sqrt{s} = 8$  TeV with the ATLAS detector", *Eur. Phys. J.* **C77** (2017), no. 11, 804, doi:10.1140/epjc/s10052-017-5349-9, arXiv:1709.09407.
- [4] ATLAS Collaboration, "Measurement of top quark pair differential cross-sections in the dilepton channel in  $pp$  collisions at  $\sqrt{s} = 7$  and 8 TeV with ATLAS", *Phys. Rev.* **D94** (2016), no. 9, 092003, doi:10.1103/PhysRevD.94.092003, arXiv:1607.07281.
- [5] ATLAS Collaboration, "Differential top-antitop cross-section measurements as a function of observables constructed from final-state particles using  $pp$  collisions at  $\sqrt{s} = 7$  TeV in the ATLAS detector", *JHEP* **06** (2015) 100, doi:10.1007/JHEP06(2015)100, arXiv:1502.05923.
- [6] ATLAS Collaboration, "Measurements of top quark pair relative differential cross-sections with ATLAS in  $pp$  collisions at  $\sqrt{s} = 7$  TeV", *Eur. Phys. J.* **C73** (2013), no. 1, 2261, doi:10.1140/epjc/s10052-012-2261-1, arXiv:1207.5644.
- [7] CMS Collaboration, "Measurement of normalized differential  $t\bar{t}$  cross sections in the dilepton channel from  $pp$  collisions at  $\sqrt{s} = 13$  TeV", *JHEP* **04** (2018) 060, doi:10.1007/JHEP04(2018)060, arXiv:1708.07638.
- [8] CMS Collaboration, "Measurements of normalised multi-differential cross sections for top quark pair production in  $pp$  collisions at  $\sqrt{s} = 13$  TeV and simultaneous determination of the strong coupling strength, top quark pole mass and parton distribution functions", Technical Report CMS-PAS-TOP-18-004, CERN, Geneva, 2018.
- [9] CMS Collaboration, "Measurements of  $t\bar{t}$  differential cross sections in proton-proton collisions at  $\sqrt{s} = 13$  TeV using events containing two leptons", *Submitted to: JHEP* (2018) arXiv:1811.06625.
- [10] CMS Collaboration, "Measurement of differential cross sections for top quark pair production using the lepton+jets final state in proton-proton collisions at 13 TeV", *Phys. Rev.* **D95** (2017), no. 9, 092001, doi:10.1103/PhysRevD.95.092001, arXiv:1610.04191.
- [11] CMS Collaboration, "Measurements of differential cross sections of top quark pair production as a function of kinematic event variables in proton-proton collisions at  $\sqrt{s} = 13$  TeV", *JHEP* **06** (2018) 002, doi:10.1007/JHEP06(2018)002, arXiv:1803.03991.
- [12] CMS Collaboration, "Measurement of double-differential cross sections for top quark pair production in  $pp$  collisions at  $\sqrt{s} = 8$  TeV and impact on parton distribution

- 487       functions”, *Eur. Phys. J.* **C77** (2017), no. 7, 459,  
 488       doi:[10.1140/epjc/s10052-017-4984-5](https://doi.org/10.1140/epjc/s10052-017-4984-5), arXiv:[1703.01630](https://arxiv.org/abs/1703.01630).
- 489 [13] CMS Collaboration, “Measurement of the differential cross section for top quark pair  
 490 production in pp collisions at  $\sqrt{s} = 8 \text{ TeV}$ ”, *Eur. Phys. J.* **C75** (2015), no. 11, 542,  
 491 doi:[10.1140/epjc/s10052-015-3709-x](https://doi.org/10.1140/epjc/s10052-015-3709-x), arXiv:[1505.04480](https://arxiv.org/abs/1505.04480).
- 492 [14] CMS Collaboration, “Measurement of the differential cross sections for top quark pair  
 493 production as a function of kinematic event variables in pp collisions at  $\sqrt{s}=7$  and 8  
 494 TeV”, *Phys. Rev.* **D94** (2016), no. 5, 052006, doi:[10.1103/PhysRevD.94.052006](https://doi.org/10.1103/PhysRevD.94.052006),  
 495 arXiv:[1607.00837](https://arxiv.org/abs/1607.00837).
- 496 [15] CMS Collaboration, “Measurement of differential top-quark pair production cross  
 497 sections in pp colisions at  $\sqrt{s} = 7 \text{ TeV}$ ”, *Eur. Phys. J.* **C73** (2013), no. 3, 2339,  
 498 doi:[10.1140/epjc/s10052-013-2339-4](https://doi.org/10.1140/epjc/s10052-013-2339-4), arXiv:[1211.2220](https://arxiv.org/abs/1211.2220).
- 499 [16] ATLAS Collaboration, “Measurements of  $t\bar{t}$  differential cross-sections of highly boosted  
 500 top quarks decaying to all-hadronic final states in pp collisions at  $\sqrt{s} = 13 \text{ TeV}$  using the  
 501 ATLAS detector”, *Phys. Rev.* **D98** (2018), no. 1, 012003,  
 502 doi:[10.1103/PhysRevD.98.012003](https://doi.org/10.1103/PhysRevD.98.012003), arXiv:[1801.02052](https://arxiv.org/abs/1801.02052).
- 503 [17] ATLAS Collaboration, “Measurement of the differential cross-section of highly boosted  
 504 top quarks as a function of their transverse momentum in  $\sqrt{s} = 8 \text{ TeV}$  proton-proton  
 505 collisions using the ATLAS detector”, *Phys. Rev.* **D93** (2016), no. 3, 032009,  
 506 doi:[10.1103/PhysRevD.93.032009](https://doi.org/10.1103/PhysRevD.93.032009), arXiv:[1510.03818](https://arxiv.org/abs/1510.03818).
- 507 [18] CMS Collaboration Collaboration, “Measurement of the  $t\bar{t}$  production cross section at 13  
 508 TeV in the all-jets final state”, Technical Report CMS-PAS-TOP-16-013, CERN, Geneva,  
 509 2016.
- 510 [19] CMS Collaboration, “Measurement of the integrated and differential  $t\bar{t}$  production cross  
 511 sections for high- $p_t$  top quarks in pp collisions at  $\sqrt{s} = 8 \text{ TeV}$ ”, *Phys. Rev.* **D94** (2016),  
 512 no. 7, 072002, doi:[10.1103/PhysRevD.94.072002](https://doi.org/10.1103/PhysRevD.94.072002), arXiv:[1605.00116](https://arxiv.org/abs/1605.00116).
- 513 [20] CMS Collaboration Collaboration, “Measurement of the differential  $t\bar{t}$  cross section with  
 514 high- $p_T$  top-quark jets in the all-hadronic channel at  $\sqrt{s} = 8 \text{ TeV}$ ”, Technical Report  
 515 CMS-PAS-TOP-16-018, CERN, Geneva, 2017.
- 516 [21] P. Nason, “A new method for combining NLO QCD with shower Monte Carlo  
 517 algorithms”, *JHEP* **11** (2004) 040, doi:[10.1088/1126-6708/2004/11/040](https://doi.org/10.1088/1126-6708/2004/11/040),  
 518 arXiv:[hep-ph/0409146](https://arxiv.org/abs/hep-ph/0409146).
- 519 [22] S. Frixione, P. Nason, and G. Ridolfi, “A Positive-weight next-to-leading-order Monte  
 520 Carlo for heavy flavour hadroproduction”, *JHEP* **09** (2007) 126,  
 521 doi:[10.1088/1126-6708/2007/09/126](https://doi.org/10.1088/1126-6708/2007/09/126), arXiv:[0707.3088](https://arxiv.org/abs/0707.3088).
- 522 [23] S. Frixione, P. Nason, and C. Oleari, “Matching NLO QCD computations with parton  
 523 shower simulations: the POWHEG method”, *JHEP* **11** (2007) 070,  
 524 doi:[10.1088/1126-6708/2007/11/070](https://doi.org/10.1088/1126-6708/2007/11/070), arXiv:[0709.2092](https://arxiv.org/abs/0709.2092).
- 525 [24] S. Alioli, P. Nason, C. Oleari, and E. Re, “A general framework for implementing NLO  
 526 calculations in shower Monte Carlo programs: the POWHEG BOX”, *JHEP* **06** (2010) 043,  
 527 doi:[10.1007/JHEP06\(2010\)043](https://doi.org/10.1007/JHEP06(2010)043), arXiv:[1002.2581](https://arxiv.org/abs/1002.2581).

- 528 [25] S. Alioli, S. O. Moch, and P. Uwer, “Hadronic top-quark pair-production with one jet and  
529 parton showering”, *JHEP* **01** (2012) 137, doi:10.1007/JHEP01(2012)137,  
530 arXiv:1110.5251.
- 531 [26] S. Alioli, P. Nason, C. Oleari, and E. Re, “NLO single-top production matched with  
532 shower in POWHEG:  $s$ - and  $t$ -channel contributions”, *JHEP* **09** (2009) 111,  
533 doi:10.1088/1126-6708/2009/09/111, arXiv:0907.4076. [Erratum:  
534 doi:10.1007/JHEP02(2010)011].
- 535 [27] J. Alwall et al., “The automated computation of tree-level and next-to-leading order  
536 differential cross sections, and their matching to parton shower simulations”, *JHEP* **07**  
537 (2014) 079, doi:10.1007/JHEP07(2014)079, arXiv:1405.0301.
- 538 [28] J. Alwall et al., “Comparative study of various algorithms for the merging of parton  
539 showers and matrix elements in hadronic collisions”, *Eur. Phys. J.* **C53** (2008) 473–500,  
540 doi:10.1140/epjc/s10052-007-0490-5, arXiv:0706.2569.
- 541 [29] T. Sjöstrand, S. Mrenna, and P. Z. Skands, “PYTHIA 6.4 physics and manual”, *JHEP* **05**  
542 (2006) 026, doi:10.1088/1126-6708/2006/05/026, arXiv:hep-ph/0603175.
- 543 [30] T. Sjöstrand, S. Mrenna, and P. Z. Skands, “A brief introduction to PYTHIA 8.1”, *Comput.  
544 Phys. Commun.* **178** (2008) 852, doi:10.1016/j.cpc.2008.01.036,  
545 arXiv:0710.3820.
- 546 [31] NNPDF Collaboration, “Parton distributions for the LHC Run II”, *JHEP* **04** (2015) 040,  
547 doi:10.1007/JHEP04(2015)040, arXiv:1410.8849.
- 548 [32] CMS Collaboration, “Event generator tunes obtained from underlying event and  
549 multiparton scattering measurements”, *Eur. Phys. J. C* **76** (2015) 155,  
550 doi:10.1140/epjc/s10052-016-3988-x, arXiv:1512.00815.
- 551 [33] CMS Collaboration Collaboration, “Investigations of the impact of the parton shower  
552 tuning in Pythia 8 in the modelling of  $t\bar{t}$  at  $\sqrt{s} = 8$  and 13 TeV”, Technical Report  
553 CMS-PAS-TOP-16-021, CERN, Geneva, 2016.
- 554 [34] GEANT4 Collaboration, “GEANT4—a simulation toolkit”, *Nucl. Instrum. Meth. A* **506**  
555 (2003) 250, doi:10.1016/S0168-9002(03)01368-8.
- 556 [35] M. Czakon and A. Mitov, “Top++: A program for the calculation of the top-pair  
557 cross-section at hadron colliders”, *Comput. Phys. Commun.* **185** (2014) 2930,  
558 doi:10.1016/j.cpc.2014.06.021, arXiv:1112.5675.
- 559 [36] Y. Li and F. Petriello, “Combining QCD and electroweak corrections to dilepton  
560 production in the framework of the FEWZ simulation code”, *Phys. Rev. D* **86** (2012)  
561 094034, doi:10.1103/PhysRevD.86.094034, arXiv:1208.5967.
- 562 [37] N. Kidonakis, “Top Quark Production”, (2014). arXiv:1311.0283.
- 563 [38] M. Bahr et al., “Herwig++ Physics and Manual”, *Eur. Phys. J.* **C58** (2008) 639–707,  
564 doi:10.1140/epjc/s10052-008-0798-9, arXiv:0803.0883.
- 565 [39] S. Gieseke, C. Rohr, and A. Siodmok, “Colour reconnections in Herwig++”, *Eur. Phys. J.*  
566 **C72** (2012) 2225, doi:10.1140/epjc/s10052-012-2225-5, arXiv:1206.0041.

- 567 [40] J. Therhaag, "TMVA Toolkit for multivariate data analysis in ROOT", *PoS ICHEP2010*  
568 (2010) 510, doi:10.22323/1.120.0510.
- 569 [41] CMS Collaboration, "Jet energy scale and resolution in the CMS experiment in pp  
570 collisions at 8 TeV", *JINST* **12** (2017) P02014,  
571 doi:10.1088/1748-0221/12/02/P02014, arXiv:1607.03663.
- 572 [42] CMS Collaboration, "Identification of heavy-flavour jets with the CMS detector in pp  
573 collisions at 13 TeV", *JINST* **13** (2018) P05011,  
574 doi:10.1088/1748-0221/13/05/P05011, arXiv:1712.07158.
- 575 [43] CMS Collaboration Collaboration, "CMS Luminosity Measurements for the 2016 Data  
576 Taking Period", Technical Report CMS-PAS-LUM-17-001, CERN, Geneva, 2017.

DRAFT

## 577 A NN Input Variables

578 In this section we provide additional comparisons between data and simulation for the six  
 579 variables used as inputs for the NN training, in three different categories: 0, 1, or 2 top jet  
 580 candidates with a b tagged subjet, prior any cut on the NN output.

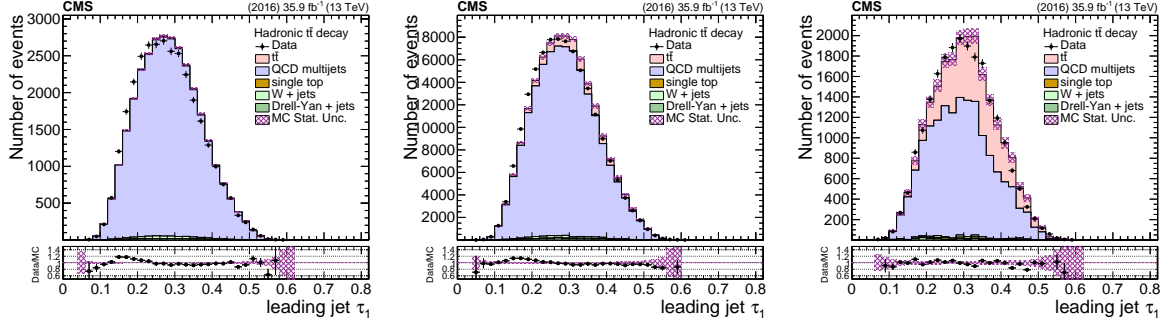


Figure 56: Data vs simulation for the  $\tau_1$  variable of the leading jet after the selection of 0 btagged subjet (left), 1 (middle) and 2 (right).

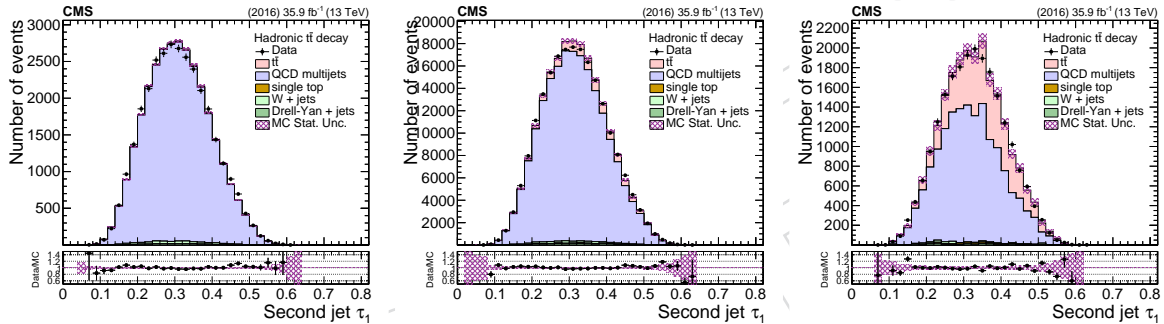


Figure 57: Data vs simulation for the  $\tau_1$  variable of the second jet after the selection of 0 btagged subjet (left), 1 (middle) and 2 (right).

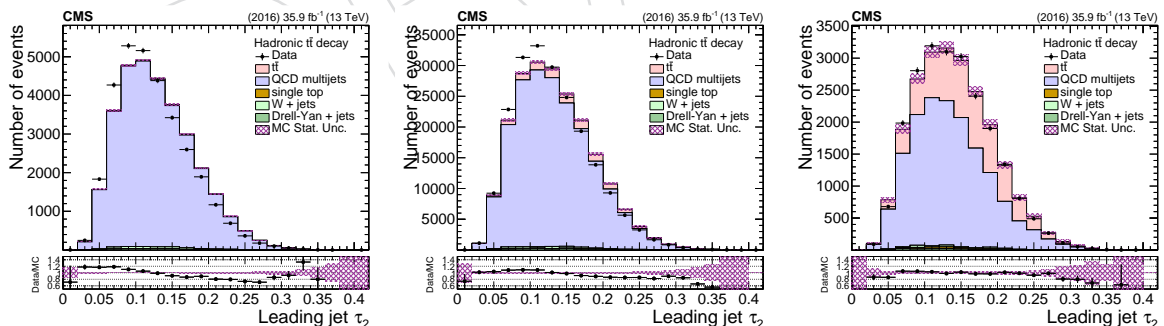


Figure 58: Data vs simulation for the  $\tau_2$  variable of the leading jet after the selection of 0 btagged subjet (left), 1 (middle) and 2 (right).

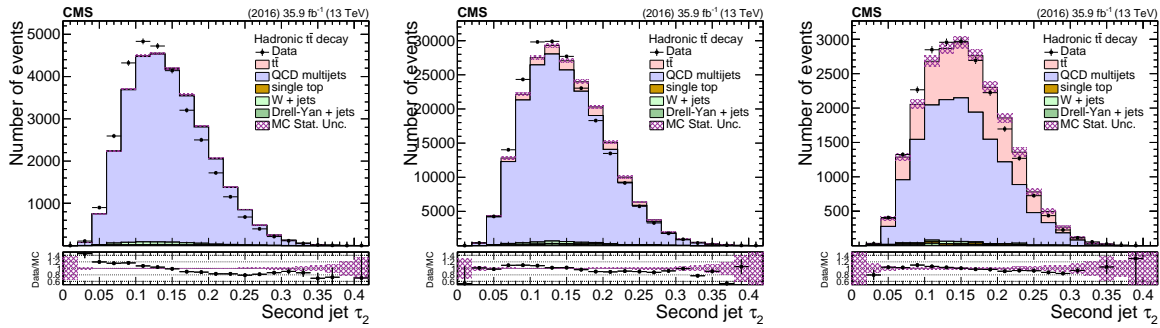


Figure 59: Data vs simulation for the  $\tau_2$  variable of the second jet after the selection of 0 btagged subjet (left), 1 (middle) and 2 (right).

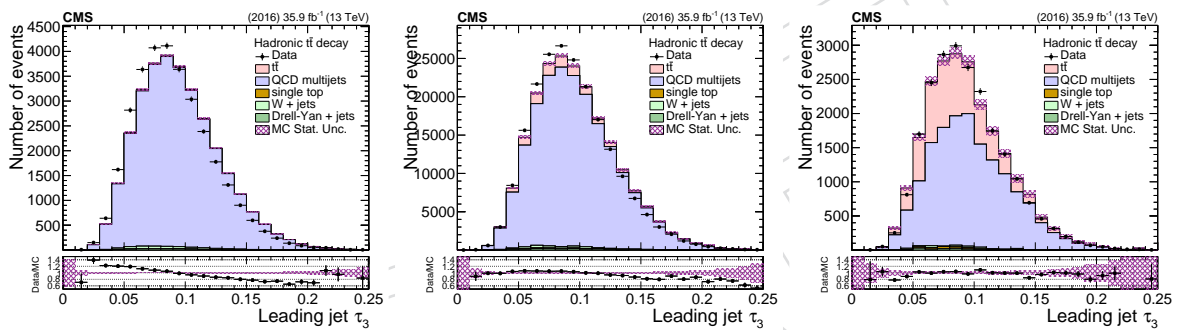


Figure 60: Data vs simulation for the  $\tau_3$  variable of the leading jet after the selection of 0 btagged subjet (left), 1 (middle) and 2 (right).

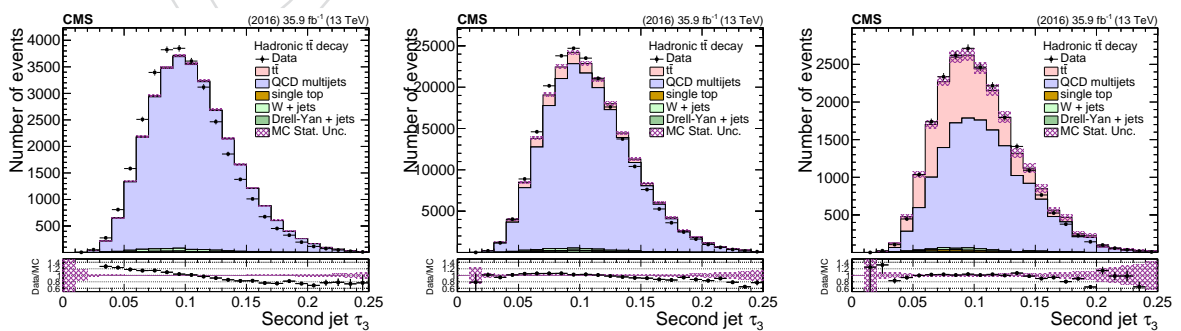


Figure 61: Data vs simulation for the  $\tau_3$  variable of the second jet after the selection of 0 btagged subjet (left), 1 (middle) and 2 (right).

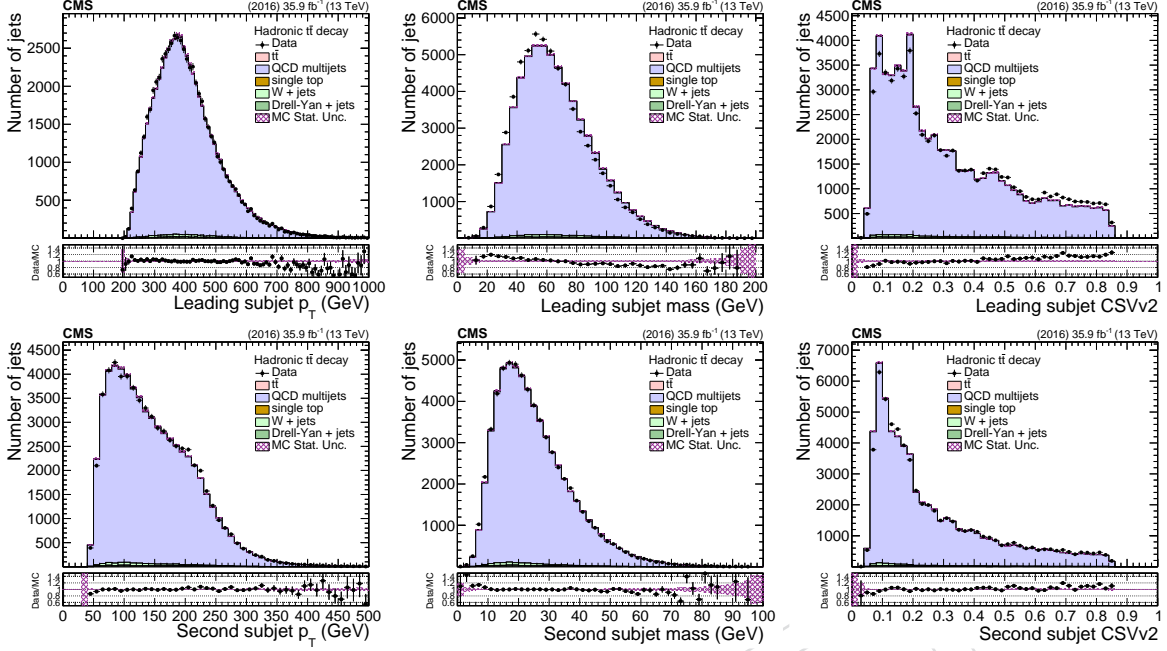


Figure 62: Data vs simulation for the  $p_T$ , mass, and CSVv2 variables for the two subjets of the top candidates after the baseline selection and the requirement of 0 b tagged subjets.

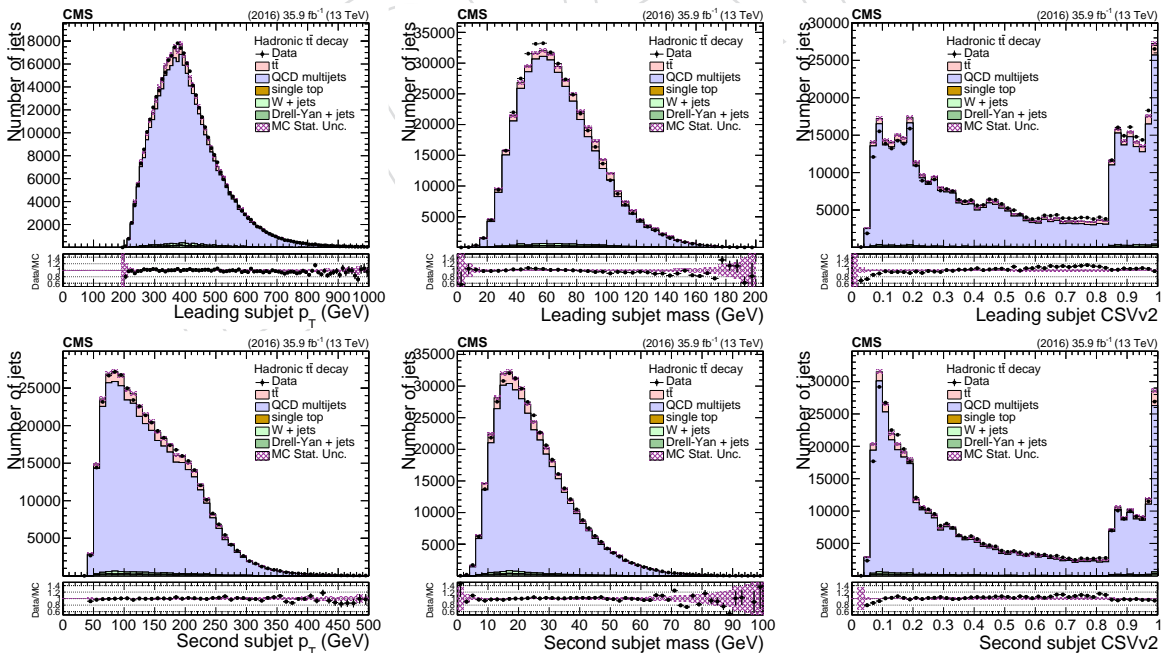


Figure 63: Data vs simulation for the  $p_T$ , mass, and CSVv2 variables for the two subjets of the top candidates after the baseline selection and the requirement of 1 b tagged subjets.

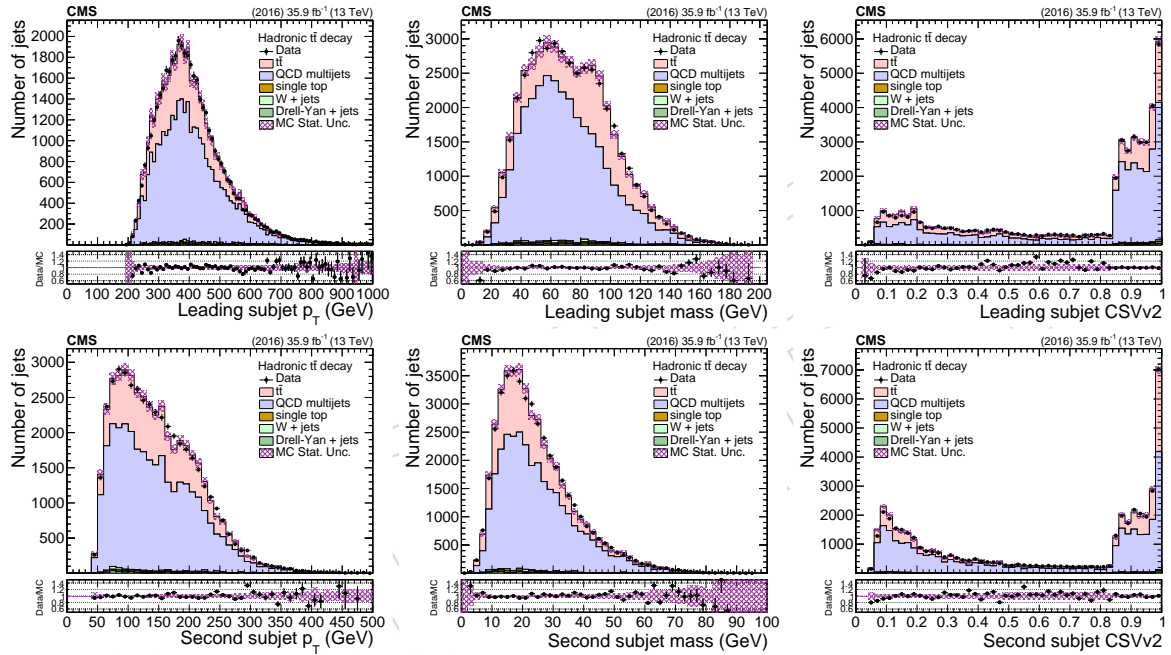


Figure 64: Data vs simulation for the  $p_T$ , mass, and CSVv2 variables for the two subjets of the top candidates after the baseline selection and the requirement of 2 b tagged subjets.

## 581 B Control Distributions

582 In this section we provide additional comparisons between data and simulation. In what fol-  
 583 lows, we show the various observables in the control and signal regions.

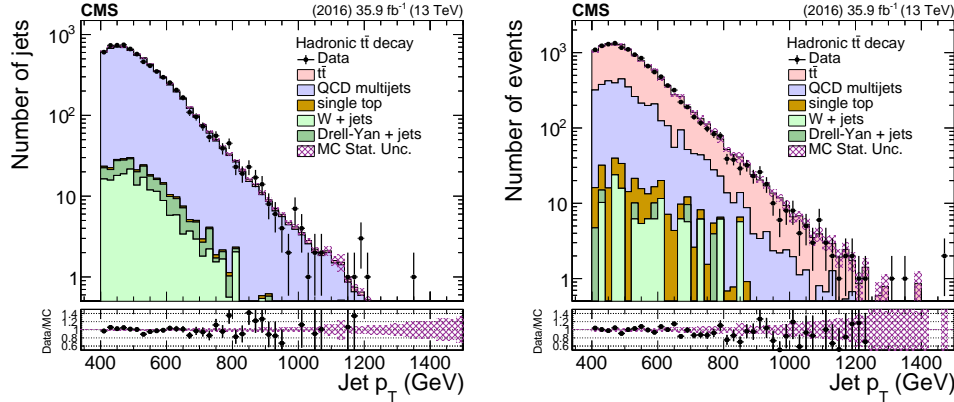


Figure 65: Data vs simulation in the control (left) and signal (right) regions for the  $p_T$  of the two leading jets.

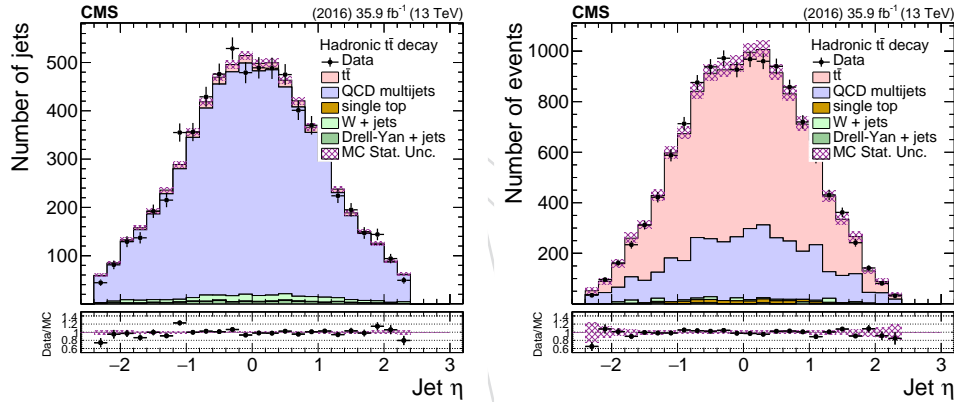


Figure 66: Data vs simulation in the control (left) and signal (right) regions for the  $\eta$  of the two leading jets.

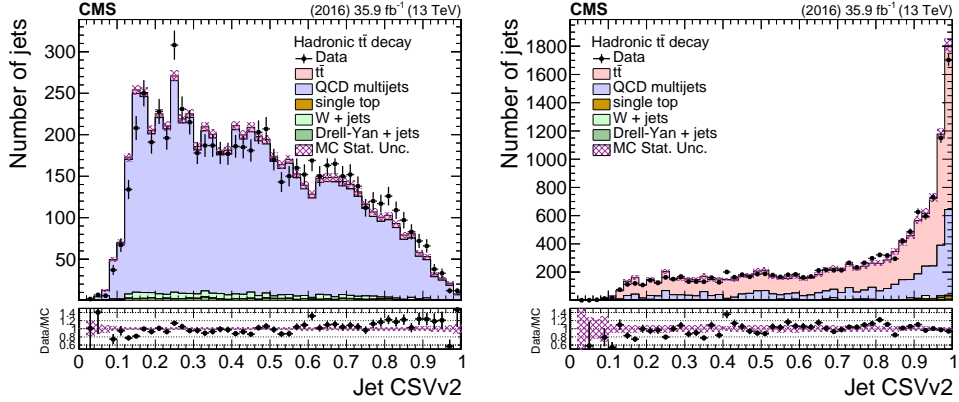


Figure 67: Data vs simulation in the control (left) and signal (right) regions for the CSVv2 of the two leading jets.

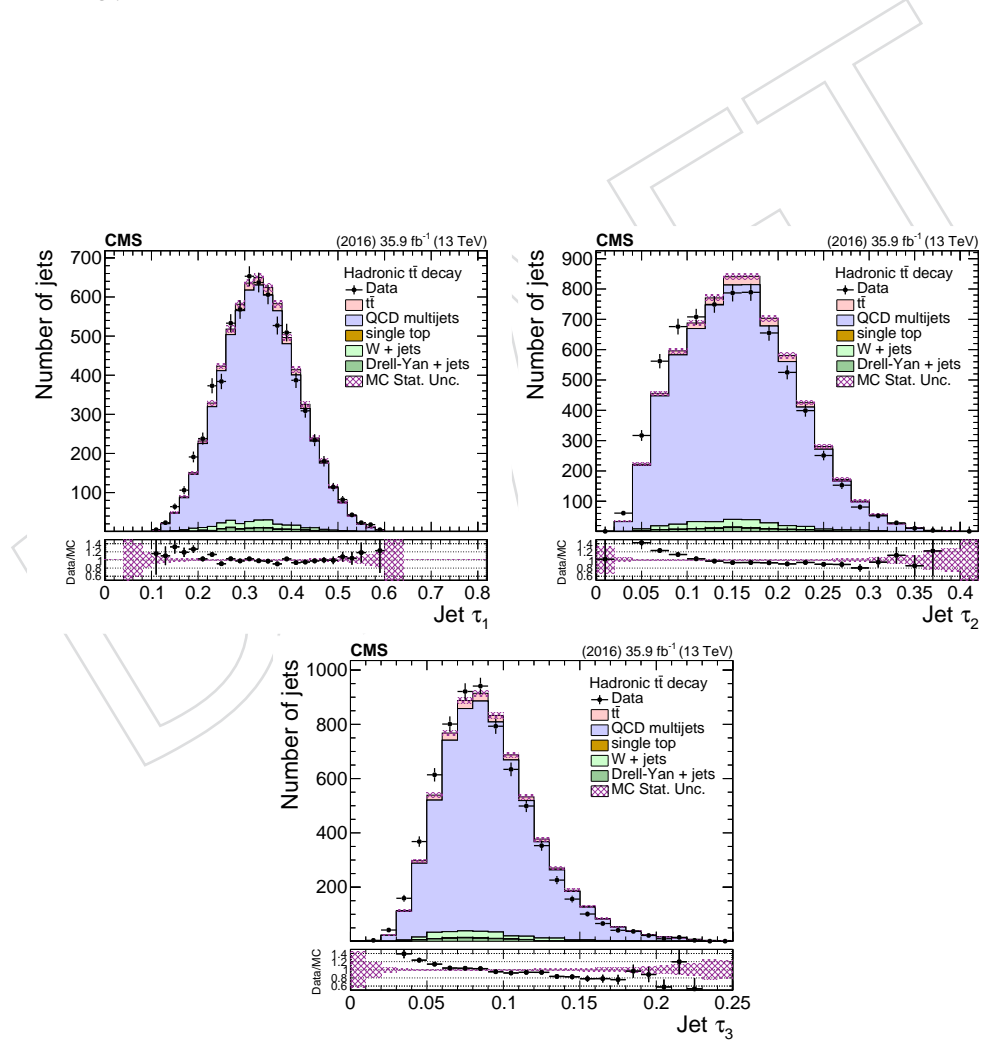


Figure 68: Data vs simulation in the control region for the n-subjettiness of the two leading jets.

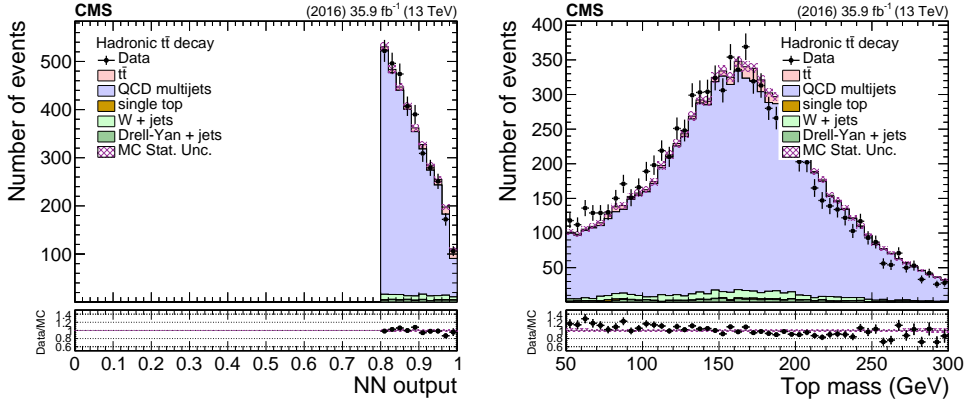


Figure 69: Data vs simulation in the control region for the NN output (left) and the top mass estimator (right).

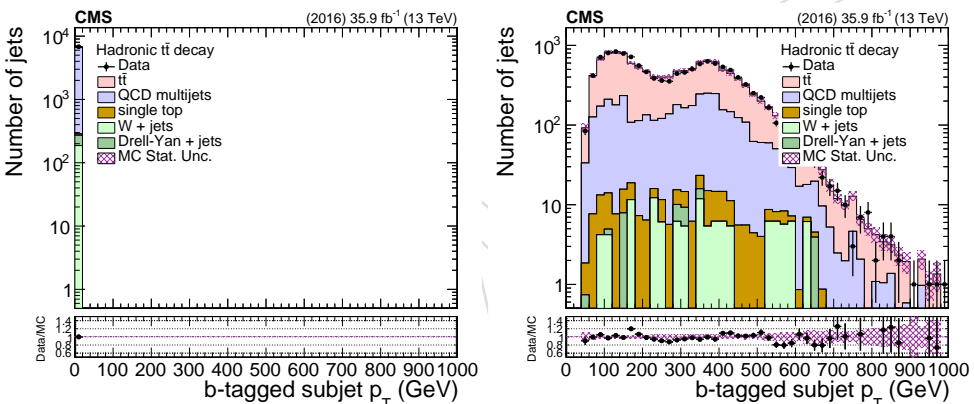


Figure 70: Data vs simulation in the control (left) and signal (right) regions for the  $p_T$  of the b-tagged subjet of the two leading jets.

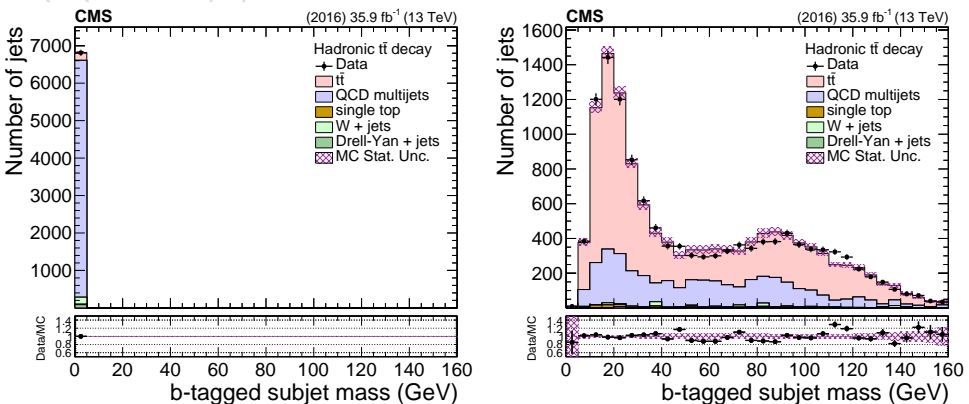


Figure 71: Data vs simulation in the control (left) and signal (right) regions for the mass of the b-tagged subjet of the two leading jets.

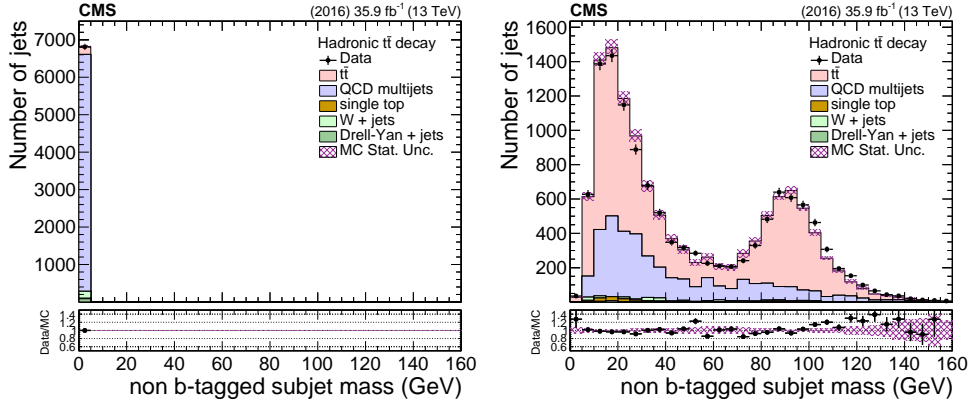


Figure 72: Data vs simulation in the control (left) and signal (right) regions for the mass of the non b-tagged subjet of the two leading jets.

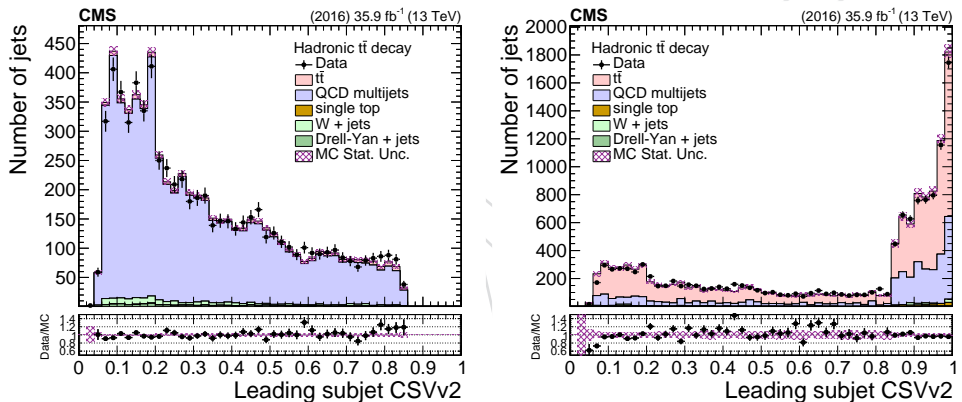


Figure 73: Data vs simulation in the control (left) and signal (right) regions for the CSVv2 of the leading subjet of the two leading jets.

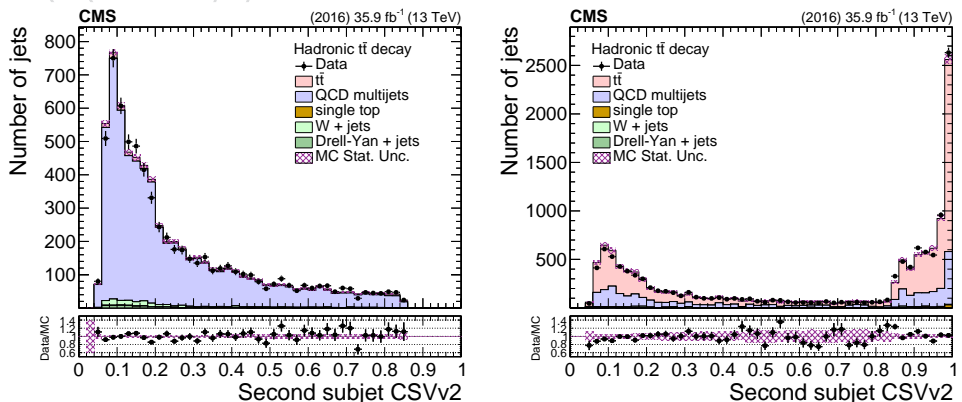


Figure 74: Data vs simulation in the control (left) and signal (right) regions for the CSVv2 of the subleading subjet of the two leading jets.

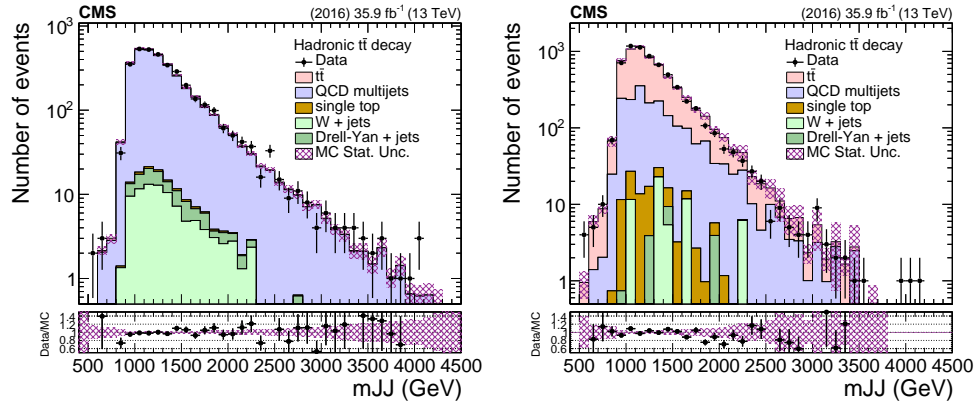


Figure 75: Data vs simulation in the control (left) and signal (right) regions dijet invariant mass.

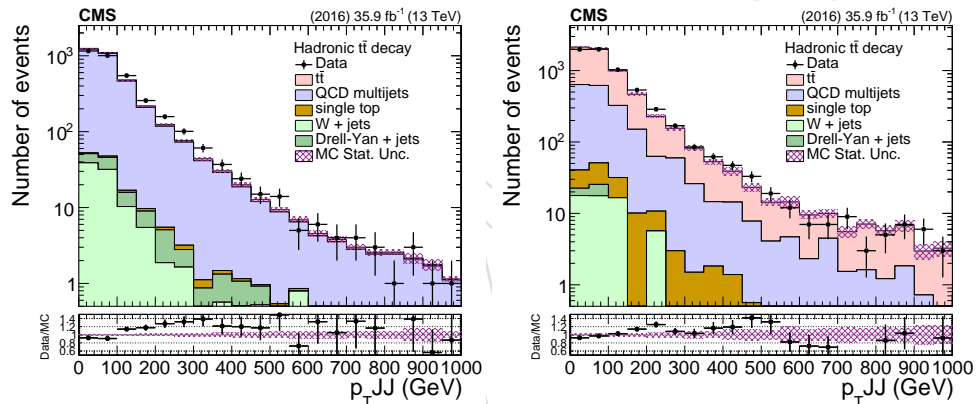


Figure 76: Data vs simulation in the control (left) and signal (right) regions dijet  $p_T$ .

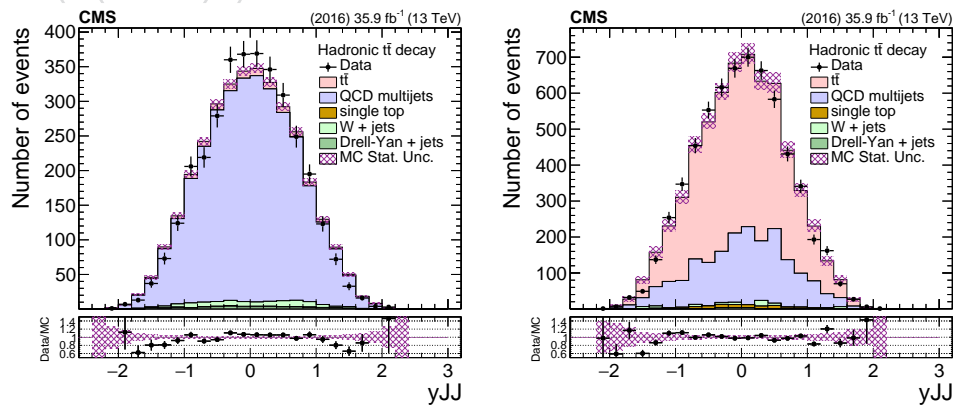


Figure 77: Data vs simulation in the control (left) and signal (right) regions dijet rapidity.

## 584 C Background Sensitivity to Pileup

585 The QCD background shape is taken from the corresponding control region in data, as de-  
 586 scribed in Section 6. Since the data are collected with a prescaled trigger path, the pileup profile  
 587 is different from the one of the signal events (Fig. 1). In order to demonstrate the robustness  
 588 of the QCD prediction between the signal and control regions, we have performed the follow-  
 589 ing test: the data from the control region are split in two subsets according to the number of  
 590 reconstructed vertices ( $< 15$  and  $\geq 15$ ) and we compare in Fig. 78 the distributions of the ob-  
 591 servables used in this analysis. A systematic difference is observed in the softdrop mass of the  
 592 jets, which is expected to be the most sensitive to pileup. This difference is naturally accounted  
 593 for in the extraction of the QCD normalization (Eq. 3) with the unconstrained nuisance param-  
 594 eter  $k_{\text{slope}}$ . In contrast, the shape of the jet and dijet kinematic observables are fully compatible  
 595 within the statistical uncertainty. Therefore, taking also into account that the difference of the  
 596 pileup profile of the two trigger paths is not as extreme as the test conducted here, we conclude  
 597 that no significant bias is introduced by using the QCD shapes from the control region.

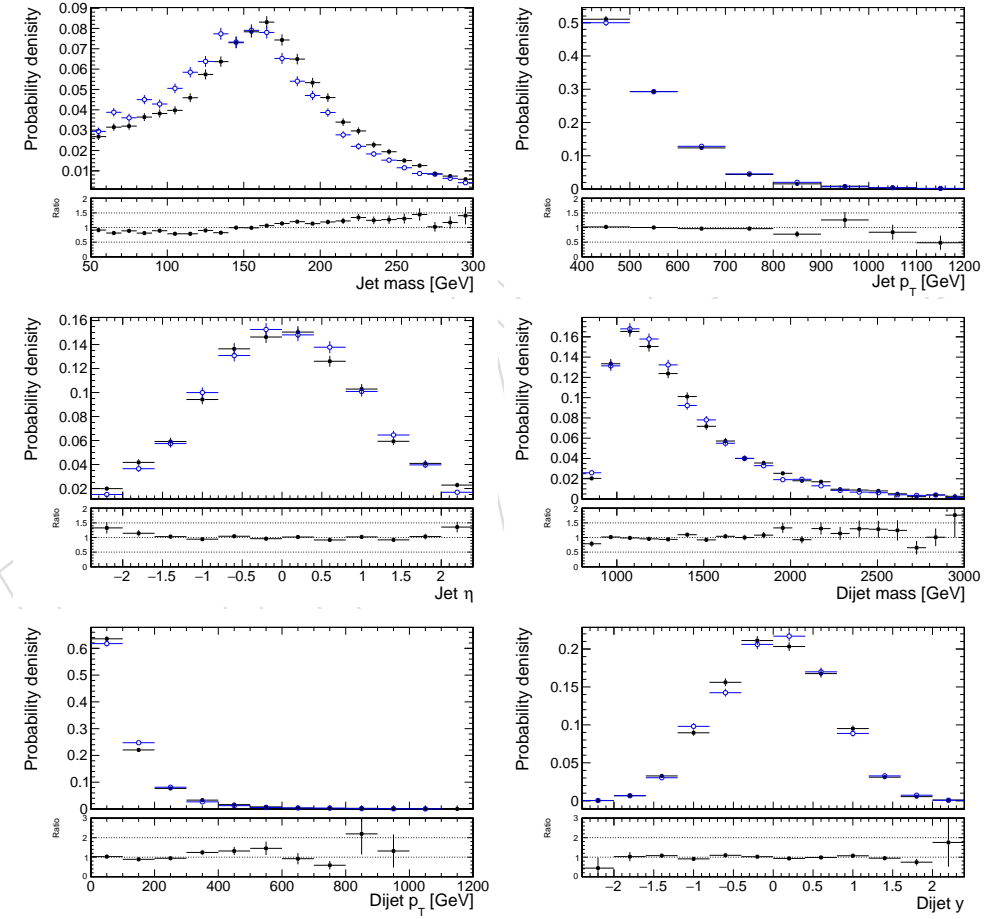


Figure 78: Distributions of jet and dijet observables from low pileup events (black,  $\text{nvtx} < 15$ ) and high pileup events (blue,  $\text{nvtx} \geq 15$ ). The bottom panel shows the ratio of the two.

598 **D Unfolding Tests**

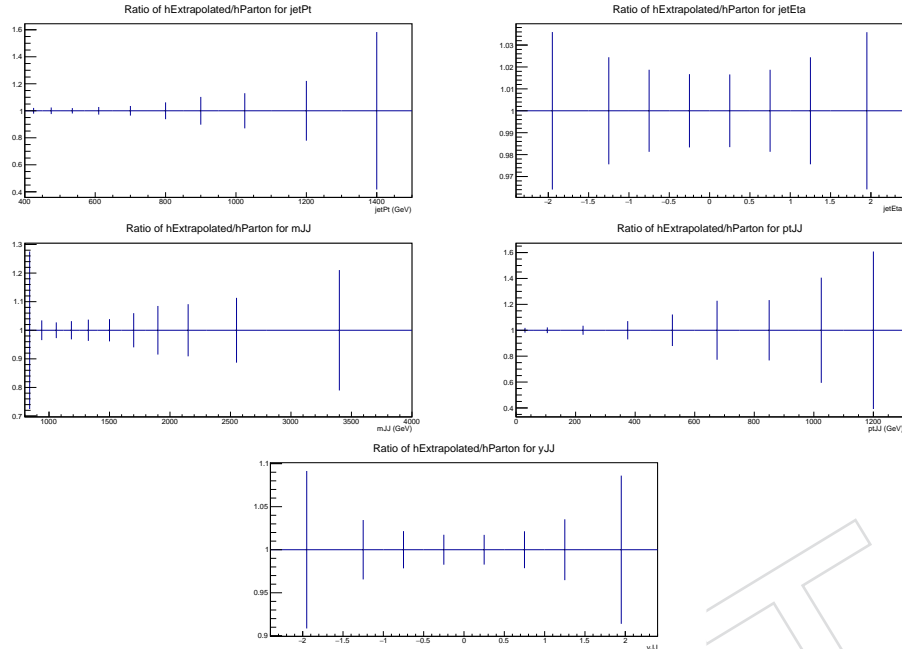


Figure 79: Parton unfolding closure test in simulation for all the reported observables. Ratio of the unfolded over the parton spectra.

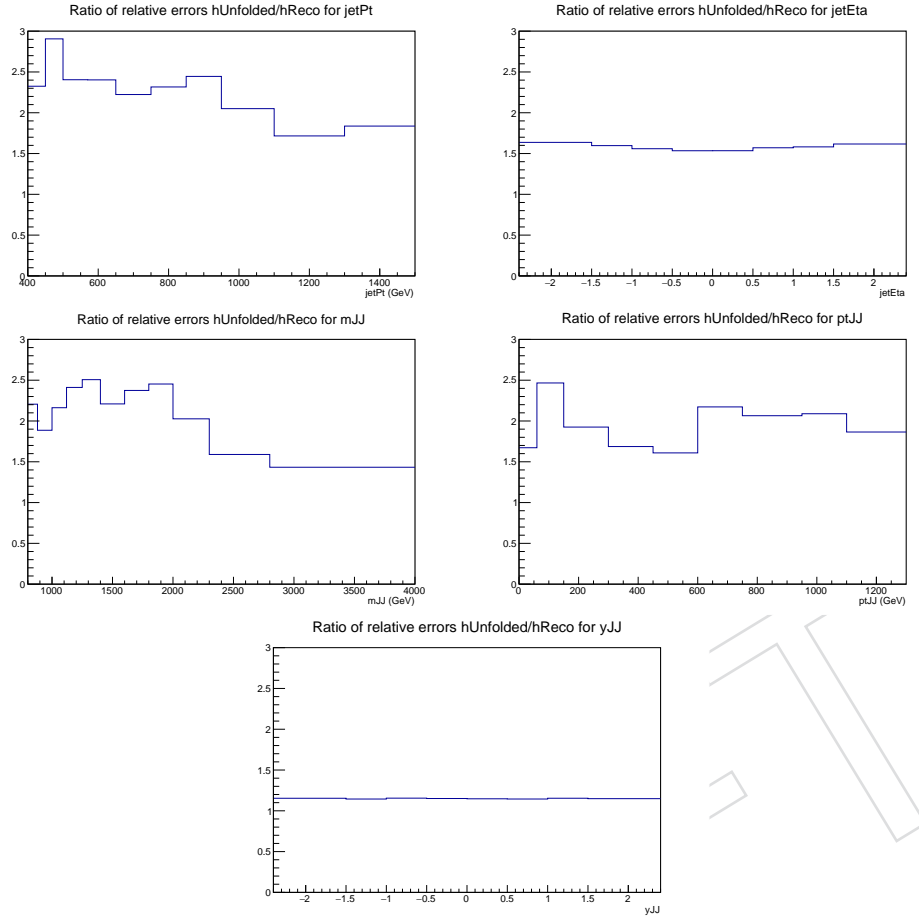


Figure 80: Ratio of the unfolded of the measured relative statistical uncertainties in the simulation (parton level).

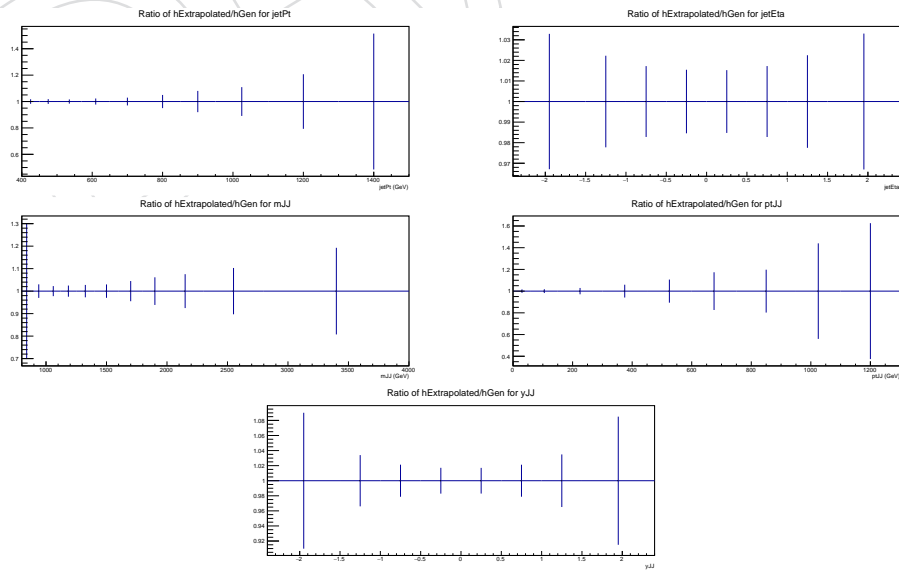


Figure 81: Particle unfolding closure test in simulation for all the reported observables. Ratio of the unfolded over the particle spectra.

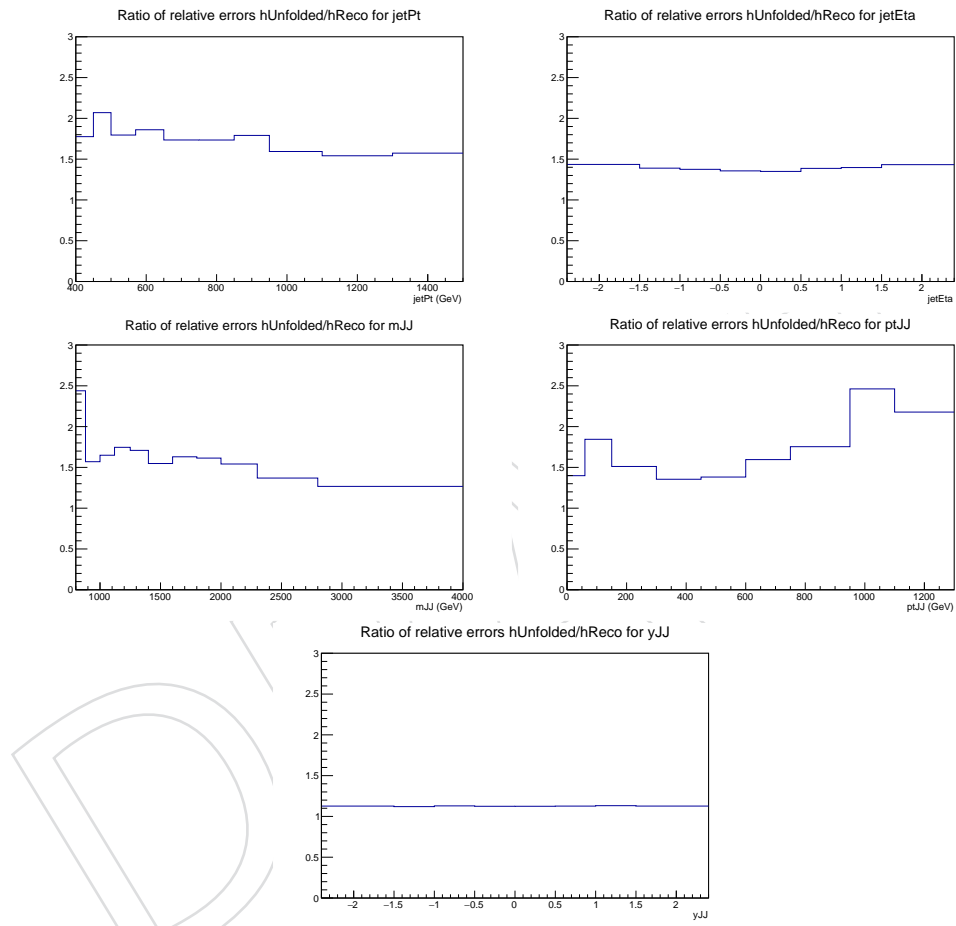


Figure 82: Ratio of the unfolded of the measured relative statistical uncertainties in the simulation (particle level).

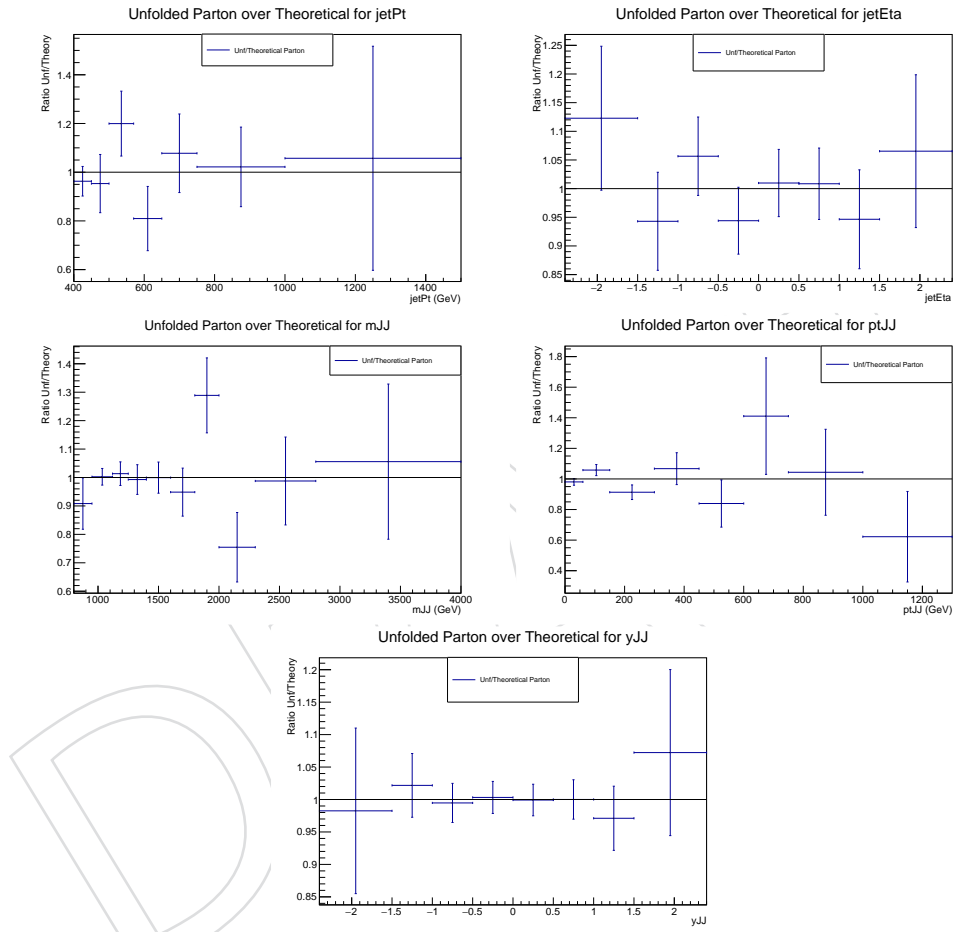


Figure 83: Stability of the unfolding at parton level in the simulation. The response matrix is derived from the first half of the sample and applied to the other half.

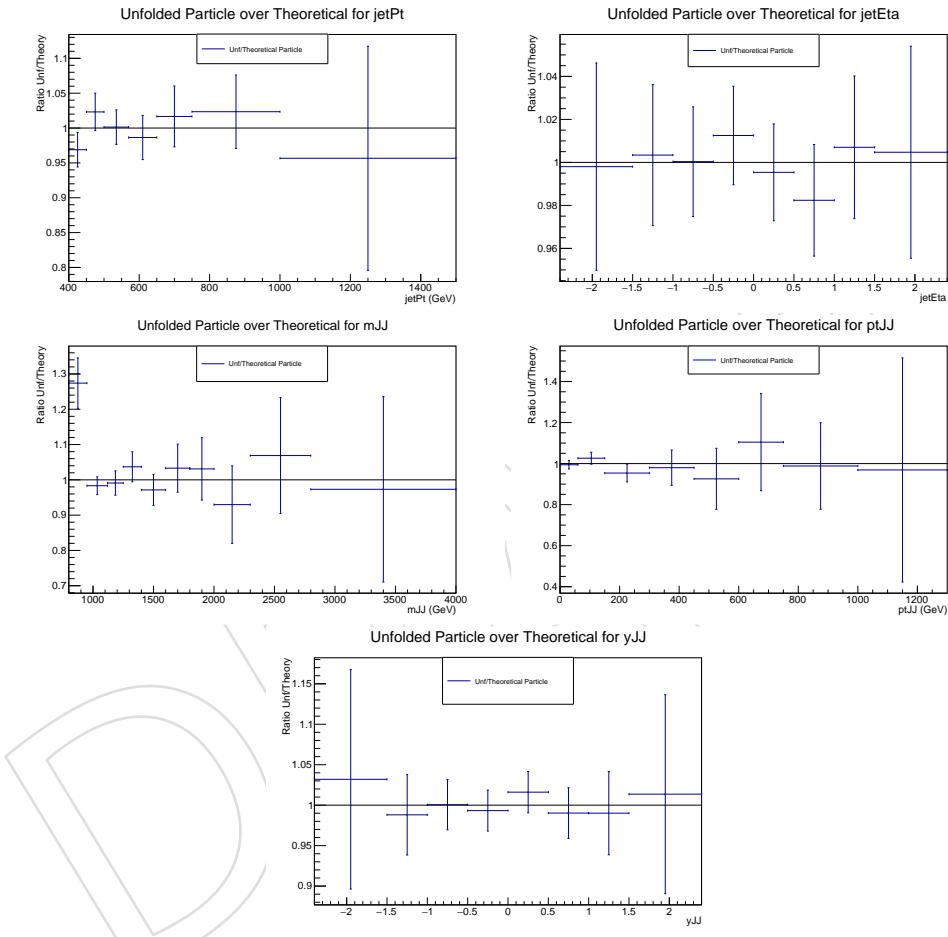


Figure 84: Stability of the unfolding at particle level in the simulation. The response matrix is derived from the first half of the sample and applied to the other half.